TECHNISCHE
UNIVERSITÄT
WIEN

MASTER THESIS

Development and Application of an Ensemble Monte Carlo Framework

submitted by

Laura Gollner

presented for the degree of

Diplom-Ingeneurin (Dipl.-Ing.)

in

Computational Science and Engineering

supervised by

Assistant Prof. Privatdoz. Dr.techn. MSc Lado Filipovic

at the

Institute for Microelectronics

Vienna, on March 1, 2023

Die approbierte gedruckte Originalversion dieser Diplomarbeit ist an der TU Wien Bibliothek verfügbar
The approved original version of this thesis is available in print at TU Wien Bibliothek.
TU WIEN Bibliothek Your knowledge hub

Abstract

Due to the fast development and high demand of semiconductor materials and devices in numerous areas related to transistor scaling along Moore's Law and extension to More-than-Moore integration, their characterization with the help of simulations has gained in importance. To enable the virtual characterization of various novel semiconductor materials and devices, a generic simulation tool which applies the multi-valley ensemble Monte Carlo method, was developed. In the scope of this thesis, the developed tool is presented, verified, and applied to different materials and devices.

First, to verify the simulation tool, the electron transport in bulk silicon was simulated and compared to published experimental results. It was shown that the behavior of the resulting drift velocity at various applied bias conditions could be reproduced. Additionally, the anisotropy and temperature-dependence of this characteristic in silicon could be replicated with the help of the developed simulator. Second, to demonstrate the ability of the tool to also simulate devices, a silicon-based MOSFET was simulated and the results were compared to the ones of `CEMC`, an established ensemble Monte Carlo simulation tool, which was also developed at the Institute for Microelectronics and is specialized for this type of device. The resulting dependence of the current and potential profile on the applied voltages at the gate and drain contact were in good agreement for both simulators.

Subsequently, initial tests with the inclusion of real-space particle-particle interactions in the ensemble Monte Carlo workflow were performed. For the approximation of the Coulomb force, which acts on each particle for one time step, the force which is felt by the carrier at the beginning of the corresponding step was calculated with the help of the fast multipole method (FMM). Within these first tests, instabilities were observed in cases when the chosen time step was too long, since the approximation of the force in these cases can lead to significant errors, because of the high and rapidly changing Coulomb force for carriers which are very close to each other. To enable longer time steps, a cut-off approach using a cut-off radius of 1 nm was applied for the evaluation of the Coulomb force. With the help of this approach and the comparison to the results from simulations without carrier-carrier interactions, the final steady-state ensemble energy of a hot ensemble of electrons and ions in bulk silicon was reproduced at varying doping concentrations. It was observed that the required time steps to avoid numerical heating in these simulations decreased with increasing doping concentration, while a time step of 5 fs was sufficient for doping levels of $1 \times 10^{13}\,\mathrm{cm}^{-3}$; a time step below 0.05 fs, however, was crucial for the simulation of silicon with a doping concentration of $1 \times 10^{18}\,\mathrm{cm}^{-3}$.

Finally, the simulator was applied to study electron transport in a monolayer of molybdenum disulfide (MoS_2). The band structure, which is used as a basis for the electron

Die approbierte gedruckte Originalversion dieser Diplomarbeit ist an der TU Wien Bibliothek verfügbar
The approved original version of this thesis is available in print at TU Wien Bibliothek.
TU WIEN Bibliothek Your knowledge hub

transport simulations of this material, is mostly obtained from *ab-initio* calculations. The problem with this approach is that varying assumptions for these simulations from first principles lead to changes in the resulting band structure. Within this thesis, the effect of changes in one specific characteristic of the band structure, the valley separation energy ΔE_{QK} between the valleys at the $\boldsymbol{K}$- and $\boldsymbol{Q}$-points, on the electron transport characteristics, was analyzed. It was shown that the electron mobility within the film varied between $100\,\mathrm{cm}^2/(\mathrm{Vs})$ and $300\,\mathrm{cm}^2/(\mathrm{Vs})$ in case ΔE_{QK} was varied within the values proposed in the literature. Additionally, due to variations in ΔE_{QK}, also the behavior of the drift velocity under different applied biases changes, with the Gunn effect being observable for higher values of ΔE_{QK}, but not for lower ones. It was concluded that, as these changes in ΔE_{QK} lead to high variations in the electron transport characteristics of the simulated film, further research is necessary to obtain a physically realistic picture for the description of this material.

Die approbierte gedruckte Originalversion dieser Diplomarbeit ist an der TU Wien Bibliothek verfügbar
The approved original version of this thesis is available in print at TU Wien Bibliothek.
TU WIEN Bibliothek Your knowledge hub

Die approbierte gedruckte Originalversion dieser Diplomarbeit ist an der TU Wien Bibliothek verfügbar
The approved original version of this thesis is available in print at TU Wien Bibliothek.
TU Wien Bibliothek Your knowledge hub

Kurzfassung

Die Charakterisierung von Halbleitermaterialien und -bauelementen gewinnt, aufgrund ihrer schnellen Weiterentwicklung und der großen Nachfrage nach diesen in verschiedensten Bereichen, immer mehr an Bedeutung. Um die virtuelle Charakterisierung von verschiedenen, neuartigen Materialien und Bauelementen, welche auf diesen basieren, zu ermöglichen, wurde im Zuge dieser Arbeit eine generisches, auf der Multi-Valley Ensemble Monte Carlo Methode basierendes Simulationstool entwickelt, verifiziert und angewandt.

Zur Verifizierung des entwickelten Tools wurden zuerst die Transporteigenschaften von Elektronen in Silizium simuliert und mit veröffentlichten, experimentellen Resultaten verglichen. Dabei wurde festgestellt, dass die resultierenden experimentellen und simulierten Driftgeschwindigkeiten der Teilchen gut übereinstimmen. Des Weiteren wurde nachgewiesen, dass sowohl die experimentell gemessene Anisotropie als auch die Temperaturabhängigkeit der Driftgeschwindigkeit mithilfe der ausgeführten Simulationen reproduziert werden konnte. Um die Fähigkeiten des Tools zur Simulation von Halbleiterbauelementen zu verifizieren, wurde anschließend ein MOSFET simuliert. Die Resultate dieser Simulationen wurden mit denen von `CEMC`, einem etablierten Simulationstool, welches auch am Institut für Mikroelektronik entwickelt wurde, verglichen. Durch diesen Vergleich wurde gezeigt, dass die resultierende Abhängigkeit des Stroms und des Potenzialprofils von der angelegten Spannung am Gate- und Drainkontakt beider Simulatoren sehr gut übereinstimmen.

Nachfolgend wurde die Teilchen-Teilchen Wechselwirkung in den Ensemble Monte Carlo Ablauf integriert. Hierzu wurde die Coulombkraft, welche während eines Zeitschrittes auf jedes Teilchen wirkt, durch die Kraft, welche am Anfang des Schrittes herrscht und mithilfe der Fast Multipole Methode berechnet wurde, approximiert. In den ersten Tests dieser Integration wurden Instabilitäten festgestellt, welche in Kombination mit zu langen Zeitschritten auftraten. Der Grund für diese Instabilitäten ist die bereits erwähnte Approximation der Coulombkraft, welche, wegen der hohen und sich schnell ändernden Kräfte bei kleinen Distanzen zwischen verschiedenen Teilchen, kombiniert mit zu groß gewählten Zeitschritten, zu signifikanten Fehlern führen kann. Um die Verwendung von längeren Zeitschritten zu erlauben, wurde eine Cut-Off-Methode, welche einen Cut-Off-Radius von 1 nm verwendet, präsentiert. Mithilfe dieser Methode und dem Vergleich zu Simulationen ohne Teilchen-Teilchen Wechselwirkungen, konnte die resultierende Energie im stationären Zustand von einem heißen Ensemble, bestehend aus Elektronen und Ionen, in Silizium reproduziert werden. Außerdem wurde beobachtet, dass die benötigte Länge der Zeitschritte, zur Vermeidung der bereits erwähnten Instabilitäten und der einhergehenden, numerischen Erwärmung in den Simulationen, von der Dotierungskonzentration im simulierten Material abhängt. Während ein Zeitschritt von 5 fs für eine Konzentration von $1 \times 10^{13}\,\mathrm{cm}^{-3}$ genügt, ist es wesentlich einen kürzeren Zeitschritt als 0.05 fs bei einer Dotierungskonzentration von

$1 \times 10^{18}\,\mathrm{cm}^{-3}$ zu verwenden.

Abschließend wurde das Tool verwendet, um eine Schicht von Molybdändisulfid (MoS_2) zu simulieren. Die Bandstruktur für dieses Material, welche als Basis für die Simulationen der Transporteigenschaften von Elektronen benötigt wird, wird zumeist mit *ab-initio* Berechnungen bestimmt. Dies führt zu Problemen, da verschiedene Annahmen bei diesen Kalkulationen zu Änderungen in der resultierenden Bandstruktur führen können. Im Rahmen dieser Arbeit wurde der Einfluss einer charakteristischen Eigenschaft der Bandstruktur, dem Energieunterschied ΔE_{QK} zwischen den Minima der Täler an den $\boldsymbol{K}$- und $\boldsymbol{Q}$-Punkten der Brillouin-Zone, auf die Transporteigenschaften der Elektronen, analysiert. Es wurde gezeigt, dass die Mobilität der simulierten Teilchen zwischen $100\,\mathrm{cm}^2/(\mathrm{Vs})$ und $300\,\mathrm{cm}^2/(\mathrm{Vs})$ schwankt, wenn ΔE_{QK} innerhalb der in der Literatur vorgeschlagenen Werte variiert wurde. Weiters wurde festgestellt, dass die Relation zwischen Driftgeschwindigkeit und Stärke des angelegten elektrischen Feldes von ΔE_{QK} abhängt, wobei der Gunn-Effekt für höhere Werte von ΔE_{QK} beobachtet wurde, jedoch nicht für niedrigere. Aus diesen Beobachtungen wurde geschlossen, dass Veränderungen von ΔE_{QK} zu großen Unterschieden der resultierenden Transporteigenschaften von Elektronen in der simulierten Schicht führen können und weitere Erforschung dieses Materials notwendig ist, um ein physikalisch realistisches Bild des Materials zu erlangen.

Die approbierte gedruckte Originalversion dieser Diplomarbeit ist an der TU Wien Bibliothek verfügbar
The approved original version of this thesis is available in print at TU Wien Bibliothek.
TU WIEN Bibliothek Your knowledge hub

Acknowledgement

First and foremost, I want to thank my supervisor, Lado Filipovic, for supporting me with advice and patience. I appreciate that he helped me to develop a deeper understanding of my topic, gave me numerous ideas, and even improved my English writing skills through his thorough feedback on my reports and thesis.

I would also like to express my deepest appreciation to the Austrian Research Promotion Agency FFG (Bridge Young Scientists) for funding this work as part of Project 878662 "Process-Aware Structure Emulation for Device-Technology Co-Optimization".

Thanks should also go to Robin Steiner and Anna Benzer who helped develop the simulation tool on which this thesis is based. Furthermore, I would like to extend my sincere thanks to Josip Bobinac and Julius Piso, who further brightened the work environment.

Most importantly, I would like to thank my family, especially my parents, Sonja and Günter Gollner, who have supported me in every phase of my life. Special thanks go to David Jäger, who I consider to be family, but needs to be mentioned individually, due to his enormous emotional help and support.

Lastly, I would like to mention Monika Spasova and Elisabeth Jäger, who took the time to proofread parts of this thesis.

Die approbierte gedruckte Originalversion dieser Diplomarbeit ist an der TU Wien Bibliothek verfügbar
The approved original version of this thesis is available in print at TU Wien Bibliothek.
TU WIEN Bibliothek Your knowledge hub

Eidesstattliche Erklärung

Ich erkläre an Eides statt, dass ich die vorliegende Diplomarbeit selbstständig und ohne fremde Hilfe verfasst, andere als die angegebenen Quellen und Hilfsmittel nicht benutzt bzw. die wörtlich oder sinngemäß entnommenen Stellen als solche kenntlich gemacht habe.

Wien, am 1. März 2023

Laura Gollner

Die approbierte gedruckte Originalversion dieser Diplomarbeit ist an der TU Wien Bibliothek verfügbar
The approved original version of this thesis is available in print at TU Wien Bibliothek.
TU WIEN Bibliothek Your knowledge hub

Contents

1. Introduction 1
1.1. Previous Work . . . 2
1.2. Aim of Thesis . . . 3
1.3. Outline of Thesis . . . 4

2. Semi-Classical Transport Theory 5
2.1. Band Structure . . . 6
2.1.1. Analytical Band Structure . . . 7
2.2. Scattering Mechanisms . . . 10
2.2.1. Calculation of Selected Scatter Rates . . . 11

3. Ensemble Monte Carlo (EMC) Method 13
3.1. Bulk Simulation . . . 13
3.1.1. Particle Initialization . . . 14
3.1.2. Particle Dynamics . . . 15
3.1.3. Output Calculation . . . 18
3.2. Device Simulation . . . 19
3.2.1. Device Representation . . . 20
3.2.2. Potential Calculation . . . 22
3.2.3. Update Electric Field . . . 23
3.2.4. Output Calculation . . . 24
3.3. Coulomb Force Treatment . . . 25
3.3.1. Fast Multipole Method (FMM) . . . 26
3.3.2. Inclusion of FMM in an EMC Workflow . . . 27

4. Implementation 29
4.1. Outline . . . 29
4.2. Device Type . . . 30
4.3. Poisson Solver . . . 32
4.4. Particle Handler . . . 33
4.4.1. Particle Implementation . . . 33
4.4.2. Tasks of Particle Handler . . . 35
4.5. Adaptations for Bulk Simulations . . . 36

5. Applications 38
5.1. Silicon (Si) . . . 38
5.1.1. Bulk Simulation . . . 40
5.1.2. Bulk Simulation Including FMM . . . 42
5.1.3. MOSFET . . . 44

Die approbierte gedruckte Originalversion dieser Diplomarbeit ist an der TU Wien Bibliothek verfügbar
The approved original version of this thesis is available in print at TU Wien Bibliothek.
TU WIEN Bibliothek Your knowledge hub

5.2. Monolayer Molybdenum Disulfide (ML-MoS_2) 48
5.2.1. Bulk Simulation 50

6. Discussion **54**

Bibliography **57**

Appendices **62**

A. Solution of the Poisson Equation **63**
A.1. Domain Partitioning 63
A.2. Discrete Approximation 63
A.2.1. Normalization 64
A.3. Solution of the Discrete Approximation 64
A.3.1. Linearization 64
A.3.2. Update of the Potential 65

B. Simulation Parameters **66**
B.1. Silicon (Si) 66
B.2. Monolayer Molybdenum Disulfide (ML-MoS_2) 67

Die approbierte gedruckte Originalversion dieser Diplomarbeit ist an der TU Wien Bibliothek verfügbar
The approved original version of this thesis is available in print at TU Wien Bibliothek.
TU WIEN Bibliothek Your knowledge hub

List of Figures

1.1. Hierarchy of transport models. 2

2.1. Characteristics of GaAs in $\boldsymbol{k}$-space. 7
2.2. Analytical approximation of the band structure of GaAs. 8
2.3. Typical constant-energy surfaces of the conduction band of semiconductors. 9
2.4. Types of scatter mechanisms in semiconductors. 12

3.1. Ensemble Monte Carlo workflow for bulk simulations. 14
3.2. Exemplary motion of one particle in an EMC simulation with applied electric field in the x-direction. 15
3.3. Workflow and sketch of the movement of particles in the EMC method. . . 17
3.4. Exemplary drift velocity ensemble average of bulk silicon. 19
3.5. Workflow for device simulations using the framework developed within the scope of this thesis. The additional components, which are required for device simulations, but not for bulk simulations are marked in light gray. . 20
3.6. Principle steps of a Particle-Mesh Scheme (PM-Scheme), visualized list from [1]. 24
3.7. Visualization of the calculation of the weights w_{pc} in 2D using different PM-Schemes. Here $w_x := \frac{\Delta_x}{h_x}$ and $w_y := \frac{\Delta_y}{h_y}$ is used. 24
3.8. Sketch of the approximation of the Coulomb force with the cut-off approach. 28

4.1. Main components of the implementation and their (simplified) relations. . . 30
4.2. Sketches of exemplary generic devices with defined shape, discrete representations, doping profiles, and contacts. 32
4.3. Structure of selected classes which are connected to the implementation of particles within the library. 35
4.4. Sketch of the periodicity in `scalFMM` in 2D with the gray box representing the simulation space and `nbLevelsAboveRoot` being a parameter that determines the number of copies of the simulation box. 37

5.1. Characteristics of Silicon in $\boldsymbol{k}$-space. 39
5.2. Scattering mechanisms in silicon and comparison to the resulting scatter rates of Vasileska et al. [2]. 40
5.3. Ensemble averages of characteristics of interest for silicon simulations with various applied electric fields in direction $\langle 1\,0\,0 \rangle$ at 300 K. 41
5.4. Electron drift velocity in silicon with varying applied electric fields parallel to the $\langle 1\,1\,1 \rangle$ or $\langle 1\,0\,0 \rangle$ directions. Furthermore, the results are compared to the experimental results from Canali et al. [3]. 42

Die approbierte gedruckte Originalversion dieser Diplomarbeit ist an der TU Wien Bibliothek verfügbar
The approved original version of this thesis is available in print at TU Wien Bibliothek.
TU WIEN Bibliothek Your knowledge hub

5.5. Effect of the cut-off approach for the cooling of a hot ensemble of electrons in silicon with a n-doping of $1 \times 10^{18}\,\text{cm}^{-3}$. 43
5.6. Cooling of a hot electron ensemble at different doping concentrations, using 200 electrons and ions for the averaging and 1 728 copies of every particle for the calculation of $\boldsymbol{F}_c$. 44
5.7. Sketch of the geometry of the simulated MOSFET-structure. 45
5.8. Equilibrium characteristics of the simulated silicon MOSFET. 46
5.9. Characteristics of the simulated silicon MOSFET with $V_d = V_g = 1\,\text{V}$ 46
5.10. Effect of applied potential at the gate and the drain on the potential cross-section at $y = 0\,\text{nm}$; if not stated otherwise, $V_g = V_d = 0\,\text{V}$. Additionally, results of the `CEMC` code are provided for comparison. 47
5.11. Resulting I-V characteristics of the simulated MOSFET (lines and circles) and comparison to the results of `CEMC` (crosses). 48
5.12. Characteristics of ML-MoS_2 in real- and **k**-space, including the armchair (A) and zigzag (Z) directions. 48
5.13. Workflow for multi-valley Ensemble Monte Carlo simulation of electrons in ML-MoS_2. 49
5.14. $\boldsymbol{K}$- and $\boldsymbol{Q}$-valleys and their constant energy surfaces. 50
5.15. Total scatter rates in ML-MoS_2 with varying energy separation ΔE_{QK}. . . 51
5.16. $\boldsymbol{K}$-valley occupation of ML-MoS_2 vs. applied electric field for varying ΔE_{QK} and comparison to the findings of Pilotto et al. [4] (dotted line). 51
5.17. Impact of varying ΔE_{QK} on the mobility of ML-MoS_2. 52
5.18. Drift velocity vs. electric field with different ΔE_{QK} and comparison to findings of Pilotto et al. [4] and Li et al. [5] (dotted lines). 53

B.1. Intervalley scatter mechanisms out of (a) $\boldsymbol{K}$- and (b) $\boldsymbol{Q}$-valleys and sketch of the corresponding phonon momenta (color). 67

Die approbierte gedruckte Originalversion dieser Diplomarbeit ist an der TU Wien Bibliothek verfügbar
The approved original version of this thesis is available in print at TU Wien Bibliothek.
TU WIEN Bibliothek Your knowledge hub

List of Tables

5.1. Parameters of the approximated silicon valleys. 38
5.2. Parameters of approximated ML-MoS_2 valleys, taken from [4]. 49

B.1. Parameters for intervalley optical scattering in silicon, taken from Vasileska et al. [2]. 66
B.2. Phonon energies at symmetry points in ML-MoS_2, taken from [5, 6]. 67
B.3. Parameters used for scatter mechanisms of ML-MoS_2, taken from [5, 6]. Additionally, intervalley scattering is visualized in Fig. B.1 and the phonon momenta are given in Table B.2. 68

Die approbierte gedruckte Originalversion dieser Diplomarbeit ist an der TU Wien Bibliothek verfügbar
The approved original version of this thesis is available in print at TU Wien Bibliothek.
TU WIEN Bibliothek Your knowledge hub

1. Introduction

Semiconductor materials and devices based on them have become indispensable in our modern world. Their applications range from digital logic circuits, where they are the building blocks of von-Neumann computers, to their employment as sensors due to their varying physical or chemical characteristics. Because of their fast development and high demand, numerous new devices and materials are frequently investigated. Since the experimental characterization is both time intensive and expensive, the analysis with simulations has gained in interest. Advantages of this virtual characterization include the ability to observe parameters which are not experimentally measurable and to help in pre-selecting promising new materials or device structures, thereby also decreasing the cost and time-to-market for new products [2, 7].

One of the principal aims of the simulation of semiconductor devices and materials is to obtain an accurate description of the charge carrier transport characteristics. In general these simulations consist of two main components, which are coupled strongly: The field, which provides an external force which causes the charge to flow, and the transport equations, which control the aforementioned flow [2]. While for material (bulk) simulations the applied electric field $\boldsymbol{E}$ is assumed to be homogeneous within the material and its strength and direction can be set, for device simulations this characteristic stems from applied voltages at contacts and varying doping concentrations, and must be calculated using its relation to the electrostatic potential Φ

$$\boldsymbol{E} = -\nabla\Phi \quad , \tag{1.1}$$

and the Poisson Equation [8]

$$\nabla \cdot (\epsilon\ \nabla\Phi) = q \cdot (n - p + N_A - N_D) \quad . \tag{1.2}$$

In this equation ϵ is the dielectric constant, n the electron concentration, p the hole concentration, and N_D and N_A the concentrations of positively- and negatively-charged impurities in the simulated device, respectively [9]. Moreover, trapped charges can also influence the potential and can thereby be included in this equation as noted in [10], but they are not covered in this thesis. The second component, the transport equations, which determine how the particles move in the presence of an electric field, can be approximated with various models which differ in their precision and complexity. The model which is chosen for a specific application depends on the accuracy required to observe the desired phenomena in the given application and the available computational resources [11]. While it would be ideal to use the most physically accurate models for all simulations, this is frequently not feasible, due to the complexity and computational effort these require. In general terms, two main groups of transport models can be identified: Quantum and semi-classical

TU WIEN Bibliothek Your knowledge hub
Die approbierte gedruckte Originalversion dieser Diplomarbeit ist an der TU Wien Bibliothek verfügbar
The approved original version of this thesis is available in print at TU Wien Bibliothek.

approaches [2]. While quantum models consider the full quantum-mechanical behavior, semi-classical ones use a mixture of classical approximations and quantum effects and are thereby less accurate. The precision required for a specific device simulation can be determined by the relation of the device dimensions and specific particle characteristics, such as the mean free path and the (de Broglie) wavelength [11]. In case the device is much larger than the aforementioned characteristics, it is sufficient to use semi-classical transport models. On the other hand, if the device is much shorter than those characteristics, quantum approaches are essential. Figure 1.1 shows a hierarchy of various transport models, with varying precision and complexity.

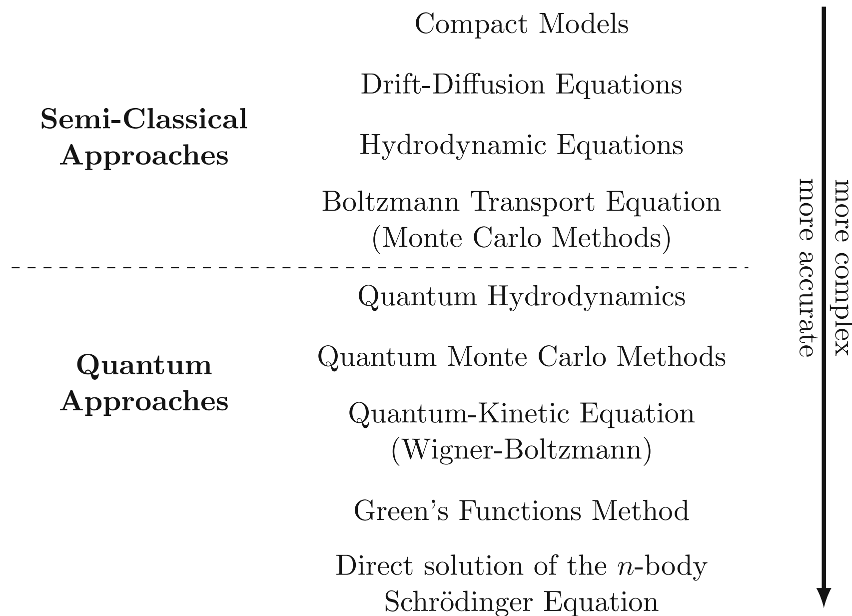

Figure 1.1.: Hierarchy of transport models.

1.1. Previous Work

This section presents a short, non-complete overview of the history of device simulations, followed by the introduction of selected state-of-the-art device simulation tools.

Before powerful computers were available, devices were theoretically characterized with closed form analytical techniques, which separate the device into regions and use linearised approximations inside the regions and adapted boundary conditions at the interfaces of the different regions [12, 13]. These techniques were suitable for large-geometry devices, but were limited to devices with principally one-dimensional transport processes and low variations in the electric field [12]. In 1964, Gummel [13] introduced the first fully numerical

Die approbierte gedruckte Originalversion dieser Diplomarbeit ist an der TU Wien Bibliothek verfügbar
The approved original version of this thesis is available in print at TU Wien Bibliothek.
TU WIEN Bibliothek Your knowledge hub

approach, based on the iterative solution of partial differential equations, to simulate the behavior of a one-dimensional bipolar transistor [7, 12, 14]. This approach was extended and applied for the one-dimensional simulation of various devices, like pn-junctions [15] and IMPATT (IMPact ionization Avalanche Transit-Time) diodes [16]. Once sufficient computational power was obtained, two-dimensional (2D) simulations were performed, including simulations of metal-oxide semiconductor field-effect transistors (MOSFETs) and metal semiconductor field effective transistors (MESFETs), with the first two-dimensional MOS-structure simulations [17, 18] being published in 1968 [19]. Several thousand papers about device simulations for different devices were issued in the following years [14]. Additionally, the trend of the continuous down-scaling of the devices and the thereby growing complexity lead to the need for three-dimensional (3D) simulations [7]. The first paper [20] which applied these three-dimensional simulations was published in 1980 [14].

Nowadays multiple commercial and openly available device simulation tools can be found. Several tools are specialized on one specific kind of device, like `MINIMOS` [21] from TU Wien, which is specialized on MOSFETs, or `BIPOLE` [22], which was written for bipolar transistors [23]. Other device simulators are written in a generic way such that different types of devices can be simulated. Prominent commercial examples for generic device simulation tools are `Sentaurus Device` [24] from Synopsys, `Victory Device` [25] from Silvaco and the commercial version of `MINIMOS-NT` [26] from Global TCAD Solutions (GTS). All three commercial tools are able to simulate various silicon and compound semiconductor devices in two and three dimensions [25, 26, 27]. Additionally, all of these tools offer the possibility to use different transport models, including the two semi-classical approaches which apply hydrodynamic and drift-diffusion equations [25, 26, 27], which can both be found in Fig. 1.1. Moreover, `Sentaurus Device` and `Victory Device` also offer Monte Carlo methods for an even more accurate approximation of the transport characteristics [27, 28]. An example for an openly available device simulation tool is `ViennaWD` [29], a `C`-based set of tools from the Institute for Microelectronics of TU Wien. This set of tools contains a semi-classical Monte Carlo simulator (`CEMC`), which can be used for the two-dimensional simulation of MOSFETs and a Wigner ensemble Monte Carlo (`WEMC`) simulator based on the solution of the Wigner-Boltzmann equation [30, 31], which can also be seen in Fig. 1.1 and is accurate up to the description of a single particle [2].

1.2. Aim of Thesis

The aim of this thesis is the development of a generic simulation tool, which can be applied for bulk and device simulations using the ensemble Monte Carlo (EMC) method. This tool should be based on the ideas of the previously mentioned tool `CEMC` from the Institute for Microelectronics at TU Wien. The original `C` code should be translated into object-oriented `C++` and extended to work for various devices and materials in two and three dimensions. Additionally, the option to include real-space particle-particle interactions using the fast multipole method (FMM), performed by the external library `scalFMM` [32, 33], should be included.

Die approbierte gedruckte Originalversion dieser Diplomarbeit ist an der TU Wien Bibliothek verfügbar
The approved original version of this thesis is available in print at TU Wien Bibliothek.
TU WIEN Bibliothek Your knowledge hub

The validation of the developed tool will be performed by the simulation of silicon-based structures, including MOSFETs for the comparison to the results of `CEMC`. Additionally, first tests to include real-space particle-particle interactions within the EMC workflow will be performed. The final step of this work is the application of the developed tool for the simulation of a monolayer of the currently heavily investigated material molybdenum disulfide (MoS_2). The aim of the second application is to demonstrate that the framework can also be applied to materials which behave quite different than silicon.

1.3. Outline of Thesis

This thesis is organized as follows:

Chapter 2 describes the necessary background and theory of the semi-classical transport equations.

Chapter 3 presents the ensemble Monte Carlo (EMC) method for material and device simulations in more detail. Additionally, a method to include real-space particle-particle interactions into the EMC workflow is presented.

Chapter 4 gives an overview of the library which is developed in the scope of this thesis by displaying the main ideas, the structure, and some examples of the code.

Chapter 5 shows the results of the applications of the developed library. First, silicon-based structures are simulated to verify the results of the implemented simulation tool. Second, first tests are performed with the included real-space particle-particle interactions, and finally, the library is used to investigate MoS_2.

Chapter 6 summarizes the findings and gives an outlook on the possible next steps.

Die approbierte gedruckte Originalversion dieser Diplomarbeit ist an der TU Wien Bibliothek verfügbar
The approved original version of this thesis is available in print at TU Wien Bibliothek.
TU WIEN Bibliothek Your knowledge hub

2. Semi-Classical Transport Theory

The basis of the *semi-classical transport theory* is the description of a particle by its *state* $(\boldsymbol{r}, \boldsymbol{k})$, which is given by the particle's position $\boldsymbol{r}$ and the current motion, or momentum, of the particle, which can be described with its wave vector $\boldsymbol{k}$. The space used for this description, which contains all possible states of particles, is called the *phase space* [34]. In this space the distribution function $f(\boldsymbol{r}, \boldsymbol{k}, t)$ represents the probability of finding carriers at the state $(\boldsymbol{r}, \boldsymbol{k})$ at a given time t [35]. The equation which considers all possible changes of the distribution function is the so-called Boltzmann transport equation (BTE), which is given by [34]

$$\frac{\partial f}{\partial t} + \underbrace{\boldsymbol{v} \cdot \nabla_{\boldsymbol{r}} f}_{\left(\frac{\partial f}{\partial t}\right)_{diff}} + \underbrace{\frac{\boldsymbol{F}}{\hbar} \cdot \nabla_{\boldsymbol{k}} f}_{\left(\frac{\partial f}{\partial t}\right)_{force}} = \left(\frac{\partial f}{\partial t}\right)_{coll} \quad , \tag{2.1}$$

where $f \mathrel{\widehat{=}} f(\boldsymbol{r}, \boldsymbol{k}, t)$ is applied [2, 36]. The terms in the BTE, Eq. (2.1), can be described as follows:

- $\frac{\partial f}{\partial t}$ describes the explicit dependence of the distribution function on time [34]. This term can be non-zero if carriers are added or subtracted over time due to scattering, generation, recombination, trapping, or releasing [37].

- $\left(\frac{\partial f}{\partial t}\right)_{diff}$ is a diffusion term and accounts for spatial variations of the distribution function, which arise from temperature or concentration gradients [2]. Furthermore, this term uses the group velocity, which can be calculated with [2]

$$\boldsymbol{v} = \nabla_{\boldsymbol{k}} E(\boldsymbol{k})/\hbar \quad , \tag{2.2}$$

  where $E(\boldsymbol{k})$ represents the dispersion relation of the corresponding semiconductor, the so-called *band structure*, which is described in Section 2.1.

- $\left(\frac{\partial f}{\partial t}\right)_{force}$ describes the acceleration caused by the Lorentz force [2]

$$\boldsymbol{F} = q \cdot (\boldsymbol{E} + \boldsymbol{v} \times \boldsymbol{B}) \quad , \tag{2.3}$$

  where $\boldsymbol{E}$ and $\boldsymbol{B}$ are the electric and magnetic fields, respectively. In the scope of this thesis it is assumed that no magnetic field is present ($\boldsymbol{B} \mathrel{\widehat{=}} \boldsymbol{0}$).

- $\left(\frac{\partial f}{\partial t}\right)_{coll}$ describes rapid changes in the distribution function due to scattering events [37] and can be represented as the difference of the in- and out-going particle flow of

Die approbierte gedruckte Originalversion dieser Diplomarbeit ist an der TU Wien Bibliothek verfügbar
The approved original version of this thesis is available in print at TU Wien Bibliothek.
TU Bibliothek, WIEN Your knowledge hub

state $(\boldsymbol{r},\boldsymbol{k})$ caused by scattering, given by [34]

$$\left(\frac{\partial f}{\partial t}\right)_{coll} = \sum_{\boldsymbol{k'}}\Bigg(\underbrace{f(\boldsymbol{r},\boldsymbol{k'},t)\,[1-f(\boldsymbol{r},\boldsymbol{k},t)]\,\Gamma(\boldsymbol{k'},\boldsymbol{k})}_{\text{in-scattering flow}} - \underbrace{f(\boldsymbol{r},\boldsymbol{k},t)\,\left[1-f(\boldsymbol{r},\boldsymbol{k'},t)\right]\Gamma(\boldsymbol{k},\boldsymbol{k'})}_{\text{out-scattering flow}}\Bigg) \quad . \tag{2.4}$$

In this equation $\Gamma(\boldsymbol{k},\boldsymbol{k'})$ is the total scatter rate for a particle to scatter from $\boldsymbol{k}$ to $\boldsymbol{k'}$ [2, 36], whose calculation is explained in Section 2.2. Additionally, the particle flow also depends on the probability of the initial state being full and the final state being empty, which is given in Eq. (2.4) by the terms $f(\boldsymbol{r},\boldsymbol{k'},t)$ and $[1-f(\boldsymbol{r},\boldsymbol{k},t)]$ for the in-scattering flow and $f(\boldsymbol{r},\boldsymbol{k},t)$ and $[1-f(\boldsymbol{r},\boldsymbol{k'},t)]$ for the out-scattering flow, respectively [34].

In case the Boltzmann transport equation can be solved and thereby $f(\boldsymbol{r},\boldsymbol{k},t)$ can be determined, several quantities of interest, such as carrier energies, densities and currents can be calculated from the average characteristics of the distribution function [2, 38]. However, due to its complicated integro-differential nature, the Boltzmann transport equation is only analytically solvable in special cases [2]. This is the reason why approximations and numerical solutions, like the method presented in the scope of this thesis, are crucial for the determination of $f(\boldsymbol{r},\boldsymbol{k},t)$.

Finally, the main approximations which lead to limitations of this semi-classical description, are the use of classical particles, for which the uncertainty principle is not considered, the assumption that scatter events are instantaneous and memory-less, and the absence of multi-particle correlations [2, 35].

2.1. Band Structure

As already mentioned, the band structure represents the dispersion relation $E(\boldsymbol{k})$ of the simulated material. For the derivation of the band structure a crystalline structure of the material of interest is assumed. Due to the periodicity in the arrangement of the lattice atoms in crystalline structures, also the potential $V_{per}(\boldsymbol{r})$ within the material fulfills

$$V_{per}(\boldsymbol{r}) = V_{per}(\boldsymbol{r} + n_1\cdot\boldsymbol{a_1} + n_2\cdot\boldsymbol{a_2} + n_3\cdot\boldsymbol{a_3}) \tag{2.5}$$

for $n_i \in \mathbb{Z}$ [8, 34]. Additionally, $\boldsymbol{r}$ represents the position in this equation and $\boldsymbol{a_i}$ are the vectors describing the lattice in the material [8, 34]. The behavior of an electron in a crystalline material is then based on the stationary Schrödinger equation, which describes carriers by their wave functions $\Psi(\boldsymbol{r})$ [35] and is given by

$$\left(-\frac{\hbar^2}{2m_0}\nabla^2 + V_{per}(\boldsymbol{r})\right)\Psi(\boldsymbol{r}) = E\Psi(\boldsymbol{r}) \quad , \tag{2.6}$$

where E is the resulting energy value and m_0 is the free electron mass [8]. According to the *Bloch theorem* the solutions to this equation are *Bloch functions* of the form

Die approbierte gedruckte Originalversion dieser Diplomarbeit ist an der TU Wien Bibliothek verfügbar
The approved original version of this thesis is available in print at TU Wien Bibliothek.
TU WIEN Bibliothek Your knowledge hub

$$\Psi_{\boldsymbol{k}}^{n}(\boldsymbol{r}) = u_{\boldsymbol{k}}^{n}(\boldsymbol{r}) e^{i\boldsymbol{k}\boldsymbol{r}} \quad , \tag{2.7}$$

where $\boldsymbol{k}$ is the wave vector of the particle, n is the index of the band, and the function $u_{\boldsymbol{k}}^{n}(\boldsymbol{r})$ possesses the same periodicity as the potential and the lattice [8, 35]. The resulting energy $E_n(\boldsymbol{k})$, which also depends on the wave vector of the particle and the index of the band, is then found to be periodic in the $\boldsymbol{k}$-space as well [8]. This implies that all the required information to describe the relation between the energy and the wave vector of an electron in the given material can be found in one period of that function, the so-called *first Brillouin zone* [35]. As an example of a real first Brillouin zone and band structure, the ones of the material gallium arsenide (GaAs) are shown in Fig. 2.1. Figure 2.1a also includes some symmetry points of the Brillouin zone, which are then used in Fig. 2.1b to describe the path for which the band structure of GaAs is shown.

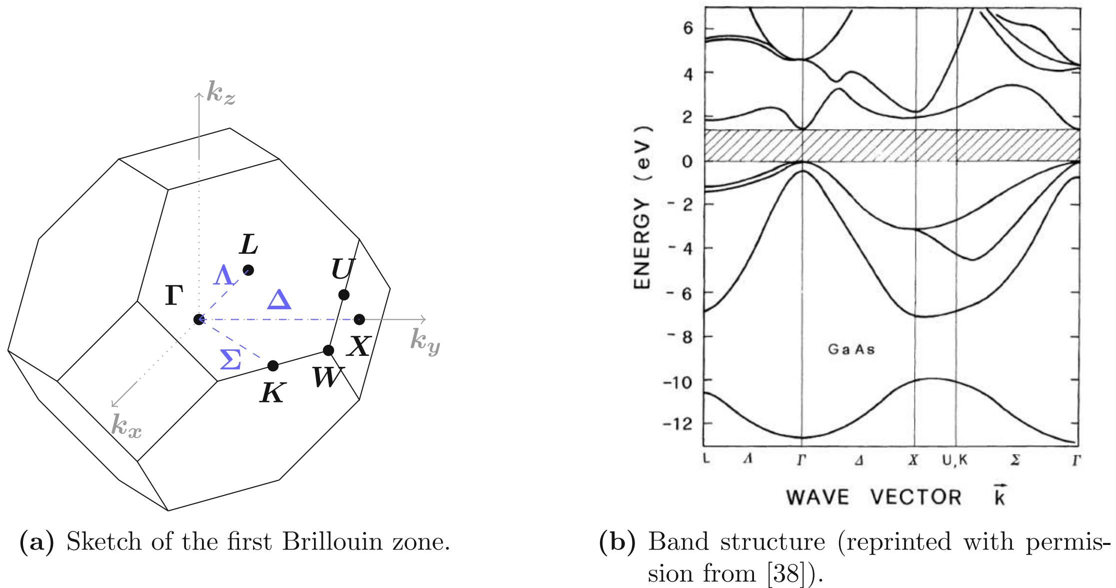

(a) Sketch of the first Brillouin zone.

(b) Band structure (reprinted with permission from [38]).

Figure 2.1.: Characteristics of GaAs in $\boldsymbol{k}$-space.

2.1.1. Analytical Band Structure

As can be observed in Fig. 2.1b, the realistic band structure of a semiconductor can be quite complicated; therefore, for computations it is easier to approximate the conduction and valence bands of that structure. This can be done by an effective mass approach, which assumes that carriers in a crystal respond to an external field the same way that a free particle would, except for an adapted effective mass m, which embodies the effect of the periodic crystal potential V_{per} on the particle [36]. This effective mass m can be calculated by [2]

$$m = \hbar^2 \left[\frac{d^2 E(\boldsymbol{k})}{d\boldsymbol{k}^2} \right]^{-1} \quad . \tag{2.8}$$

Die approbierte gedruckte Originalversion dieser Diplomarbeit ist an der TU Wien Bibliothek verfügbar
The approved original version of this thesis is available in print at TU Wien Bibliothek.
TU WIEN Bibliothek Your knowledge hub

While $E(\boldsymbol{k})$ is a quadratic function and the effective mass is thereby a constant, when one investigates a free electron, the case for an electron in a crystal is quite different, as can be seen in Fig. 2.1b. Even though the parabolic behavior of $E(\boldsymbol{k})$ cannot be observed in the whole Brillouin zone, it can be observed near extrema of the conduction and valence bands [2]. This observation and the fact that the higher parts of the conduction and the lower parts of the valence band are almost unreachable for carriers [37], lead to the idea to approximate the extrema of the bands and apply Eq. (2.8) to calculate the local effective masses around the selected extrema of the bands. As an example for this approximation, a sketch of the approximated conduction and valence bands of GaAs are shown in Fig. 2.2. It can be seen that, based on the full band structure shown in Fig. 2.1b, three minima of the conduction band are identified and approximated, one at the $\boldsymbol{L}$-, one at the $\boldsymbol{\Gamma}$- and a last one close to the $\boldsymbol{X}$-point of the first Brillouin zone given in Fig. 2.1a. Within this approach, each approximated extremum is called a *valley*. However, it should be noted that due to the symmetry of the first Brillouin zone some symmetry points and thereby also their approximated valleys appear more than once. Often valleys which are situated at the same symmetry points are grouped and handled as one group of valleys, with a specific number of degenerate sub-valleys. In the case of GaAs for example, the $\boldsymbol{\Gamma}$-valley only appears once, while the group of valleys close to the $\boldsymbol{X}$-point consists of 6 subvalleys and the one at the $\boldsymbol{L}$-point consists of 8 subvalleys.

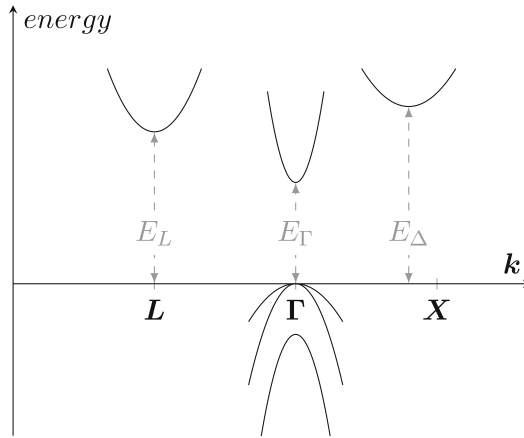

Figure 2.2.: Analytical approximation of the band structure of GaAs.

Moreover, valleys can differ in their constant-energy surfaces, which determine the value of the corresponding effective masses. For the conduction band these surfaces are typically either spherical or ellipsoidal [38], as sketched in Fig. 2.3. In the spherical case, the resulting effective mass in that valley, calculated with Eq. (2.8), is independent of the direction. The relation of the wave vector $\boldsymbol{k} = (k_x, k_y, k_z)$, which is measured from the center of the valleys, and the energy of a particle E in this valley is then given by [2]

$$\gamma(\boldsymbol{k}) := E(1 + \alpha E) = \frac{\hbar^2 \boldsymbol{k}^2}{2m} \quad . \tag{2.9}$$

Here, α is the non-parabolicity factor and m is the corresponding effective mass. In case

Die approbierte gedruckte Originalversion dieser Diplomarbeit ist an der TU Wien Bibliothek verfügbar
The approved original version of this thesis is available in print at TU Wien Bibliothek.
TU WIEN Bibliothek Your knowledge hub

$\alpha = 0$ this approximation is called *parabolic*, else a non-parabolicity is introduced, which is required in case high electric fields are applied [8]. Finally, within this approximation, the carrier group velocity $\boldsymbol{v}$ can be calculated by using Eq. (2.2), which leads to [38]

$$\boldsymbol{v} = \frac{\hbar \boldsymbol{k}}{m(1+2\alpha E)} \quad . \tag{2.10}$$

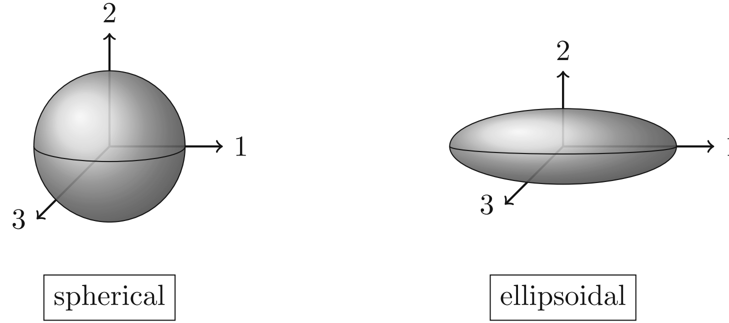

Figure 2.3.: Typical constant-energy surfaces of the conduction band of semiconductors.

A more general case is the one of elliptic equi-energetic surfaces, for which the effective mass is no longer a scalar, but rather a tensor. Under these assumptions, there still exists a coordinate system, termed the ellipse coordinate system (ECS) [2, 36] in the following, in which this tensor is diagonal of the form

$$\boldsymbol{M} = \begin{pmatrix} m_1 & 0 & 0 \\ 0 & m_2 & 0 \\ 0 & 0 & m_3 \end{pmatrix} \quad . \tag{2.11}$$

For most semiconductor valleys this tensor can be simplified by using the longitudinal effective mass $m_l := m_1$ and the transversal effective mass $m_t := m_2 = m_3$ [2, 34, 37]. In the case of elliptic constant-energy surfaces there are two special averaging functions of the direction-dependent effective mass, which are required for different calculations. The first one is the effective mass for density of states calculations m_d, which is the geometric mean of the three effective masses [38]:

$$m_d = (m_1 m_2 m_3)^{\frac{1}{3}} \quad . \tag{2.12}$$

The second one is the conductive effective mass m_c, which is, for example, used for the mobility calculation, and can be determined with the harmonic mean of the given effective masses [2, 38]:

$$m_c = \frac{3}{\frac{1}{m_1} + \frac{1}{m_2} + \frac{1}{m_3}} \quad . \tag{2.13}$$

The dispersion relation for valleys with elliptic constant-energy surfaces is given by

$$E(1+\alpha E) = \frac{\hbar^2}{2}\left(\frac{k_1^2}{m_1} + \frac{k_2^2}{m_2} + \frac{k_3^2}{m_3}\right) \quad , \tag{2.14}$$

Die approbierte gedruckte Originalversion dieser Diplomarbeit ist an der TU Wien Bibliothek verfügbar
The approved original version of this thesis is available in print at TU Wien Bibliothek.
TU WIEN Bibliothek Your knowledge hub

where $\boldsymbol{k}_{ECS} = (k_1, k_2, k_3)$ is the wave vector of the particle in the ECS and E is the energy of the particle [34, 39]. To ease the treatment of these kinds of valleys, the *Herring-Vogt transformation*, which reduces the calculations to the ones that are used for spherical valleys, is applied [38]. For this transformation the following transformation matrix [34, 38]

$$\boldsymbol{T} = \begin{pmatrix} \sqrt{\frac{m^*}{m_1}} & 0 & 0 \\ 0 & \sqrt{\frac{m^*}{m_2}} & 0 \\ 0 & 0 & \sqrt{\frac{m^*}{m_3}} \end{pmatrix} \quad , \tag{2.15}$$

where m^* is frequently either set to m_d or m_c, is used. In case the coordinate system of the simulation is not the same as the ECS, a rotation matrix $\boldsymbol{R}$, which performs the transformation from the simulation coordinate system (SCS) to the ECS is also required. After the application of the Herring-Vogt transformation, the transformed wave vector $\boldsymbol{k}^*_{ECS} = \boldsymbol{TRk}$ fulfills the following spherical dispersion relation [38]:

$$E(1 + \alpha E) = \frac{\hbar^2 {\boldsymbol{k}^*_{ECS}}^2}{2m^*} \quad . \tag{2.16}$$

2.2. Scattering Mechanisms

In a realistic physical system perturbations lead to deviations from the ideal periodicity which is assumed for the derivation of the band structure, as shown in Section 2.1. These deviations in turn lead to a huge number of transitions between various particle states and are collectively termed *scattering mechanisms* [36]. Within the semi-classical approximations these mechanisms are assumed to be instantaneous and memory-less events [2], which can alter a particle's wave vector $\boldsymbol{k}$ and the band n to which this particle is assigned. It is noteworthy that, in case the analytical band structure is applied, as mentioned in Section 2.1.1, various valleys represent the bands of the band structure and instead of altering the band, the mechanisms alter the valley to which a specific particle is assigned to. Regardless of the approximation of the band structure, the general description of scattering mechanisms is based on quantum-mechanical perturbation theory, which leads to *Fermi's Golden rule* which gives a formula for the transition rate of a particle with initial wave vector $\boldsymbol{k}$ corresponding to a specific band (valley) n to the final wave vector $\boldsymbol{k'}$ and band (valley) n' [2]:

$$\Gamma\left(n, \boldsymbol{k}, n', \boldsymbol{k'}\right) = \frac{2\pi}{\hbar} \left| \left\langle n', \boldsymbol{k'} | V(\boldsymbol{r}) | n, \boldsymbol{k} \right\rangle \right|^2 \delta\left(E_{n'}(\boldsymbol{k'}) - E_n(\boldsymbol{k}) \pm \hbar\omega\right) \quad . \tag{2.17}$$

In this equation $V(\boldsymbol{r})$ is the scattering potential of the corresponding process and $\hbar\omega$ represents the energy which is either absorbed ($-$ sign) or emitted ($+$ sign) by the particle involved in that scatter event [2]. Additionally, the dispersion relation $E_n(\boldsymbol{k})$ is given by the band structure, which is presented in Section 2.1 or by its approximation presented in Section 2.1.1. Furthermore, for the EMC workflow the transition rate which represents the

Die approbierte gedruckte Originalversion dieser Diplomarbeit ist an der TU Wien Bibliothek verfügbar
The approved original version of this thesis is available in print at TU Wien Bibliothek.
TU WIEN Bibliothek Your knowledge hub

rate at which carriers scatter out of their current state into any other possible state [35], is important and given by

$$\Gamma(n,\boldsymbol{k}) = \sum_{n',\boldsymbol{k'}} \Gamma(n,\boldsymbol{k},n',\boldsymbol{k'}) \quad . \tag{2.18}$$

Finally, in case multiple scattering mechanisms are included, the total scatter rate is calculated as the sum of the different scatter rates

$$\Gamma_{tot}\left(n,\boldsymbol{k},n',\boldsymbol{k'}\right) = \sum_{i=1}^{N_{mech}} \Gamma_i\left(n,\boldsymbol{k},n',\boldsymbol{k'}\right), \tag{2.19}$$

where N_{mech} represents the number of included scattering mechanisms and $\Gamma_{tot}\left(n,\boldsymbol{k},n',\boldsymbol{k'}\right) \widehat{=} \Gamma\left(\boldsymbol{k},\boldsymbol{k'}\right)$ from Eq. (2.4).

The typical types of scattering mechanisms which occur in semiconductors are provided in Fig. 2.4. The importance and the influence of each mechanism varies in different materials, but in general three classes of scatter mechanisms can be distinguished: The first class is defect scattering, which can happen due to crystal defects and impurities. The second type of scatter mechanisms is carrier-carrier scattering. Both, carrier-carrier scattering and the scattering due to interactions of carriers with ionized impurities (a type of defect scattering) are based on Coulomb forces and can be treated in various ways, which will be discussed in Section 3.3. The last class of scatter events is lattice scattering, which occurs due to vibrations in the crystalline lattice and the thereby resulting interactions of the considered particle and phonon [8]. This class can be subdivided based on the relation between the initial and final valley of the corresponding particle and on the involved type of phonon. In case the corresponding particle stays in the same valley the mechanism is called *intravalley*, else it is called *intervalley*. Additionally, if acoustic phonons, which arise from neighbouring particles oscillating in the same direction, are involved, the mechanism is called *acoustic*. In case optical phonons, which arise from neighboring particles oscillating in different directions, contribute to the scattering, the mechanism is called *optical* [2].

2.2.1. Calculation of Selected Scatter Rates

The formulas for the scatter rates of mechanisms which are used for all applications mentioned in this thesis, are presented in the following. The calculation of the rates of application-dependent scatter mechanisms is described in Chapter 5, within the presentation of the corresponding application. Furthermore, only the resulting scatter rates for the mechanisms are presented, as the derivation of the formulas can be found in several books including [2, 8, 34, 35, 36, 37, 38].

Two types of lattice scattering are used in both applications: Acoustic intravalley scattering and optical intervalley scattering. Both mechanisms are approximated by the application of the deformation potential approach which utilizes deformation potentials, whose values can be derived either from experiments [35] or from *ab-initio* calculations [5]. The scattering rate for acoustic intravalley scattering is given by [2, 8]

Die approbierte gedruckte Originalversion dieser Diplomarbeit ist an der TU Wien Bibliothek verfügbar
The approved original version of this thesis is available in print at TU Wien Bibliothek.
TU WIEN Bibliothek Your knowledge hub

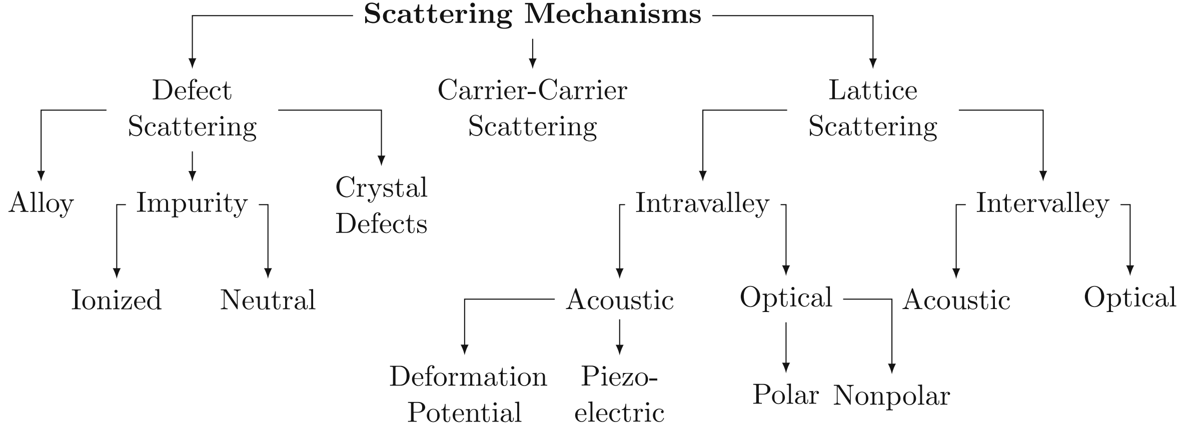

Figure 2.4.: Types of scatter mechanisms in semiconductors.

$$\Gamma_{ac}(n, \boldsymbol{k}) = \frac{2\pi\Xi^2 k_b T}{\hbar c_L} N(E_n(\boldsymbol{k})) \quad , \tag{2.20}$$

where Ξ represents the deformation potential, T is the temperature of the lattice, c_L is the elastic constant of the material, and $N(E_n(\boldsymbol{k}))$ is half of the density of states function [2]. Moreover, acoustic intravalley scattering is assumed to be elastic, meaning that the energy of the particle is not changed in the course of the scattering event, and isotropic, meaning that each direction of the final wave vector has the same probability [2, 38]. The resulting scatter rate for zero-th order optical intervalley scattering for a particle with initial associated valley i and final valley f is given by [2, 8]

$$\Gamma_{op0}(n, \boldsymbol{k}) = \frac{\pi D_{if}^2 Z_f}{\rho \omega_{if}} \left[n(\omega_{if}) + \frac{1}{2} \mp \frac{1}{2} \right] N(E_f) \cdot \Theta(E_f) \quad , \tag{2.21}$$

$$\text{with} \quad E_f = E_n(\boldsymbol{k}) \pm \hbar\omega_{if} - \Delta E_{fi} \quad . \tag{2.22}$$

Here D_{if} is the deformation potential between valley i and f, Z_f is the total number of final valleys for the carrier to scatter into, ρ is the density of the material, and E_f is the final energy of the particle, which depends on the energy of the involved phonon $\hbar\omega_{if}$ and the potential energy difference ΔE_{fi} between the bottoms of valleys i and f. Additionally, $\Theta(\cdot)$ represents the Heaviside function which ensures that the final particle energy E_f is not negative and $n(\omega_{if})$ is the phonon occupancy factor, given by [2]

$$n(\omega_{if}) = \frac{1}{e^{\frac{\hbar\omega_{if}}{k_b T}} - 1} \quad . \tag{2.23}$$

Moreover, zero-th order optical intervalley scattering is assumed to be isotropic and inelastic, meaning that the initial and final energies of the scatter event differ, as can be seen in Eq. (2.22) [2, 38].

Die approbierte gedruckte Originalversion dieser Diplomarbeit ist an der TU Wien Bibliothek verfügbar
The approved original version of this thesis is available in print at TU Wien Bibliothek.
TU WIEN Bibliothek Your knowledge hub

3. Ensemble Monte Carlo (EMC) Method

The ensemble Monte Carlo (EMC) method is a stochastic and numerical method, whose aim is to simulate the non-equilibrium transport in semiconductor devices and materials [2]. Instead of making *a priori* assumptions on the distribution function $f(\boldsymbol{r}, \boldsymbol{k}, t)$ to solve the BTE, this approach tracks the trajectories of sample particles in phase space, by moving them successively and simultaneously during small time increments Δt and by calculating their mean characteristics in between these movements [8, 36]. Within this method, the motion of the sample particles is based on random numbers, leading to random walks, whose characteristics fulfill the BTE (Eq. (2.1)) in the long time limit [2, 34].

This chapter describes the main ideas of the EMC method and is separated into the description of bulk and device simulations. While both types of simulations are based on the same principles, additional components are required for the simulation of devices. Due to this, first the ideas of bulk simulations are introduced in Section 3.1 and then the supplementary components, which are required for device simulations, are presented in Section 3.2. Finally, Section 3.3 discusses various ways to include the Coulomb force into the EMC workflow.

3.1. Bulk Simulation

Bulk simulations determine the response of a bulk material to an applied electric background field. This type of simulation allows for the determination of average carrier characteristics, such as the average energy or drift velocity, which can be compared to experimental data and can help in the characterization of materials of interest.

The full workflow of an EMC bulk simulation is shown in Fig. 3.1 and is separated into four parts: The first part of the workflow handles the definition of the input parameters, which have to be known *a priori*. In case of bulk simulations the input parameters contain characteristics of the material of interest (such as the band structure), the applied electric background field, the particle type (e.g. electrons) and the characteristics of the most important scatter mechanisms. Additionally, simulation settings, such as the total simulation time t_s and the time step Δt must be set. In the second part, the previously defined input characteristics are used for the preparation of the initial state of the simulation. First, to decrease computational effort and allow easier treatment of the scatter mechanisms during the simulation, the scatter rates for all defined mechanisms are precalculated on discrete energy values and are tabulated. Subsequently, the sample particles, which are required for the simulation, are created and initialized, by defining each particle's position, energy, wave vector and additional characteristics - more information on this initialization process is given in Section 3.1.1. The third section of the workflow contains the main simulation

Die approbierte gedruckte Originalversion dieser Diplomarbeit ist an der TU Wien Bibliothek verfügbar
The approved original version of this thesis is available in print at TU Wien Bibliothek.
TU WIEN Bibliothek Your knowledge hub

flow. It consists of one loop which starts at time $t = 0$, at which all particles are in their initialized state. In each iteration of that loop all particles move during time Δt, using alternating free-flight and scatter events, which will be described in more detail in Section 3.1.2. After the movement of the particles in each iteration, average particle characteristics, such as the average velocity or energy, are calculated - Section 3.1.3 describes this calculation in more depth. This main loop proceeds until the total simulation time t_s is reached, at which point the final results are calculated and stored, as represented by the last part of the simulation workflow.

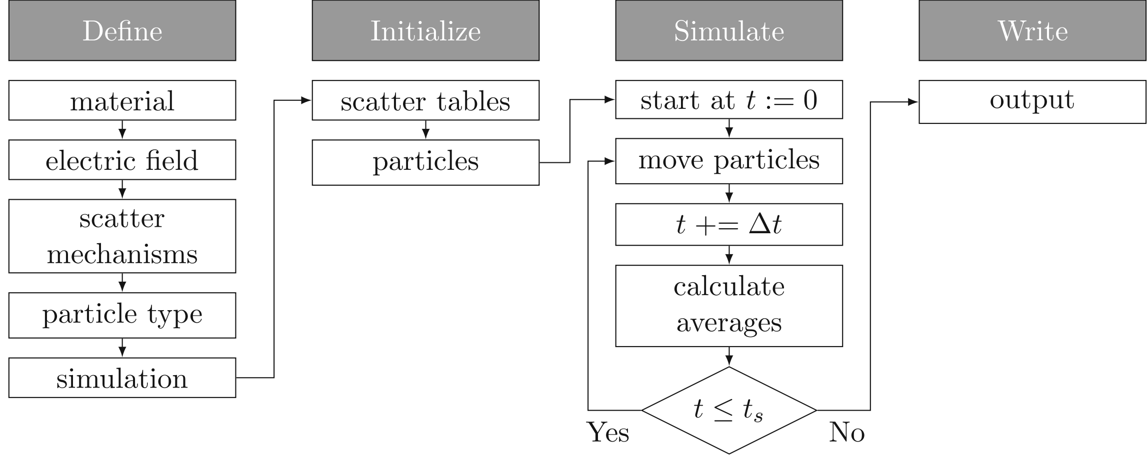

Figure 3.1.: Ensemble Monte Carlo workflow for bulk simulations.

3.1.1. Particle Initialization

At the beginning of the simulation, the state of each particle has to be defined. This means that all particles must have an assigned position $\boldsymbol{r}$, wave vector $\boldsymbol{k}$, and energy E. Additionally, each particle also requires an allocated valley (and subvalley) and a remaining free-flight time τ, which represents the time until the next scatter event for this particle takes place. Even though the influence of the choice of the initial state of the particles is not significant on the resulting average characteristics if the total simulation time t_s is long enough, it has an impact when studying transient phenomena, which can be interesting for device simulations [38].

Within the scope of this thesis, random numbers, whose distributions are adapted to the physical background of the specific property, are used for the initialization of the carrier characteristics. The determination of the initial energy E of a particle, for example, is performed with

$$E = -\frac{f}{2} k_b T \ln(rn) \ , \tag{3.1}$$

where rn is a uniformly distributed random number between 0 and 1 and f is the degree of freedom (which is 2 in 2D-materials and 3 in 3D-materials). Moreover, the determination of the remaining free-flight time of a particle is based on the assumption that the total

Die approbierte gedruckte Originalversion dieser Diplomarbeit ist an der TU Wien Bibliothek verfügbar
The approved original version of this thesis is available in print at TU Wien Bibliothek.
TU WIEN Bibliothek Your knowledge hub

scatter rate Γ_0, which is the sum of the scatter rates of all included scatter mechanisms, is independent of the particle's energy [1]. Under this assumption, one can use

$$\tau = -\frac{\ln(rn)}{\Gamma_0} \quad , \tag{3.2}$$

for the calculation of the remaining free-flight time, where rn is a uniformly distributed random number between 0 and 1 [2, 34, 38].

3.1.2. Particle Dynamics

The motion of particles within the EMC method can be separated into a sequence of free flights (or drifts) with a duration which is determined by the remaining free-flight time τ and instantaneous scatter events (or collisions), which interrupt the free flights [2]. An exemplary motion of one particle in real-space with alternating free-flights and scatter events is sketched in Fig. 3.2. In this section, first the treatment of free flights and scatter events is explained separately, followed by the description of their combination to obtain the full particle trajectories.

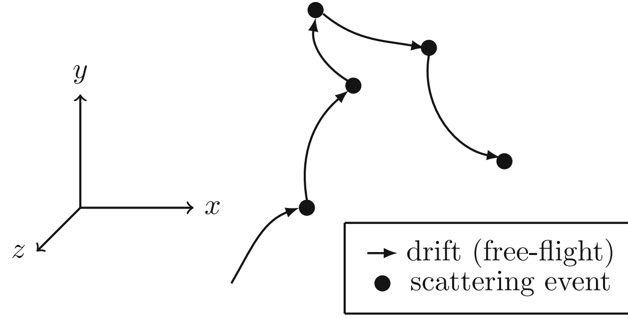

Figure 3.2.: Exemplary motion of one particle in an EMC simulation with applied electric field in the x-direction.

Free Flight

A free flight or drift describes the trajectory of a particle in the presence of an external force $\boldsymbol{F}$ [36]. After a free flight which starts at $t = 0$ and lasts for the time τ, the wave vector $\boldsymbol{k}$ of a charge carrier at position $\boldsymbol{r}$, is updated according to

$$\boldsymbol{k}(\tau) = \boldsymbol{k}(0) + \int_{t=0}^{\tau} \frac{\boldsymbol{F}(\boldsymbol{r}(t))}{\hbar}\, dt \quad . \tag{3.3}$$

The update equation for the position of the particle in case the analytical band approximation with circular constant-energy surfaces, presented in Section 2.1.1, is applied, is then given with [1]

$$\boldsymbol{r}(\tau) = \boldsymbol{r}(0) + \int_{t=0}^{\tau} \boldsymbol{v}(t)\, dt \overset{(2.10)}{=} \boldsymbol{r}(0) + \frac{\hbar}{m} \int_{t=0}^{\tau} \frac{\boldsymbol{k}(t)}{1 + 2\alpha E_n(\boldsymbol{k}(t))}\, dt \quad . \tag{3.4}$$

Die approbierte gedruckte Originalversion dieser Diplomarbeit ist an der TU Wien Bibliothek verfügbar
The approved original version of this thesis is available in print at TU Wien Bibliothek.
TU WIEN Bibliothek Your knowledge hub

Analytical solutions for Eqs. (3.3) and (3.4) only exist under simple conditions, such as constant $\boldsymbol{F}$. For this reason, numerical methods are commonly used to update the position and wave-vector [36]. In the scope of this thesis, the *leapfrog scheme* [1, 2] is applied to update these characteristics, where $\boldsymbol{F}(\boldsymbol{r}(0))$ is used to calculate $\boldsymbol{k}\,(\tau/2)$, which in turn is used to update the position of the particle.

Scatter Events

As mentioned in Section 2.2, the scatter events are instantaneous and can alter the wave vector, energy, and assigned valley of a carrier, but not its position, as sketched in Fig. 3.2. Within the EMC workflow the execution of a scatter event is equivalent to the selection of one specific scatter mechanism, the calculation of the changes of the state of the particle caused by the selected mechanism, and the determination of a new remaining free flight time τ for the corresponding particle. The calculation of τ is performed by Eq. (3.2), meaning that in this section, only the obtainment of an energy-independent total scatter rate, as required for Eq. (3.2), the selection of the scatter mechanism, and the calculation of the state of the particle after the scatter event will be discussed.

To obtain an energy-independent total scatter rate Γ_0 an additional, fictitious scattering mechanism, the so-called *self-scattering*, is introduced, which does not alter the state of a particle [2]. The scatter rate of this mechanism is defined by [8]

$$\Gamma_{self}(n,\boldsymbol{k}) := \Gamma_0 - \sum_{i=1}^{N} \Gamma_i(n,\boldsymbol{k}) \quad . \tag{3.5}$$

In this formula N represents the total number of scatter mechanisms, which possess the corresponding scatter rates $\Gamma_i(n,\boldsymbol{k})$. Additionally, Γ_0 is a fixed, pre-selected value which must be higher than or equal to the sum of the scatter rates for all input parameters.

The selection of the scattering mechanism for each scatter event is performed using uniformly distributed random numbers rn between 0 and 1. Specifically, the i-th mechanism is selected if the condition [8, 36]

$$\sum_{j=1}^{i-1} \Gamma_j(n,\boldsymbol{k}) \leq \Gamma_0 \cdot rn < \sum_{j=1}^{i} \Gamma_j(n,\boldsymbol{k}) \tag{3.6}$$

is fulfilled. Moreover, in case N scatter mechanisms are applied in the simulation and $\sum_{j=1}^{N} \Gamma_j(n,\boldsymbol{k}) \leq \Gamma_0 \cdot rn$ is fulfilled, the self-scattering mechanism is chosen and thereby no particle characteristic is altered within this scatter event. Finally, in case a non-fictitious scatter mechanism is chosen, the state of the corresponding carrier must be adapted: First, if an intervalley mechanism is considered, the valley and subvalley to which the carrier is assigned are altered accordingly. Subsequently, if the mechanism is inelastic, the energy of the particle is adapted. Ultimately, the final wave vector is calculated, with its norm being determined by the dispersion relation and the (updated) energy, and its direction being determined with the help of random numbers.

Die approbierte gedruckte Originalversion dieser Diplomarbeit ist an der TU Wien Bibliothek verfügbar
The approved original version of this thesis is available in print at TU Wien Bibliothek.
TU WIEN Bibliothek Your knowledge hub

Combination of Free-Flights and Scatter Events

The workflow of the motion of a particle for one time step Δt is given in Fig. 3.3a. This workflow combines free flights and scatter events and shows the idea of the *move particles* step from the bulk simulation workflow shown in Fig. 3.1. For the motion of a particle two cases are distinguished: The case where the remaining time for the motion of the particle t_{rem}, which is set to Δt at the beginning, is longer than the remaining free-flight time τ and the case where it is shorter. In both cases first the force acting on the carrier must be determined; for bulk simulations, the applied electric field is homogeneous and therefore the same value is always used for that step. In case of device simulations the electric field can be inhomogeneous and the re-evaluation of the force that is acting on the carrier before each free-flight is thereby essential. Next, both instances perform the drift of the particle, whose duration depends on the relation of the remaining free flight time and the remaining movement time. In the first case, $\tau > t_{rem}$, the particle drifts for the entire time step and subsequently the remaining free-flight time τ is adapted. In the second case, the particle drifts for the remaining free-flight time and then a scatter event occurs. As described earlier, in this scatter event a mechanism is selected, the state of the particle is adapted, and a new free-flight time for the particle is determined using a random number and Eq. (3.2). Lastly, t_{rem} is adapted and the distinction between the two initial cases is repeated. When using this workflow, scatter events are randomly distributed, and the number of scatter events in one time step can vary between 0 and any positive integer. This random distribution of scatter events can also be seen when looking at the time evolution of the carriers in an ensemble, which are always moved synchronously for the time Δt, thereby allowing for the calculation of average characteristics in-between these motions [36], as can be seen in Fig. 3.3b.

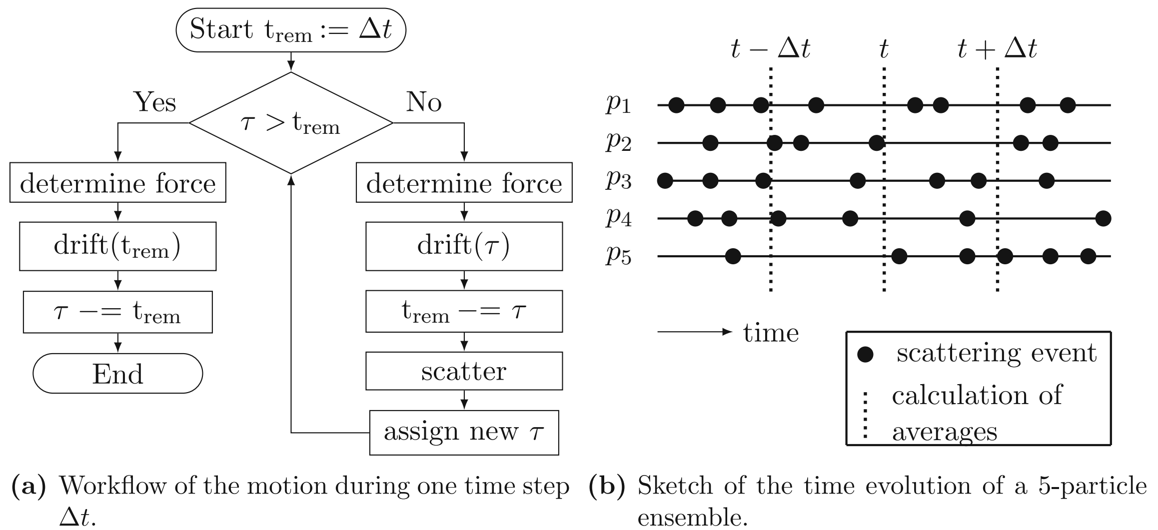

(a) Workflow of the motion during one time step Δt.

(b) Sketch of the time evolution of a 5-particle ensemble.

Figure 3.3.: Workflow and sketch of the movement of particles in the EMC method.

Die approbierte gedruckte Originalversion dieser Diplomarbeit ist an der TU Wien Bibliothek verfügbar
The approved original version of this thesis is available in print at TU Wien Bibliothek.
TU Bibliothek, WIEN Your knowledge hub

3.1.3. Output Calculation

The main characteristics of interest for bulk simulations are the average energy E of particles, the average drift velocity v_d, which is the average velocity of the particles in the direction of the applied electric field [2], and the occupation probability of the different valleys, in case multiple valleys exist in the material of interest. The calculation of these averages is performed using ensemble averages $\langle \cdot \rangle$ after every time step Δt, which can be determined for a quantity A after the j-th time step and corresponding time $t_j = j \cdot \Delta t$ with [38]

$$\langle A(t_j) \rangle = \frac{1}{N} \sum_i A_i(t_j) \quad . \tag{3.7}$$

In this formula $A_i(t_j)$ is the quantity of interest of particle i at time t_j and N represents the number of particles in the corresponding ensemble. An example of the time-evolution of the ensemble average of the drift velocity in silicon is shown in Fig. 3.4. The figure shows that, initially, the observed quantity changes with time during what is called the *transient* phase of the simulation, followed by a steady-state value, whose accuracy is determined by the statistical noise, which is called the *stationary* phase [36]. In case the resulting steady-state value of the observed quantity and not the evolution of the ensemble average is of interest, one has to ensure that the duration of the simulation is long enough to reach a steady-state [36]. Additionally, a criterion is required to determine the end of the transient phase, in order to differentiate between the ensemble averages which were calculated in the transient and the stationary phase. Once the number of initial transient steps N_{tr} and the number of steps in the stationary phase N_{st} have been determined, one can calculate the time average of the steady-state ensemble average

$$\bar{A} = \frac{1}{N_{st}} \sum_{j=N_{tr}+1}^{N_{tr}+N_{st}} \langle A(t_j) \rangle \quad , \tag{3.8}$$

to reduce the statistical variance [36].

An additional quantity of interest for bulk simulations is the mobility μ of the charge carriers, which is defined for small applied electric fields $\boldsymbol{E}$ by [2, 37]

$$v_d = \mu \cdot |\boldsymbol{E}| \quad , \tag{3.9}$$

where v_d represents the steady-state value for the drift velocity in case the electric field $\boldsymbol{E}$ is applied. The mobility can be calculated directly by simulating the response of particles in a material of interest to different small applied electric fields $\boldsymbol{E}$, determining the corresponding drift velocities and then fitting the results to Eq. (3.9). A drawback of this direct approach is that the statistical uncertainty of the resulting mobility can be large due to thermal motion [38]. An alternative approach for the determination of μ is the calculation of the diffusion coefficient at zero field via the auto-correlation function [38]. For this, during the simulation with no applied electric field, the velocity of each particle $\boldsymbol{v}(t_i)$ must be recorded at the time steps $t_i = i \cdot \Delta t$ for a reasonably long time. Subsequently, for a selected number M and for steps that fulfill $i > M$,

$$\boldsymbol{v}(t_i) \cdot \boldsymbol{v}(t_{i-j}) \quad \forall j = 0, 1, \ldots, M \tag{3.10}$$

Die approbierte gedruckte Originalversion dieser Diplomarbeit ist an der TU Wien Bibliothek verfügbar
The approved original version of this thesis is available in print at TU Wien Bibliothek.
TU WIEN Bibliothek Your knowledge hub

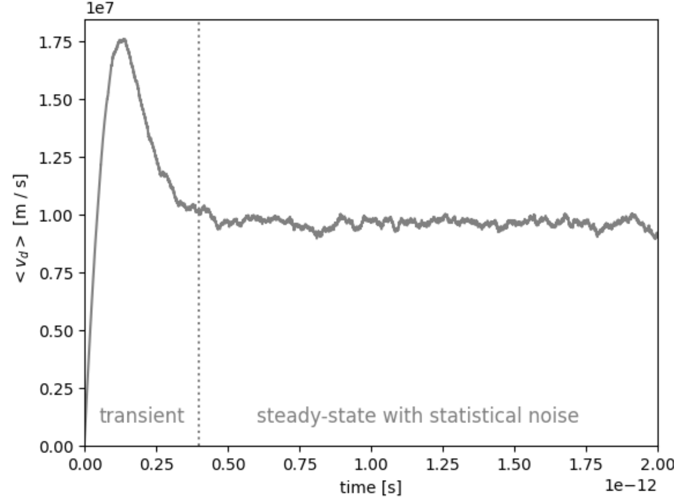

Figure 3.4.: Exemplary drift velocity ensemble average of bulk silicon.

can be calculated using $t_{i-j} = (i - j) \cdot \Delta t$. Based on these terms, the auto-correlation function can be derived by applying [38]

$$C(t_j) = \overline{\boldsymbol{v}(t) \cdot \boldsymbol{v}(t - t_j)} - v_d^2 \quad , \tag{3.11}$$

where $\overline{\boldsymbol{v}(t) \cdot \boldsymbol{v}(t - t_j)}$ is the average over the results of Eq. (3.10) with the same used value for j. Subsequently, the diffusion coefficient $D = \frac{1}{f} \int_0^\infty C(t)dt \approx \frac{1}{f} \sum_{j=0}^{M} C(t_j)$ can be determined, assuming that M steps are sufficiently large to fulfill $C(t_j) \approx 0$ for $j > M$ [38] and that f represents the degrees of freedom [38, 40]. Finally, for the calculation of the mobility the Einstein relation

$$D = \frac{\mu k_b T}{q} \quad , \tag{3.12}$$

where q is the elementary charge, can be applied [34, 38].

3.2. Device Simulation

As the name states, the aim of *device simulations* is the simulation of a semiconductor device, as opposed to a bulk material, which is discussed in the previous section. For the description of such a device the doping profile, the extent, and the position and type of contacts must be known. Additionally, in the device simulation, the electric field resulting from the potential applied at the contacts and the distribution of the charge carriers inside the device can be calculated by solving the Poisson equation Eq. (1.2) and applying Eq. (1.1). However, care has to be taken, as the resulting electric field depends on the particle distributions, which means that, if the positions of the simulated particles change during the simulation, also the resulting electric field changes. One method to incorporate this relation into the simulation is *self-consistent*, where the electric field is updated in fixed time steps using the particle distribution at that time for its calculation [8].

TU WIEN Bibliothek Your knowledge hub
Die approbierte gedruckte Originalversion dieser Diplomarbeit ist an der TU Wien Bibliothek verfügbar
The approved original version of this thesis is available in print at TU Wien Bibliothek.

The workflow of a typical self-consistent device simulation can be seen in Fig. 3.5, where it can be observed that most steps of this workflow are also required in bulk simulations and were therefore explained in Section 3.1. The additional steps which are required for device simulations are marked in light gray in the figure and represent the definition of the device geometry, the initialization of the potential distribution in the device, the calculation of the electric field, and the handling of particles at the device boundary. In the following sections all additional steps will be discussed, with the definition of the device and the handling of the boundaries in Section 3.2.1. The initialization and the general calculation of the potential are then presented in Section 3.2.2 and the update of the electric field is described in Section 3.2.3. Finally, Section 3.2.4 presents exemplary characteristics of interest for device simulations, such as the final current at each contact.

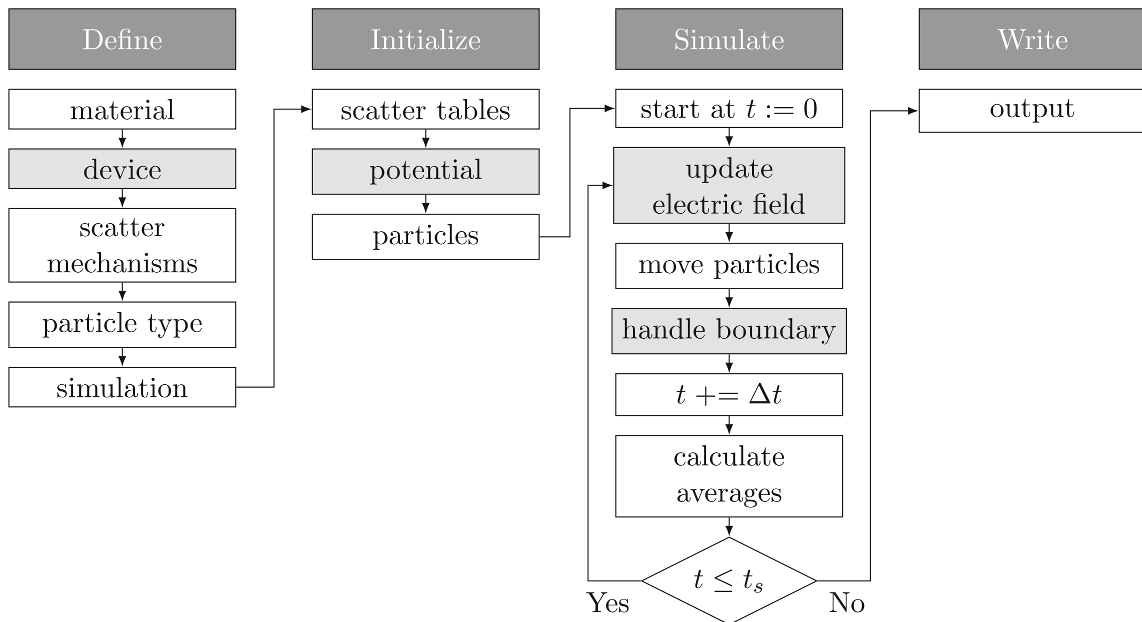

Figure 3.5.: Workflow for device simulations using the framework developed within the scope of this thesis. The additional components, which are required for device simulations, but not for bulk simulations are marked in light gray.

3.2.1. Device Representation

To represent a device within an EMC simulation, a simplified and tractable model of the device needs to be created [38]. Approximations, which can be applied within the model, are reduced dimensions and the treatment of Ohmic contacts as ideal, without any resistance [38]. The reduced dimensions can be assumed for cases where introducing a higher dimension provides no variation in the relevant physical quantities. The resulting tractable model must also include information about the device's extents, its doping profile, and the positioning and type of contacts. Additionally, as the geometry of the simulated device is discretized within the simulation, also the resulting mesh, which takes into consideration

Die approbierte gedruckte Originalversion dieser Diplomarbeit ist an der TU Wien Bibliothek verfügbar
The approved original version of this thesis is available in print at TU Wien Bibliothek.
TU WIEN Bibliothek Your knowledge hub

the extent of the device, must be defined. Within the scope of this thesis, uniform meshes with spacing $\boldsymbol{h} = (h_x, h_y, h_z)$ between the grid points are used for the discrete representation of devices of interest. Each characteristic of the device, such as the doping profile or the potential, is then defined only on the discrete mesh points and not in the continuous domain.

The definition of the boundaries of the device is important to enforce boundary conditions for the solution of the Poisson equation which is required for the calculation of the electric field within the device, and for the particle dynamics, in the cases when a moving particle reaches the boundary [38]. Depending on the type of the boundary the conditions for both, the Poisson equation and the particle dynamics, can vary: First, if no contact is located at the boundary, a particle that reaches this border is reflected back into the device, according to a predefined surface or interface scattering mechanism. For the Poisson equation, it is assumed that no electric field in the direction which is normal to the given boundary exists, which leads to the Neumann boundary condition [8]

$$\boldsymbol{E_n} = -\frac{\partial \Phi}{\partial \boldsymbol{n}} = 0 \quad . \tag{3.13}$$

Here $\boldsymbol{E_n}$ is the electric field in the $\boldsymbol{n}$ direction which is normal to the given boundary. Second, as mentioned previously, Ohmic contacts are assumed to be ideal and resistance-free, meaning that they allow particles to leave and enter the device and to contribute to the current, which will be discussed in more detail in Section 3.2.4. For this assumption to be reasonable, a region around the contact is considered to be in thermal equilibrium, meaning that the total number of particles near that contact is kept constant and equal to the number of dopant ions [2]. The handling of this condition within EMC simulations will also be discussed in Section 3.2.4. For the Poisson equation, Dirichlet boundary conditions which consider the applied voltage V_{app} and the built-in potential V_{bi} [41]

$$\Phi = V_{app} + V_{bi} \quad , \tag{3.14}$$

are applied at Ohmic contacts, for which the built-in potential can be calculated using [42]

$$V_{bi} = \frac{k_b T}{q} \operatorname{arcsinh}\left(\frac{N_D - N_A}{2n_i}\right) \quad . \tag{3.15}$$

In this equation q is the elementary charge, N_A and N_D are the negatively- and positively-charged dopant concentrations, representing electron acceptors and donors, respectively, and n_i is the intrinsic carrier concentration. The last type of boundary considered within the scope of this work is the Gate contact, which represents interfaces between the semiconductor material of a device and an oxide, with a contact on top of the oxide. For the particle dynamics, once again reflective boundary conditions are applied. To obtain the final boundary condition for the Poisson equation it is assumed that no charges are present at the interface. This leads to a continuous displacement vector between the semiconductor (sc) and the oxide (ox), given by [19, 41]

$$\epsilon_{ox} \left.\frac{\partial \Phi}{\partial \boldsymbol{n}}\right|_{ox} = \epsilon_{sc} \left.\frac{\partial \Phi}{\partial \boldsymbol{n}}\right|_{sc} \quad , \tag{3.16}$$

Die approbierte gedruckte Originalversion dieser Diplomarbeit ist an der TU Wien Bibliothek verfügbar
The approved original version of this thesis is available in print at TU Wien Bibliothek.
TU WIEN Bibliothek Your knowledge hub

where ϵ_{sc} and ϵ_{ox} represent the dielectric constant of the semiconductor and the oxide, respectively. Moreover, it is assumed that the potential through the oxide drops linearly, given by [19]

$$\left.\frac{\partial \Phi}{\partial \boldsymbol{n}}\right|_{ox} = \frac{V_G - \Phi}{t_{ox}} \quad , \tag{3.17}$$

where t_{ox} is the thickness of the oxide and V_G is the potential at the gate, which is obtained by combining the applied voltage and a pre-defined barrier height. Combining Eq. (3.16) and Eq. (3.17) leads to a mixed (Robin) boundary condition for the Poisson equation at the gate contact

$$\left.\frac{\partial \Phi}{\partial \boldsymbol{n}}\right|_{sc} = \frac{\epsilon_{ox}}{\epsilon_{sc} \cdot t_{ox}} \left(V_G - \Phi\right) \quad . \tag{3.18}$$

3.2.2. Potential Calculation

The calculation of the electrostatic potential in the device, which is required to obtain the corresponding electric field, is performed by solving the Poisson equation, a partial differential equation shown in Eq. (1.2). For the solution of this equation the device domain and its boundary conditions have to be defined. Additionally, the dielectric constant ϵ, electron concentration n, hole concentration p, and N_A and N_D, which are the negatively- and positively charged impurity concentrations, respectively, have to be known. While the charged impurity concentrations, the dielectric constant, and the device domain can be determined directly from the given device of interest, two kinds of assumptions are made for the remaining parameters throughout the simulation. The first type of assumptions are equilibrium ones, which are required at the beginning of the simulation for the initialization of the potential. For the solution of the Poisson equation, with the assumption of the device being in equilibrium, the applied voltages at the contacts are discarded, meaning $V_{app} = 0$ is assumed. Additionally, equilibrium conditions are applied for the electron and hole concentrations, given by

$$n = n_i \cdot e^{\frac{\Phi}{V_T}} \quad \text{and} \tag{3.19}$$

$$p = n_i \cdot e^{-\frac{\Phi}{V_T}} \quad , \tag{3.20}$$

respectively. In this equation n_i represents the intrinsic carrier concentration, and V_T is the thermal voltage, given by $V_T = \frac{k_b T}{q}$ [2]. The second type of assumptions represent the non-equilibrium state of the device and are applied during the main simulation loop for updating the electric field, given by the *Simulate* section in Fig. 3.5. In this case, the applied voltages at the contacts are not discarded. Moreover, the free carrier concentrations of the simulated particle types are calculated with the utilization of the actual simulated particles, by assigning their charge to the discrete mesh which represents the device - this calculation will be explained in Section 3.2.3.

The solution of the Poisson equation with both types of assumptions can then be calculated using theoretical or numerical approaches. Theoretical approaches may become

Die approbierte gedruckte Originalversion dieser Diplomarbeit ist an der TU Wien Bibliothek verfügbar
The approved original version of this thesis is available in print at TU Wien Bibliothek.
TU WIEN Bibliothek Your knowledge hub

unfeasible if the boundary conditions are too complex, which can be the case for semiconductor devices [2]. Hence, numerical approaches are mostly used for the solution of the Poisson equation for device simulations. In general, three parts are required for the numerical solution of the Poisson equation: A partition of the domain, an approximation of the continuous differential equation with algebraic equations, using only the evaluation on the discrete points in the partitioned domain, and a means to solve this discrete approximation of the continuous equation [19]. While the partition of the domain can be performed in various ways, in the scope of this thesis the uniform meshes, mentioned in Section 3.2.1, are utilized. Subsequently, the discrete approximation of the Poisson equation can be obtained by the application of the finite difference method or the finite boxes method, both of which result in a large system of algebraic equations with unknown variables at discrete points representing the continuous behavior of the quantities of interest [19]. Finally, also the resulting linear system of algebraic equations can be solved in various ways, including direct approaches, for example by the application of the Gauss Elimination Method or LU Decomposition. Alternatively, the system can be solved in an iterative manner by using, e.g., the Gauss-Seidel or the Successive-Over-Relaxation (SOR) methods [2]. The solution of the Poisson equation with the application of the finite difference scheme and the SOR solver, as applied within the scope of this thesis, is presented in more detail in Appendix A.

3.2.3. Update Electric Field

For the calculation of the electric field based on the distribution of the particles within the device, a method to relate the continuous positions of the particles with the discrete representation of the device is required [2, 36] and is carried out by a so-called Particle-Mesh Scheme (PM-Scheme). The steps of a typical PM-Scheme are provided in Fig. 3.6. First, the charge of each particle is assigned to the discrete mesh points by selecting a weight $w_{pc} \in [0, 1]$ for each particle p with given charge ρ_p and coordinate c [2]. This weight determines the portion of ρ_p which is assigned to the given coordinate based on the current position of the particle. After the charge of each carrier is assigned to the corresponding mesh points, the effective carrier concentration corresponding to each mesh point can be determined. This enables the calculation of the potential at the coordinates by solving the Poisson equation using non-equilibrium assumptions, as described in Section 3.2.2. Subsequently, the electric field at discrete points can be obtained by calculating the discrete derivative of the potential [36]. To obtain the field that is felt at a specific particle position, the weights, which were determined in the first step, are reused to link the discrete electric field and the continuous particle position by

$$\boldsymbol{E_p} = \sum_c w_{pc} \boldsymbol{E_c} \quad , \tag{3.21}$$

where $\boldsymbol{E_p}$ represents the electric field at the particle and $\boldsymbol{E_c}$ is the electric field at each coordinate c in the given discrete representation of the device [2]. The first three steps of this procedure are performed for each update of the electric field in the EMC device simulation workflow, shown in Fig. 3.5. The last step is performed prior to each particle drift and is required for the determination of the force at the particle position, as can be

Die approbierte gedruckte Originalversion dieser Diplomarbeit ist an der TU Wien Bibliothek verfügbar
The approved original version of this thesis is available in print at TU Wien Bibliothek.
TU WIEN Bibliothek Your knowledge hub

seen in the workflow describing the motion of a particle shown in Fig. 3.3a.

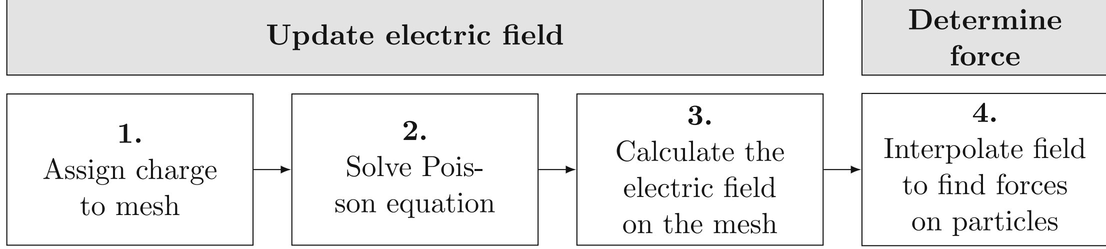

Figure 3.6.: Principle steps of a Particle-Mesh Scheme (PM-Scheme), visualized list from [1].

Different schemes exist to calculate the particle weights w_{pc}: The first one is the Nearest-Grid-Point (NGP) scheme, where the full charge of the particle is assigned to the closest grid point, which means that $w_{pc} = 1$ holds, if coordinate c is the closest to the current particle p, else $w_{pc} = 0$ [1, 2, 38]. Another method is the Nearest-Element-Center (NEC) scheme, which splits the charge of a particle equally between the components of the element with the closest center. This means that, in two dimensions, the charge is assigned equally with a weight of 0.25 to the 4 points of the rectangular mesh element with the closest center and in three dimensions the same is performed with a weight of 0.125 to the 8 points of the corresponding mesh element [2]. At last, the Cloud-In-Cell (CIC) scheme assigns the charge to the same points as the previous method, but not each point receives the same portion of the charge; the assignment is weighted by the distance of the particle to the mesh point [1, 2, 38]. An example for the determination of the weights for one particle p using the different schemes can be seen in Fig. 3.7.

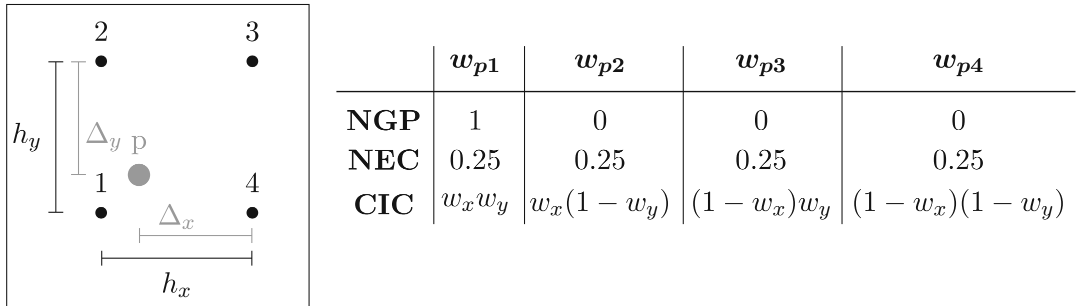

	w_{p1}	w_{p2}	w_{p3}	w_{p4}
NGP	1	0	0	0
NEC	0.25	0.25	0.25	0.25
CIC	$w_x w_y$	$w_x(1-w_y)$	$(1-w_x)w_y$	$(1-w_x)(1-w_y)$

Figure 3.7.: Visualization of the calculation of the weights w_{pc} in 2D using different PM-Schemes. Here $w_x := \frac{\Delta_x}{h_x}$ and $w_y := \frac{\Delta_y}{h_y}$ is used.

3.2.4. Output Calculation

One of the main characteristics of interest for device simulations is the current I at each Ohmic contact. This characteristic can be calculated by tracking the net number n_{net} of particles which exit or enter the corresponding contact through a fixed period of time Δt

Die approbierte gedruckte Originalversion dieser Diplomarbeit ist an der TU Wien Bibliothek verfügbar
The approved original version of this thesis is available in print at TU Wien Bibliothek.
TU Bibliothek WIEN Your knowledge hub

[2]. In general two different contributions to the net current exist: First, the number of particles which naturally leave the device by passing through the contact N_{exit} has to be considered. The second contribution stems from the number of particles which are deleted N_{del} or injected N_{inj} due to the condition that the amount of particles close to the contact should be constant, as mentioned in Section 3.2.1. Within the simulation this condition is ensured by comparing the number of particles close to the contact to the expected number of particles and by deleting excess particles or injecting missing particles until these numbers match. The final current at each contact is then determined by

$$I = \frac{q \cdot n_{net}}{\Delta t} = \frac{q \cdot (N_{exit} + N_{del} - N_{inj})}{\Delta t} \quad , \tag{3.22}$$

where q represents the charge of the corresponding particles [2].

Additional characteristics of interest in device simulations are the average potential, the average electric field, and the average particle concentration in the device. All of these quantities can be determined through time-averaging once the stationary state of the simulation is reached, as discussed in Section 3.1.3.

3.3. Coulomb Force Treatment

Calculating the Coulomb force is required for the determination of the interaction between different carriers, termed carrier-carrier (c-c) interaction, and the interaction between the carriers and the ionized impurities (dopants) in doped regions of a material, termed carrier-impurity (c-i) interaction. Both interactions are also mentioned in Fig. 2.4 as types of scattering mechanisms, with c-i being referred to as *ionized impurity scattering*.

While in typical EMC bulk simulations, as described in Section 3.1, the long-range part of the Coulomb force is not considered, in device simulations, as described in Section 3.2, it is incorporated through the solution of the Poisson equation. Furthermore, in these traditional simulations, the short-range part of the Coulomb force is either discarded or approximated in $\boldsymbol{k}$-space [2]. For this approximation the carrier-impurity (c-i) interactions are mostly treated as a two-body problem, with the application of a screened Coulomb potential [38]. One approach for the description of the screened potential was suggested by Brooks and Herring and assumes a scattering potential of [2]

$$V(r) = \frac{Zq^2}{4\pi\epsilon r} e^{-q_D r} \quad , \tag{3.23}$$

where r is the distance between the carrier and the impurity, q is the elementary charge, ϵ the dielectric constant of the material, Z is the number of charge units of the impurity, and $L_D = \frac{1}{q_D} = \sqrt{\frac{\epsilon V_T}{q(n+p)}}$ is the Debye length which depends on the thermal voltage V_T and the electron and hole concentrations n and p, respectively [2, 8, 38]. The resulting scatter rate for the interaction of a single carrier with a single impurity, which is calculated using Eq. (2.17), is then given by [2]

Die approbierte gedruckte Originalversion dieser Diplomarbeit ist an der TU Wien Bibliothek verfügbar
The approved original version of this thesis is available in print at TU Wien Bibliothek.
TU Wien Bibliothek Your knowledge hub

$$\Gamma(n, \boldsymbol{k}) = \frac{\sqrt{2} N_i Z^2 q^4}{\epsilon^2 \sqrt{m_d E_\beta}} \sqrt{E(1+\alpha E)} \frac{1+2\alpha E}{1+\frac{4E(1+\alpha E)}{E_\beta}} \quad , \tag{3.24}$$

where $E = E_n(\boldsymbol{k})$ is calculated with the given dispersion relation. Additionally, N_i represents the doping concentration and $E_\beta = \frac{\hbar^2 q_D^2}{2m_d}$, where q_D is defined via the Debye length as previously mentioned [2]. Moreover, also the short-range carrier-carrier interaction is mostly approximated with binary collisions and a screened Coulomb potential. Limitations of these approximations are the discarding of multi-ion contributions for c-i scattering and the neglection of the fact that both, the local distribution function and the screening length, can change for c-c interactions [43, 44].

While the presented approximations of the Coulomb force are sufficient in some cases, a more accurate treatment of c-i interactions is essential, for example for the simulation of ultra-small devices, in which threshold voltage fluctuations can appear due to the discrete nature of the impurity atoms [2, 43] and a more careful approximation of c-c interactions is crucial for the analysis of hot-carrier degradation [45]. For these cases, a treatment which is more precise within a classical framework for both c-c and c-i interactions, has been presented using different techniques: The particle-particle particle-mesh (P^3M) method [43], the Corrected Coulomb approach [46, 47], and the fast multipole method (FMM) [48, 49, 50]. The first approach, the P^3M method, separates the Coulomb force into a long-range part, which is calculated by the Poisson equation, and a short-range one, which is calculated by direct summation [50]. In this method care has to be taken to avoid so-called double-counting, which means that it should be circumvented to consider the contribution of one particle in both the long- and short-range potentials [2]. The second method, the Corrected Coulomb approach, is a numerical method which utilizes separate look-up tables for c-c and c-i interactions, which contain the pre-calculated change of the force due to short-range interaction between a carrier and another carrier or an impurity at a given distance, respectively [50]. The last method, the combination of the FMM and EMC, which is applied in this thesis, will be explained in the following sections, with a short description of the FMM algorithm in Section 3.3.1 and the main idea for the inclusion of this algorithm into the EMC workflow presented in Section 3.3.2.

3.3.1. Fast Multipole Method (FMM)

The fast multipole method (FMM) is a numerical algorithm for the fast and approximated evaluation of sums of the form [51, 52]

$$u(\boldsymbol{r}) = \sum_{i=1}^{N} w_i \cdot K(\boldsymbol{r}, \boldsymbol{r}_i) \quad , \tag{3.25}$$

where $u(\boldsymbol{r})$ is the characteristic of interest at position $\boldsymbol{r}$ which can be calculated by summing the contributions of N target points with weights w_i and locations $\boldsymbol{r}_i$. Additionally, the application of the kernel $K(\cdot,\cdot)$ which describes the influence of a source on a target based on its position, is required. Sums in the form of Eq. (3.25) appear when considering

TU Bibliothek WIEN Your knowledge hub
Die approbierte gedruckte Originalversion dieser Diplomarbeit ist an der TU Wien Bibliothek verfügbar
The approved original version of this thesis is available in print at TU Wien Bibliothek.

various N-body problems, such as gravitational, electrical, or acoustical ones [52].

The main ideas of the FMM are a hierarchical partitioning of the input space and the approximation of the given kernel $K(\boldsymbol{r}_1, \boldsymbol{r}_2)$ using analytical expansions if $\boldsymbol{r}_1$ and $\boldsymbol{r}_2$ are far away from each other [52]. These two main ideas then allow for the evaluation of the characteristic of interest in an ensemble of N points at each point with a complexity of $O(N)$ instead of $O(N^2)$ as is required for the direct summation of Eq. (3.25) for each point of interest [52].

3.3.2. Inclusion of FMM in an EMC Workflow

The main idea for the inclusion of the FMM into the EMC workflow is the calculation of the force $\boldsymbol{F}$ which is acting on each particle, as superposition of two forces

$$\boldsymbol{F} = \boldsymbol{F}_b + \boldsymbol{F}_c \quad , \tag{3.26}$$

where $\boldsymbol{F}_c$ is the Coulomb force and $\boldsymbol{F}_b$ the background force, both of which will be explained in the following. First, the Coulomb force acting on a particle j, which is at position $\boldsymbol{r}_j$ and carries a charge q_j, can be calculated by adding up the force created by the interaction of the particle with all other carriers c and impurities i in the simulation space and is given by [46]

$$\boldsymbol{F}_c^j(\boldsymbol{r}_j) = q_j \left(\sum_{i=1}^{N_i} \frac{q_i}{4\pi\epsilon} \frac{\hat{\boldsymbol{r}}_{ji}}{\|\boldsymbol{r}_i - \boldsymbol{r}_j\|^2} + \sum_{\substack{c=1 \\ c\neq j}}^{N_c} \frac{q_c}{4\pi\epsilon} \frac{\hat{\boldsymbol{r}}_{jc}}{\|\boldsymbol{r}_c - \boldsymbol{r}_j\|^2} \right) \quad . \tag{3.27}$$

In the above equation, $q_{i/c}$ represents the charge, $N_{i/c}$ the total number, and $\boldsymbol{r}_{i/c}$ the position of the corresponding impurity or carrier, respectively. Lastly, $\hat{\boldsymbol{r}}_{ji/c}$ represents the unit vector along the force which stems from the interaction of the current particle and an impurity or carrier. Within this thesis, it is noted that Eq. (3.27) is of the form of Eq. (3.25) and can thereby be evaluated with the help of the FMM. Second, the background force results from the applied electric field $\boldsymbol{E}_{app}$ in bulk simulations and from the applied potential at the contacts and additional conditions at the boundaries for device simulations. While it is straightforward to evaluate $\boldsymbol{F}_b^j = q_j \cdot \boldsymbol{E}_{app}$ in bulk simulations, the calculation of the force within device simulations has to be performed by the solution of an adapted Poisson (Laplace) equation, which is not presented here.

Furthermore, the inclusion of the real-space particle-particle interactions into EMC bulk simulations, as presented in this section, does not require a drastic adaptation of the workflow shown in Fig. 3.1: First, at the beginning of each time step, $\boldsymbol{F}_c$ is updated by re-evaluating Eq. (3.27) with the help of the FMM. Second, for the determination of the force experienced by each particle, which is required for the motion of the particles and shown in the workflow in Fig. 3.3a, the superposition of $\boldsymbol{F}_c$ and $\boldsymbol{F}_b$, as shown in Eq. (3.26), is considered. Problems can arise due to the required re-evaluation of the force after each scatter event. As these events occur at random times within one time step for each particle and as the positions of all particles concurrently are only known between the time steps,

Die approbierte gedruckte Originalversion dieser Diplomarbeit ist an der TU Wien Bibliothek verfügbar
The approved original version of this thesis is available in print at TU Wien Bibliothek.
TU WIEN Bibliothek Your knowledge hub

an update of the Coulomb force after every scatter event is not possible. For that reason, in the scope of this thesis, $\boldsymbol{F}_c$ is only updated at the beginning of each time step and is not modified within a step.

Finally, in case the FMM is used for the c-c and c-i-interactions, a non-physical numerical heating of a simulated ensemble can appear [48]. The reason for this is the previously mentioned assumption that the Coulomb force which acts on a particle within one time step is approximated with the force acting on the particle at the beginning of the step. First, this discrete update of the Coulomb force allows for repulsive particles to get closer to each other than is physically possible when the force is updated in a continuous manner. Second, in case two particles are very close to each other at the time the Coulomb force is updated, their motion is effectively based on the resulting high forces throughout the entire time step instead of only during the short time the particles are close to each other. If the duration of the time step Δt is then chosen to be too long this can lead to non-physical high energies and velocities, which in turn lead to this numerical heating. To allow the choice of higher Δt within the scope of this thesis, a cut-off approach, which cuts off the force at a distance of $r_c = 1\,\text{nm}$, is applied during the calculation of $\boldsymbol{F}_c$ [48]. Mathematically, this means that, if the distance $\boldsymbol{r}$ between two particles fulfills $\|\boldsymbol{r}\| \geq r_c$ the Coulomb force is calculated with Eq. (3.27), as described earlier. On the other hand, if the distance is smaller than r_c, $\boldsymbol{F}_c$ is calculated with an adapted distance $\boldsymbol{r}_{adapted} = \boldsymbol{r} \cdot \frac{r_c}{\|\boldsymbol{r}\|}$, which fulfills $\|\boldsymbol{r}_{adapted}\| = r_c$ and is parallel to the initial vector distance ($\boldsymbol{r}_{adapted} \parallel \boldsymbol{r}$). This leads to a constant norm of the Coulomb force for all distances smaller than r_c, as can be seen in Fig. 3.8, and additionally, the direction of the force between two particles is not modified by this approach. Even though the discard of the rapidly changing high forces of particles with distances smaller than r_c enables the use of longer time steps, care has to be taken to avoid choosing a time step which is too long, as this still can lead to numerical heating.

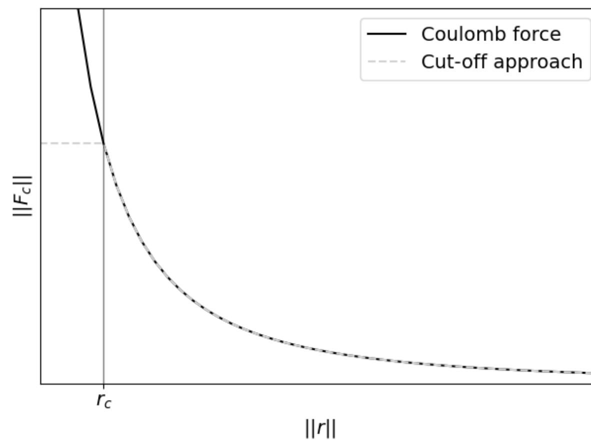

Figure 3.8.: Sketch of the approximation of the Coulomb force with the cut-off approach.

Die approbierte gedruckte Originalversion dieser Diplomarbeit ist an der TU Wien Bibliothek verfügbar
The approved original version of this thesis is available in print at TU Wien Bibliothek.
TU WIEN Bibliothek Your knowledge hub

4. Implementation

Within the scope of this thesis, a `C++` header-only library [53] was developed and implemented, whose main goal is to enable the simulation of various generic devices using the EMC method. Additional goals of the library are to enable the bulk simulation of various materials using a subgroup of the components of the library, and the inclusion of real-space particle-particle interactions which was implemented with the help of the FMM, as described in Section 3.3.2, and the external library `scalFMM` [32]. This chapter first provides an outline of the main ideas and components of the developed library for device simulations, followed by a more precise description of the different components. Finally, the applied components and adaptations for bulk simulations are presented.

4.1. Outline

An overview of the main components of the developed library and a simplified version of their relations is provided in Fig. 4.1. In the following paragraphs the main idea of each component is described.

The aim of the *Device Type* component is the description of the simulated electronic device. As discussed in Section 3.2.1, the characterization of a device requires the knowledge of material characteristics, the doping profile, and the positioning and types of the contacts at the surface of the device. A more precise description of this component, including its sub-components and a sample application, can be found in Section 4.2.

The *Poisson Solver* handles the calculation of the potential in the given *Device Type* by solving the Poisson equation given in Eq. (1.2). Implementation details of this component are discussed in Section 4.3.

The *Particle Handler* is responsible for the storage and handling of all simulated particles. Furthermore, each simulated particle belongs to a specific class of particles, a so-called *Particle Type*. This *Particle Type* determines the particle behavior during the simulation, such as how and if the particle moves and the corresponding particle characteristics, such as the charge and mass. Additionally, this component includes a *PM-Scheme* which provides the linking between the discrete grid and the continuous particle positions, as discussed in Section 3.2.3. A more precise description of this component and all its sub-components will be given in Section 4.4.

The *Simulation* component handles the execution of the EMC simulation as mentioned in the workflow in Fig. 3.5. It combines and applies all previously mentioned components.

TU WIEN Bibliothek Your knowledge hub
Die approbierte gedruckte Originalversion dieser Diplomarbeit ist an der TU Wien Bibliothek verfügbar
The approved original version of this thesis is available in print at TU Wien Bibliothek.

Additionally, it is also concerned with the storage of the specific settings and results of the ongoing simulation.

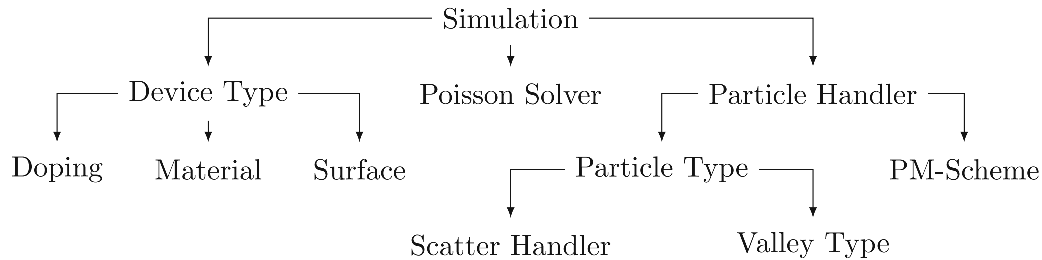

Figure 4.1.: Main components of the implementation and their (simplified) relations.

4.2. Device Type

The *Device Type* component describes the model of the simulated electronic device. Since one of the goals of this library is the ability to simulate various types of devices, the characterization of the device is kept as generic as possible. The only underlying assumptions for the model of the device within the library are a cuboid geometry with one corner being situated at the origin of the simulation space and the use of a uniform mesh for the discrete representation of the device. With the application of these assumptions a model for a device within this library is uniquely described by the following properties:

1. *Dimension:* Within the library one can either simulate devices in 2D or 3D. While a three-dimensional model of the device is more realistic, it requires more computational effort to simulate. Therefore, if the characteristics of the device allow discarding one dimension, a 2D model and simulation of the device is utilized. Although the two-dimensional model then simulates the same number of particles projected onto the 2D simulation space, the potential and electric field are only calculated in 2D, which decreases runtime.

2. *Geometry:* As previously stated, it is assumed that the geometry of the model of the device is a cuboid with one corner at the origin of the simulation space. To uniquely define the cuboid geometry under these assumptions, the only supplementary parameter which must be set is the position of the corner of the cuboid which is furthest away from the origin. Additionally, the spacing of the uniform mesh in each dimension has to be determined. Finally, if the simulation is performed in 2D, the virtual extent of the device in the discarded third dimension also needs to be set.

3. *Material:* The underlying semiconductor material is defined by the determination of material constants such as the permittivity and the density. Furthermore, also the temperature of the material has to be set. If no other temperature is provided, room temperature is assumed.

Die approbierte gedruckte Originalversion dieser Diplomarbeit ist an der TU Wien Bibliothek verfügbar
The approved original version of this thesis is available in print at TU Wien Bibliothek.
TU WIEN Bibliothek Your knowledge hub

4. *Doping:* The doping profile is uniquely defined in case the net amount of doping at each discrete mesh point is determined. The value of the net doping can be set by the user in the cuboid regions of the device which span from a given minimum corner (closest to the origin) to a maximum one, using the function `addConstantDopingRegion(minPos, maxPos, netDoping)`. Here `minPos` and `maxPos` are the positions of the previously mentioned minimum and maximum corner, respectively, and `netDoping` is the value for the net doping within this region.

5. *Surface:* On the surface of the simulated device, different types of contacts can be placed. For the characterization of a contact, its exact position, applied voltage, type, and all additional characteristics of interest have to be set. The implemented library offers functions which can add either Ohmic or Gate contacts. The addition of an Ohmic contact is performed with `addOhmicContact(boundPos, appliedVolt, minPos, maxPos)`, where `boundPos` defines the boundary at which the contact is added, `minPos` and `maxPos` define the extent of the contact on the given boundary, and `appliedVolt` defines the applied voltage at the contact. A gate contact is added in a similar way, with the determination of additional characteristics such as the thickness of the oxide `thickOx`, the dielectric constant of the oxide `dielOx` and the barrier height of the contact `barrierHeight`, leading to the function `addGateContact(boundPos, appliedVolt, minPos, maxPos, dielOx, thickOx, barrierHeight)`.

Two sketches of 2D models for specific devices are shown in Fig. 4.2, with one of them representing a PN-Junction and the other one a MOSFET. Furthermore, the code for the creation of the device shown in Fig. 4.2b within the developed library is given in Listing 4.1. In the presented code, first the dimension, the geometry, and the material of the created device are set. Subsequently, the doping regions are added one by one, by setting their minimal and maximal position and the net doping concentration (with n-doped regions being defined as positive net doping). Finally, the positions, applied voltages, and additional characteristics of the contacts are set.

TU Bibliothek. Die approbierte gedruckte Originalversion dieser Diplomarbeit ist an der TU Wien Bibliothek verfügbar. The approved original version of this thesis is available in print at TU Wien Bibliothek. Your knowledge hub

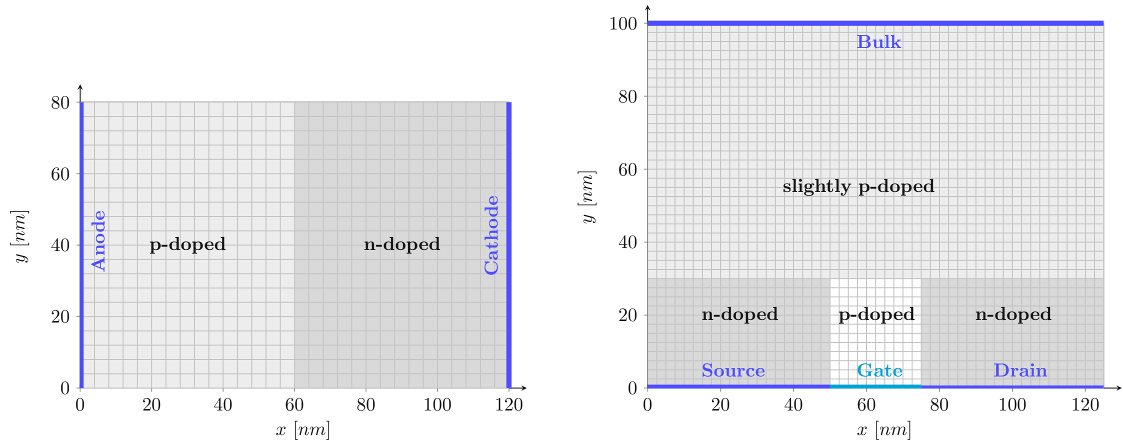

(a) PN-Junction.

(b) MOSFET.

Figure 4.2.: Sketches of exemplary generic devices with defined shape, discrete representations, doping profiles, and contacts.

```
const SizeType Dim = 2; // (1.) dimension

// (2.) geometry + (3.) material
std::array<double, Dim> maxCorner = {125e-9, 100e-9};
std::array<double, Dim> spacing = {1e-9, 1e-9};
emcMaterial<double> silicon = Silicon::getMaterial<double>();
emcDevice<double, Dim> mosfet{silicon, maxCorner, spacing};
mosfet.setDeviceWidth(1e-6); // set extent in 3rd dimension

// (4.) doping (input: minPos, maxPos, netDoping)
mosfet.addConstantDopingRegion({0, 30e-9}, {125e-9, 100e-9}, -5e23);
mosfet.addConstantDopingRegion({0, 0}, {51e-9, 30e-9}, 5e25);
mosfet.addConstantDopingRegion({51e-9, 0}, {75e-9, 30e-9}, -5e24);
mosfet.addConstantDopingRegion({75e-9, 0}, {125e-9, 30e-9}, 5e25);

// (5.) surface (order: bulk, source, gate, drain)
// (input: boundaryPosition, voltage, minPos, maxPos, add. param.)
mosfet.addOhmicContact(emcBoundaryPos::YMAX, 0, {0}, {125e-9});
mosfet.addOhmicContact(emcBoundaryPos::YMIN, 0, {0}, {51e-9});
mosfet.addGateContact(emcBoundaryPos::YMIN, 1, {51e-9}, {75e-9}, 3.9, 1.2e
    -9, silicon.getBandGap() / 2.);
mosfet.addOhmicContact(emcBoundaryPos::YMIN, 1, {75e-9}, {125e-9});
```

Listing 4.1: Example code to model the MOSFET-structure shown in Fig. 4.2b.

4.3. Poisson Solver

As already mentioned, the *Poisson Solver* is used to obtain the potential within the device by solving the Poisson equation, Eq. (1.2). Three different types of solutions of the

Die approbierte gedruckte Originalversion dieser Diplomarbeit ist an der TU Wien Bibliothek verfügbar
The approved original version of this thesis is available in print at TU Wien Bibliothek.
TU WIEN Bibliothek Your knowledge hub

before-mentioned equation are distinguished based on their underlying assumptions about the carrier concentrations and the boundary conditions: The first two types of solutions are based on the equilibrium and non-equilibrium assumptions, which are discussed in Section 3.2.2. While the last kind of solution of the Poisson solver is not used in the scope of this thesis, it represents the background potential Φ_b, which is required for the inclusion of the FMM and whose determination allows for the calculation of $\boldsymbol{F}_b$ in devices, as mentioned in Section 3.3.2.

Within the library this component is implemented as a purely abstract class which has three abstract member functions, each responsible for the calculation of one of the previously described solution types. This structure allows for the implementation of various customized solvers of the Poisson equation, which should be implemented as derived classes from the abstract base class. In the scope of this thesis only one solver was implemented, the iterative Successive-Over-Relaxation (SOR)-solver, whose derivation is shown in Appendix A.

4.4. Particle Handler

In general the *Particle Handler* is responsible for the storage and handling of all simulated particles. In this chapter, first the implementation of a particle in the developed library will be discussed in Section 4.4.1, followed by a more detailed description of the tasks and implementation of the *Particle Handler* in Section 4.4.2.

4.4.1. Particle Implementation

Each particle in the library has a corresponding position and is assigned to a so-called *Particle Type*, which represents a group of particles which share specific attributes and behaviors. In the library, the following behavior and attributes are determined by the corresponding *Particle Type*:

1. *Characteristics*: Each particle of a specific type possesses the same mass and charge, therefore these characteristics are stored by the associated *Particle Type* and not by each single particle. Additionally, two different kinds of *Particle Types* can be distinguished: The ones containing moving particles and those containing non-moving particles, which are referred to as moving and non-moving *Particle Types*, respectively. While non-moving particles, which are immobile during the simulation, are of interest in case the FMM is included for the representation of dopants (impurities), moving particles are required in all simulations as they represent the charge carriers, such as holes or electrons. In case a moving *Particle Type* is considered, additional characteristics describing the current motion of each particle of that type have to be stored, such as the particle's wave vector, its current energy, its remaining free flight time τ, and the index of the corresponding valley, subvalley, and doping region. Within the library, these characteristics are stored for each moving particle in an object of the class `emcParticle`, which is shown in Fig. 4.3a.

TU WIEN Bibliothek Your knowledge hub
Die approbierte gedruckte Originalversion dieser Diplomarbeit ist an der TU Wien Bibliothek verfügbar
The approved original version of this thesis is available in print at TU Wien Bibliothek.

2. *Initialization*: The *Particle Type* provides functionality to determine the number of particles to be initialized at the beginning of a simulation and an additional function which handles the initialization of a particle of this type. While in case of a non-moving *Particle Type* only the position of each particle has to be initialized, for moving *Particle Types* also the supplementary characteristics which are stored in an `emcParticle` object and describe the motion of the particle have to be initialized and stored.

3. *Dispersion relation*: Each moving *Particle Type* stores the dispersion relation for the corresponding particles. Within the framework, analytical bands are applied, meaning that the dispersion relation is represented by - and stored as - multiple valleys, as discussed in Section 2.1.1. While different types of pre-defined valleys are already implemented in the library, the user can also implement custom types of valleys. Generally, in the provided library, a valley can be derived from the abstract *Valley Type* base class, whose structure is shown in Fig. 4.3c. Essentially, the functionality given in this class allows for the determination of all important characteristics of a given valley: The effective masses and their averages, as described in Eqs. (2.12) and (2.13), the non-parabolicity factor α, the number of subvalleys (degeneracy) of the corresponding valley, and the value of the energy of the valley extrema. Additionally, functions which allow for the calculation of the norm of the wave-vector from the energy and vice versa have to be implemented. For the implementation of these functions for valleys with circular constant energy surfaces, for example, Eq. (2.9) is applied. Finally, in case of valleys with elliptic constant energy surfaces, function templates are provided for the coordinate transformation between the coordinate system used in the simulation and the ellipse coordinate system. A function template is also provided for the determination of the diagonal of the transformation matrix which is required for the Herring Vogt transformation, given in Eq. (2.15).

4. *Scattering Mechanisms*: Each *Particle Type* also provides a functionality for the addition and handling of scattering mechanisms. Within the library a scattering mechanism is implemented as a derived class from the abstract *Scatter Mechanism* class. This base class contains three virtual functions, as shown in Fig. 4.3b, which determine the name, the scatter rate, and the adaptations of the final state of a carrier after a scatter event with that mechanism. For the creation of a custom scattering mechanism these functions must be overwritten. Additionally, several pre-defined mechanisms are already implemented in the library such as acoustic intravalley scattering and optical intervalley scattering, described in Section 2.2.1. Furthermore, each *Particle Type* has an additional class which is responsible for the management of all mechanisms. This class is called *Scatter Handler* in the library and its responsibilities include the initial calculation of the tabulated scatter rates, the inclusion of self-scattering as described in Eq. (3.5), and the selection of the mechanism in the case of a scatter event as described by Eq. (3.6).

5. *Conditions at Ohmic contacts*: In case of moving particles, Ohmic contacts must be considered separately due to the condition that the number of particles close to these contacts is assumed to remain constant, as described in Section 3.2.1. For that

TU WIEN Bibliothek Your knowledge hub
Die approbierte gedruckte Originalversion dieser Diplomarbeit ist an der TU Wien Bibliothek verfügbar
The approved original version of this thesis is available in print at TU Wien Bibliothek.

reason each *Particle Type* containing moving particles has to possess a functionality to calculate the expected number of particles near a contact and, in case the number is too low, also a function for the initialization (injection) of new particles in that region has to be provided.

Finally, the simplified structure of the abstract implementation of the *Particle Type* is given in Fig. 4.3d. As with the other abstract classes, the main idea is to keep this class as generic as possible, to allow the usage of various custom *Particle Types*. Within the scope of this thesis moving electrons with different initial conditions and non-moving dopants (impurities) are used as *Particle Types*.

emcParticle <T>
+ k : array<T, 3>
+ energy : T
+ tau : T
+ idxValley : SizeType
+ idxSubValley : SizeType
+ idxRegion : SizeType

(a) Characteristics of single moving particle.

{abstract}
emcScatterMechanism<T>
-idxValley : SizeType
+getScatterRate(T, SizeType) = 0 : T
+scatterParticle(emcParticle<T> &, emcRNG &) = 0 : void
+getName() = 0 : string

(b) *Scatter Mechanism* base class.

{abstract}
emcAbstractValley <T>
+getEffMassDOS(T) = 0 : T
+getEffMassCond(T) = 0 : T
+getNonParabolicity() = 0 : T
+getBottomEnergy() = 0 : T
+getDegeneracyFactor() = 0 : SizeType
+getNormWaveVec(T) = 0 : T
+getVelocity(array<T,3>, T, SizeType) = 0 : array<T, 3>
+getVogtTransformationFactor() = 0 : array<T, 3>
+transformToDeviceCoord(SizeType, array<T,3>) = 0 : array<T,3>
+transformToEllipseCoord(SizeType, array<T,3>) = 0 : array<T,3>
+check() : void

(c) *Valley Type* base class.

{abstract}
emcAbstractParticleType <T,DeviceType>
-valleys : vector<emcAbstractValleys<T>*>
-scatterHandler : emcScatterHandler<T, DeviceType>
+getMass() = 0 : void
+getCharge() = 0 : void
+isMoved() = 0 : bool
+isInjected() = 0 : bool
+getInitialNrParticles(...) = 0 : T
+getExpectedNrParticlesAtContact(...) = 0 : T
+generateInitialParticle(...) : emcParticle<T>
+generateInjectedParticle(...) : emcParticle<T>
+addValley(...) : void
+addScatterMechanism(...) : void
+scatterParticle(...) : void

(d) Simplified *Particle Type* base class.

Figure 4.3.: Structure of selected classes which are connected to the implementation of particles within the library.

4.4.2. Tasks of Particle Handler

As previously mentioned, the *Particle Handler* is responsible for the storage and handling of all particles of every simulated *Particle Type*. In detail, this means that this class manages the following tasks:

1. *Initialization:* The *Particle Handler* performs the initialization of the particles by applying the functionality given by each *Particle Type*, which determines the number of initial particles and their initialization.

2. *Motion:* The motion of all moving particles during each time step Δt is performed by this class and follows the workflow given in Fig. 3.3a. As stated in Section 3.1.2 this motion consists of alternating drifts and scatter events, for which each *Particle Type* holds the information on the available valleys and scatter mechanisms. Additionally,

Die approbierte gedruckte Originalversion dieser Diplomarbeit ist an der TU Wien Bibliothek verfügbar
The approved original version of this thesis is available in print at TU Wien Bibliothek.
TU WIEN Bibliothek Your knowledge hub

particles which reach a device boundary during their motion are also handled by this class. Furthermore, prior to each drift event the force at the position of the particle needs to be determined; this is also performed by this class. It should be noted, that the implementation of the precise motion of the charge carriers, the handling of the boundary conditions and the determination of the force can vary depending on the implemented *Particle Handler*.

3. *Assignment:* As described in Section 3.2.3 the link between the continuous particle position and the discrete representation of the device is crucial for EMC-simulations and is performed with a PM-Scheme. Within the code, the base class of this scheme contains virtual functions which enable the assignment of the particles to the discrete coordinates and facilitate the calculation of the force at a continuous particle position, based on an electric field which is calculated at discrete points. All three PM-Scheme mentioned in Section 3.2.3 are implemented within the library.

4. *Ohmic Contacts:* The *Particle Handler* ensures that the number of particles close to Ohmic contacts is kept constant. With the use of the functions which are provided by each *Particle Type*, the expected number of particles are calculated and if not enough particles are in the corresponding region, additional particles of the specific type are injected. In case excess particles are found close to the contacts, these particles are removed.

In summary, the abstract *Particle Handler* class allows for the implementation of various customized derived classes. Additionally, within the developed library different types of this class are already implemented. The implementations which are used within the scope of this thesis, differ in the way the force, which is acting on the particles, is calculated. The first implemented handler is used for classical device simulations and is called *Basic Particle Handler*. For this implementation the force acting on the particles is determined by the solution of the Poisson equation as described in Section 3.2.2, particle-particle interactions are not considered, and the boundary conditions are treated as described for all device boundary types in Section 3.2.1. Moreover, a *Particle Handler* which includes the carrier-carrier interactions with the help of the FMM and the external library `scalFMM` is implemented, but not used in the scope of the thesis.

4.5. Adaptations for Bulk Simulations

As described in Chapter 3, only a subgroup of the components applied for device simulations is essential for bulk simulations. This observation is also utilized in the developed library by reusing parts of the developed components for device simulations to perform bulk simulations. While, for example, the *Poisson Solver*, *PMScheme*, and *Simulation* components are not necessary for bulk simulations, the *Particle Type*, a customized *Particle Handler*, and parts of the *Device Type* component can be reused for these types of simulations. In this setting, the *Device Type* component describes the simulation space, the material, and the doping concentration in the material, which is assumed to be constant. Furthermore, the customized *Particle Handlers* resemble the ones used in device simulations, but they

TU Bibliothek Die approbierte gedruckte Originalversion dieser Diplomarbeit ist an der TU Wien Bibliothek verfügbar
The approved original version of this thesis is available in print at TU Wien Bibliothek.

discard some of the functionality not needed in bulk simulations as the *PM-Scheme*. Additionally, instead of applying the device boundary conditions discussed in Section 3.2.1, periodic boundary conditions are used on the surface of the defined simulation space so that this space represents an infinite bulk of the given material. Finally, as described in Section 3.1, the force acting on the particles stems from a homogeneous applied electric field. In the simulations, the user can set the direction and strength of this field.

Within this thesis, two types of customized *Bulk Particle Handlers* are used: The first one, termed *Basic Bulk Particle Handler*, is applied for classical bulk simulations as described in Section 3.1. The second customized *Bulk Particle Handler*, the *FMM Bulk Particle Handler*, differs from the one previously described by including the full classical real-space particle-particle interactions with the help of the external library `scalFMM`, as described in Section 3.3.2. It is noteworthy, that the periodic boundary conditions assumed for bulk simulations also must be considered for the calculation of the Coulomb force. The library `scalFMM` implicitly implements these boundary conditions, by considering not only the particles in the simulation space but also a specific number of copies of the simulation space and all particles in it, for the calculation of $\boldsymbol{F}_c$. In the implementation, the number of considered copies of the simulation space depends on the parameter `nbLevelsAboveRoot` which can take values between -1 and infinity. Figure 4.4 sketches the arrangement of the simulation space (gray) and all its copies in two dimensions for the lowest values of `nbLevelsAboveRoot`. In `scalFMM`, three dimensions must be used, leading to a total of 27 simulation boxes if `nbLevelsAboveRoot`$= -1$, 216 if `nbLevelsAboveRoot`$= 0$, and 1 728 ones if `nbLevelsAboveRoot`$= 1$.

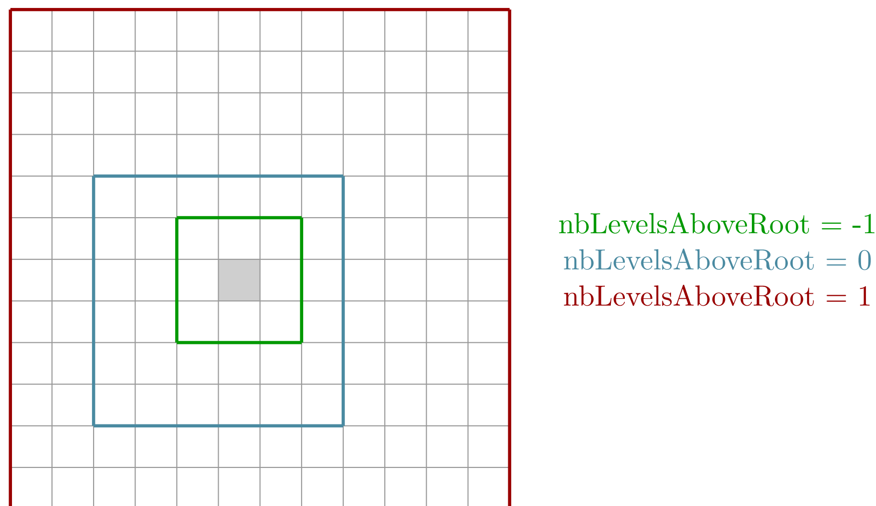

Figure 4.4.: Sketch of the periodicity in `scalFMM` in 2D with the gray box representing the simulation space and `nbLevelsAboveRoot` being a parameter that determines the number of copies of the simulation box.

Die approbierte gedruckte Originalversion dieser Diplomarbeit ist an der TU Wien Bibliothek verfügbar
The approved original version of this thesis is available in print at TU Wien Bibliothek.
TU WIEN Bibliothek Your knowledge hub

5. Applications

This chapter provides applications of the library which is developed within the scope of this thesis. It should be noted that, as this library is kept quite generic, these shown applications are only examples with neither the devices nor the simulated materials being restricted to the shown examples.

The first applications, presented in Section 5.1, are silicon-based structures. As the characteristics of silicon are well investigated, these simulations are used to verify the results of the developed simulator by comparing them with results from experiments and other established simulators. Furthermore, tests with the inclusion of the FMM into the EMC workflow, as described in Section 3.3.2, are performed. Subsequently, in Section 5.2, simulations of a monolayer of the 2D semiconductor molybdenum disulfide (MoS_2) are demonstrated. As this two-dimensional material is currently heavily investigated, these simulations show the relevance of the developed simulation tool to an active scientific field of research.

5.1. Silicon (Si)

Silicon is the most applied material for the fabrication of semiconductor devices. The band structure of bulk silicon is given in Fig. 5.1a while its first Brillouin zone, which is identical to that of GaAs, can be seen in Fig. 2.1a. In the band structure, one can see silicon's valence band maximum at the $\mathbf{\Gamma}$-point and its conduction band minimum in the path between the $\mathbf{\Gamma}$- and $\boldsymbol{X}$-points. Additionally, local minima of the conduction band can be seen (at $\boldsymbol{L}$- and $\mathbf{\Gamma}$-points), but as these have energies which are significantly higher than the one of the global minima, they do not contribute to the electron transport, even at high fields [38]. These observations indicate that, for the simulation of electron transport in this material, it is sufficient to approximate the valleys around the global minima with the analytical band approximation, as described in Section 2.1.1. Due to the symmetry of the Brillouin zone, six equivalent subvalleys around the global minima appear. All of the subvalleys, including their elliptic constant-energy surfaces are shown in Fig. 5.1b. Moreover, the characteristics of the approximated valleys are given in Table 5.1.

m_l $[m_0]$	m_t $[m_0]$	α $[eV^{-1}]$
0.916	0.196	0.5

Table 5.1.: Parameters of the approximated silicon valleys.

Die approbierte gedruckte Originalversion dieser Diplomarbeit ist an der TU Wien Bibliothek verfügbar
The approved original version of this thesis is available in print at TU Wien Bibliothek.
TU WIEN Bibliothek Your knowledge hub

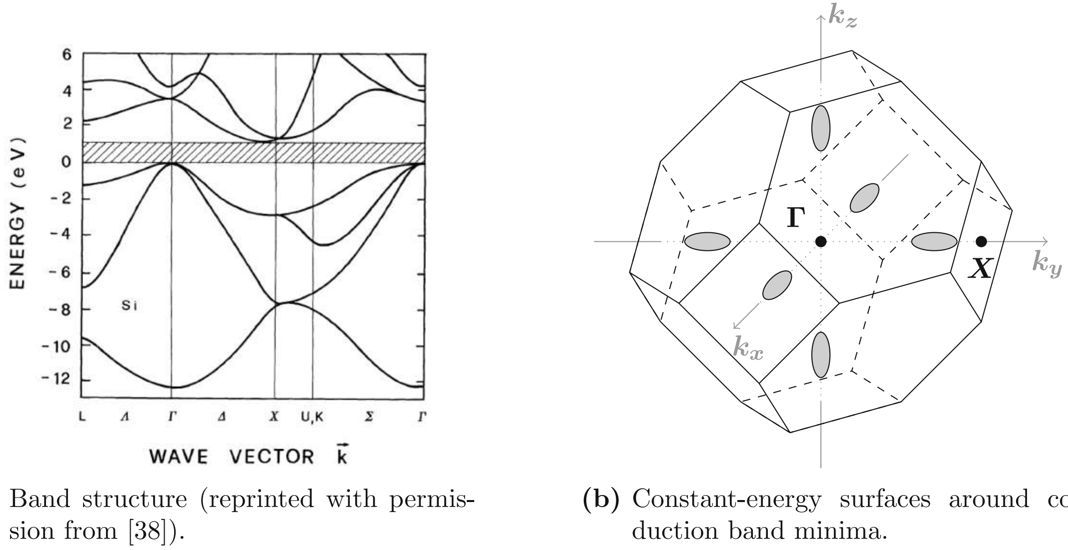

(a) Band structure (reprinted with permission from [38]).

(b) Constant-energy surfaces around conduction band minima.

Figure 5.1.: Characteristics of Silicon in $\boldsymbol{k}$-space.

The dominant scatter mechanisms in silicon are intravalley acoustic scattering and zeroth and first order intervalley optical scattering. The characteristics and calculations of scatter rates for the first two mechanisms have already been discussed in Section 2.2, with the only missing parameter being half of the density of states, which is given for three-dimensional materials with the applied non-parabolic band approximation, described in Section 2.1.1, by [2]

$$N_{3D}(E) = \frac{(2m_d)^{3/2}}{4\pi^2\hbar^3}\sqrt{E(1+\alpha E)}(1+2\alpha E) \quad . \tag{5.1}$$

The final scatter mechanism, first order intervalley optical scattering, is an inelastic and isotropic mechanism, whose scatter rate is given by [2]

$$\Gamma^{Si}_{op_1}(n,\boldsymbol{k}) = \frac{\sqrt{2m_d^5}\, D_{if}^2 Z_f}{\pi\hbar^5\rho\omega_{if}}\left[n(\omega_{if}) + \frac{1}{2} \mp \frac{1}{2}\right] \cdot \\ \left\{\sqrt{E_f(1+\alpha E_f)E(1+\alpha E)} + E_f(1+\alpha E_f)(1+2\alpha E_f)\right\}\Theta(E_f) \quad , \tag{5.2}$$

All parameters used for the calculation of this scatter rate have already been used in Eq. (2.21), and are therefore already described there. Additionally, as in Eq. (2.21) the upper sign is used for the absorption and the lower one for the emission of a phonon. It should also be noted that for silicon all included valleys have their minima at the same energy, which leads to $\Delta E_{fi} = 0$ for any considered final and initial valley [2]. Moreover, for silicon, two types of intervalley scattering mechanisms are distinguished: Either the particle scatters to the only valley which lies on the same axis as the initial valley, which is called *g-type*, or it scatters to a valley on another axis, which is called *f-type* [2]. Both

Die approbierte gedruckte Originalversion dieser Diplomarbeit ist an der TU Wien Bibliothek verfügbar
The approved original version of this thesis is available in print at TU Wien Bibliothek.
TU WIEN Bibliothek Your knowledge hub

types of intervalley scattering are visualized in Fig. 5.2a. Finally, the parameters for all described scatter mechanisms for silicon are presented in Table B.1 and the scatter rates for each type of the three dominant scatter mechanisms and their comparison to the resulting rates of Vasileska et al. [2] are plotted in Fig. 5.2.

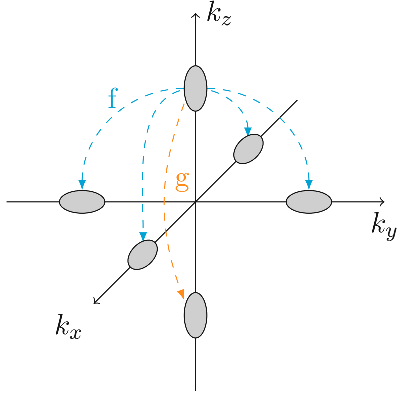

(a) Types of intervalley scattering.

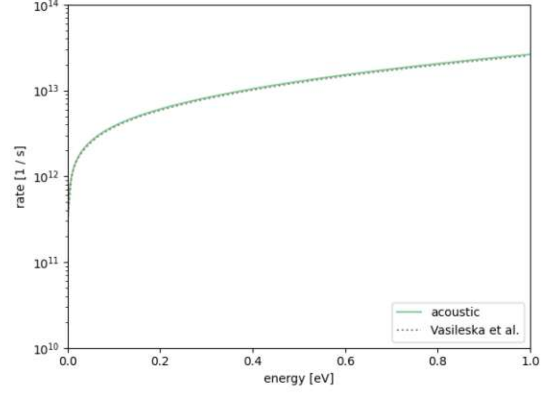

(b) Acoustic scatter rate.

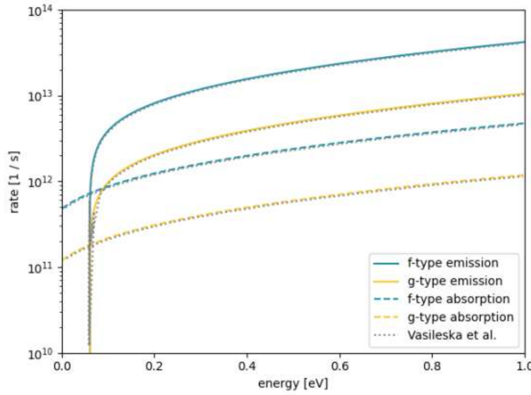

(c) Zero-th order intervalley optical scatter rates.

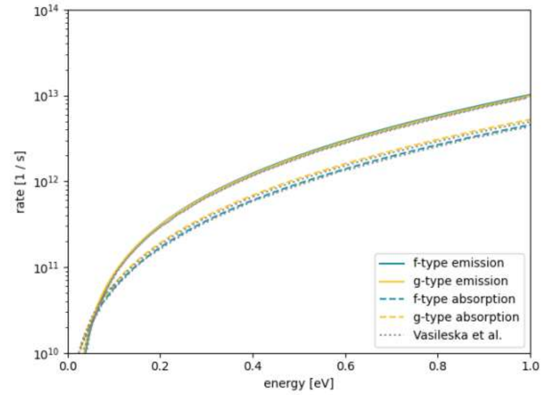

(d) First order intervalley optical scatter rates.

Figure 5.2.: Scattering mechanisms in silicon and comparison to the resulting scatter rates of Vasileska et al. [2].

5.1.1. Bulk Simulation

As a first test of the developed library and the applied silicon model, bulk silicon is simulated with the use of the *Basic Bulk Particle Handler* and 10 000 electrons. The initialization of these particles is performed by applying random numbers, as mentioned in Section 3.1.1. First, the initial energy of the particles is assigned using Eq. (3.1). Subsequently, the corresponding subvalley and the initial wave-vector direction are also selected at random with each possible direction and subvalley having the same probability. Once all particles are initialized, a homogeneous electric field is applied and the response from the particles is

Die approbierte gedruckte Originalversion dieser Diplomarbeit ist an der TU Wien Bibliothek verfügbar
The approved original version of this thesis is available in print at TU Wien Bibliothek.
TU WIEN Bibliothek Your knowledge hub

tracked.

At first the transient behavior of this ensemble of electrons is investigated by calculating the time-dependent ensemble average of the drift velocity and the energy. The results for electric fields with a strength of 2 kV/cm, 5 kV/cm, 10 kV/cm, and 20 kV/cm are provided in Fig. 5.3. They show that after the transient state a steady-state is reached for the ensemble velocity and energy, as is discussed in Section 3.1.3. Additionally, a velocity overshoot can be observed for high applied electric fields in Fig. 5.3a. The reason for these overshoots is that the scattering rates for particles with smaller energies are quite low, which allows the particles to gain energies higher than the steady-state velocities. This behavior proceeds until the particles reach high enough energies and the increasing scattering rates ultimately lead to the final steady-state drift velocity.

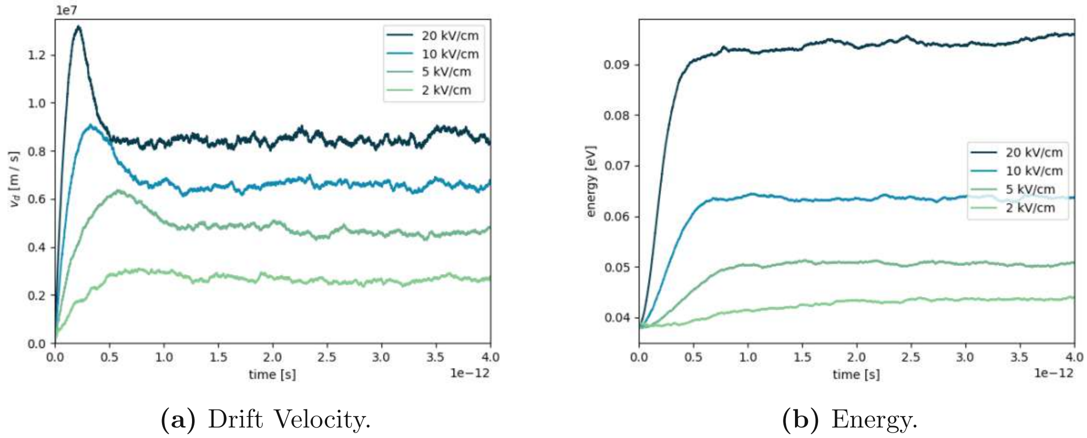

(a) Drift Velocity. **(b)** Energy.

Figure 5.3.: Ensemble averages of characteristics of interest for silicon simulations with various applied electric fields in direction $\langle 1\,0\,0 \rangle$ at 300 K.

Subsequently, the steady state behavior of the drift velocity is compared to the experimental results from Canali et al. [3]. For this, electric fields with varying strengths are applied in $\langle 1\,0\,0 \rangle$ and $\langle 1\,1\,1 \rangle$ directions at different temperatures. The results of that comparison are shown in Fig. 5.4 and it is evident that the resulting drift velocities of the newly developed tool are in good agreement with the experimental results. Furthermore, the plot shows that the results of this work reproduce the temperature dependence of v_d, as well as the anisotropic behavior of the electron transport in silicon. In the simulations, the temperature dependence of v_d is introduced by the temperature dependence of the scatter rates, as can be seen in Eqs. (2.20), (2.21) and (5.2). Moreover, the dependence of the investigated parameter on the direction of the applied field in the simulations arises from the elliptic constant-energy surfaces of the subvalleys and their varying orientation with regards to the applied field [3].

Die approbierte gedruckte Originalversion dieser Diplomarbeit ist an der TU Wien Bibliothek verfügbar
The approved original version of this thesis is available in print at TU Wien Bibliothek.
TU WIEN Bibliothek Your knowledge hub

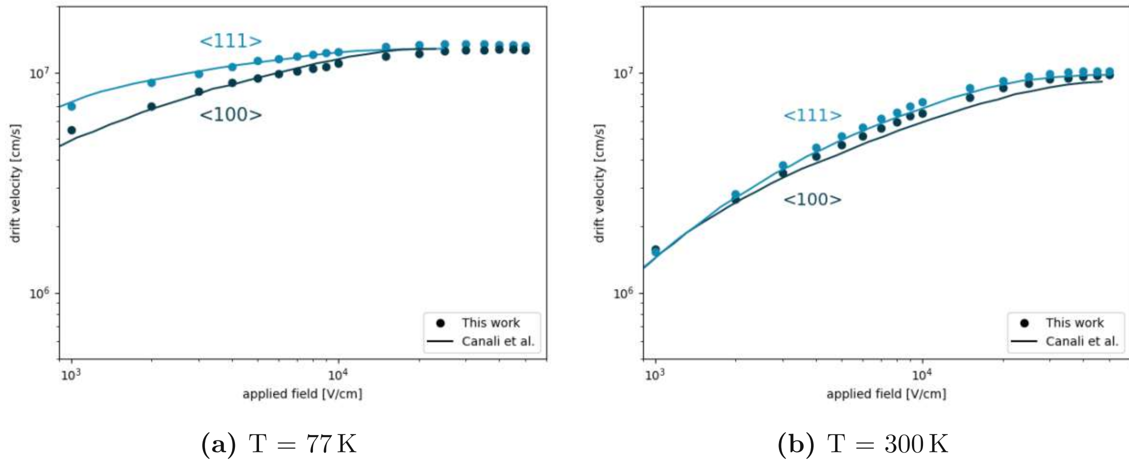

(a) T = 77 K

(b) T = 300 K

Figure 5.4.: Electron drift velocity in silicon with varying applied electric fields parallel to the $\langle 1\,1\,1 \rangle$ or $\langle 1\,0\,0 \rangle$ directions. Furthermore, the results are compared to the experimental results from Canali et al. [3].

5.1.2. Bulk Simulation Including FMM

The real-space Coulomb interactions are included in the bulk simulations with the help of the FMM, as described in Section 3.3.2 and as implemented in the *FMM Bulk Particle Handler*. The force acting on the particles in these simulations is generated by the applied electric field and by the Coulomb force which considers the classical interaction between all particles, as shown in Eq. (3.27). Additionally, for all simulations, in which the real-space Coulomb interactions are included, two *Particle Types* are utilized, moving electrons and non-moving active n-type dopants (impurities). Within the simulation, both particle types are distributed randomly in the simulation space with the number of the particles being calculated with the selected doping concentration. Finally, as mentioned in Section 4.4.2, the periodic boundary conditions, which are required for bulk simulations, are incorporated in the calculation of $\boldsymbol{F}_c$ by considering the interaction between the simulated particles and a specific number of copies of all simulated particles outside of the simulation space. In this simulation a value of 1 is used for `nbLevelsAboveRoots` which leads to a total of 1 728 copies of the simulation box.

In this section, the cooling of hot ensembles of electrons at 3 000 K in n-doped bulk silicon samples, with varying doping concentration and without any applied electric background field is simulated. First, the behavior of the ensemble in silicon with a n-type doping concentration of $1 \times 10^{18}\,\mathrm{cm}^{-3}$ with and without the application of the cut-off approach, which is described in Section 3.3.2, is compared. In Fig. 5.5a the results without the application of the cutoff approach are shown and it can be seen that for all applied time steps, which are varied between 0.05 fs and 0.5 fs a numerical increase in the ensemble energy can be observed, instead of the expected decrease in this characteristic. The reason for the increase is the approximation of the force within one time step being the force acting on each particle at the beginning of the step and the chosen Δt being way too long,

TU Bibliothek WIEN Your knowledge hub
Die approbierte gedruckte Originalversion dieser Diplomarbeit ist an der TU Wien Bibliothek verfügbar
The approved original version of this thesis is available in print at TU Wien Bibliothek.

thereby leading to numerical heating, as discussed in Section 3.3.2. Moreover, this increase happens in a very sharp manner (from one step to the next one) which is expected as it is caused by particles getting unrealistically close to each other and then experiencing very high forces for one whole time step, which is based on the discrete approximation of the Coulomb force as discussed in Section 3.3.2. In case the cut-off approach, which discards the rapidly changing high forces for distances below the cutoff radius of 1 nm, is applied, the ensemble average of the energy decreases with time, as expected. Additionally, it can be observed that the resulting development of the ensemble energy of the hot ensemble can still depend on the selected time step, which will be analyzed in more details in the following.

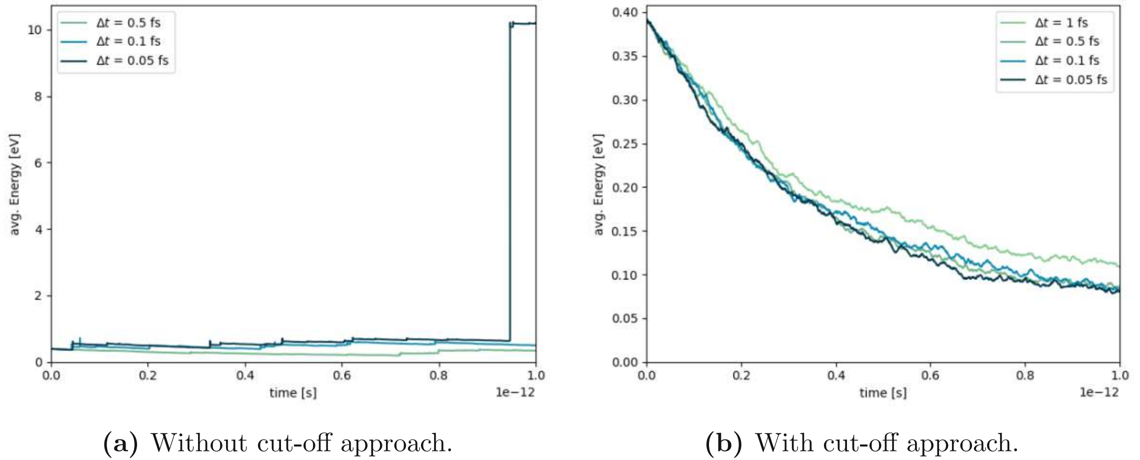

(a) Without cut-off approach.

(b) With cut-off approach.

Figure 5.5.: Effect of the cut-off approach for the cooling of a hot ensemble of electrons in silicon with a n-doping of $1 \times 10^{18}\,\mathrm{cm}^{-3}$.

To analyze the ability of the EMC method, with the implemented particle-particle interactions and the applied cut-off approach, to reproduce the expected steady-state ensemble energy of the hot ensemble, the results are compared to the ones of the EMC simulations without the inclusion of the particle-particle interactions, as described in Section 3.1, where the inelastic phonon scatter mechanisms are responsible for the cooling and which is termed `without FMM` in the following. The results of this comparison with varying doping levels of the simulated material and different applied time steps can be seen in Fig. 5.6. In Figs. 5.6a and 5.6b one can see that for lower doped samples the evolution of the ensemble energy in time for all applied Δt is similar to the one without the application of real-space particle-particle interactions. For higher doped samples, as shown in Figs. 5.6c and 5.6d, a numerical heating can be seen for higher values of Δt. This numerical heating is only observed at higher doping levels, as with increasing amount of doping, the mean distance between the particles decreases. As the average distance between carriers is reduced, the effect of small movements of other particles on the force which is felt by one carrier is larger and the error which is created due to the approximation of the force throughout one step being constant is increased, as described in Section 3.3.2. Hence, the upper limit for the selected Δt in case real-space particle-particle interactions with the cut-off approach are

Die approbierte gedruckte Originalversion dieser Diplomarbeit ist an der TU Wien Bibliothek verfügbar
The approved original version of this thesis is available in print at TU Wien Bibliothek.
TU WIEN Bibliothek Your knowledge hub

applied, depends on the doping concentration which is considered. In these simulations, it can be observed that for a doping of $1 \times 10^{13}\,\mathrm{cm}^{-3}$ and $1 \times 10^{15}\,\mathrm{cm}^{-3}$ a time step of 5 fs is sufficient to avoid numerical heating. However, for a doping concentration of $1 \times 10^{17}\,\mathrm{cm}^{-3}$ a time step below 1 fs and for a doping level of $1 \times 10^{18}\,\mathrm{cm}^{-3}$ a time step Δt below 0.05 fs is essential, to obtain the expected steady-state ensemble energy.

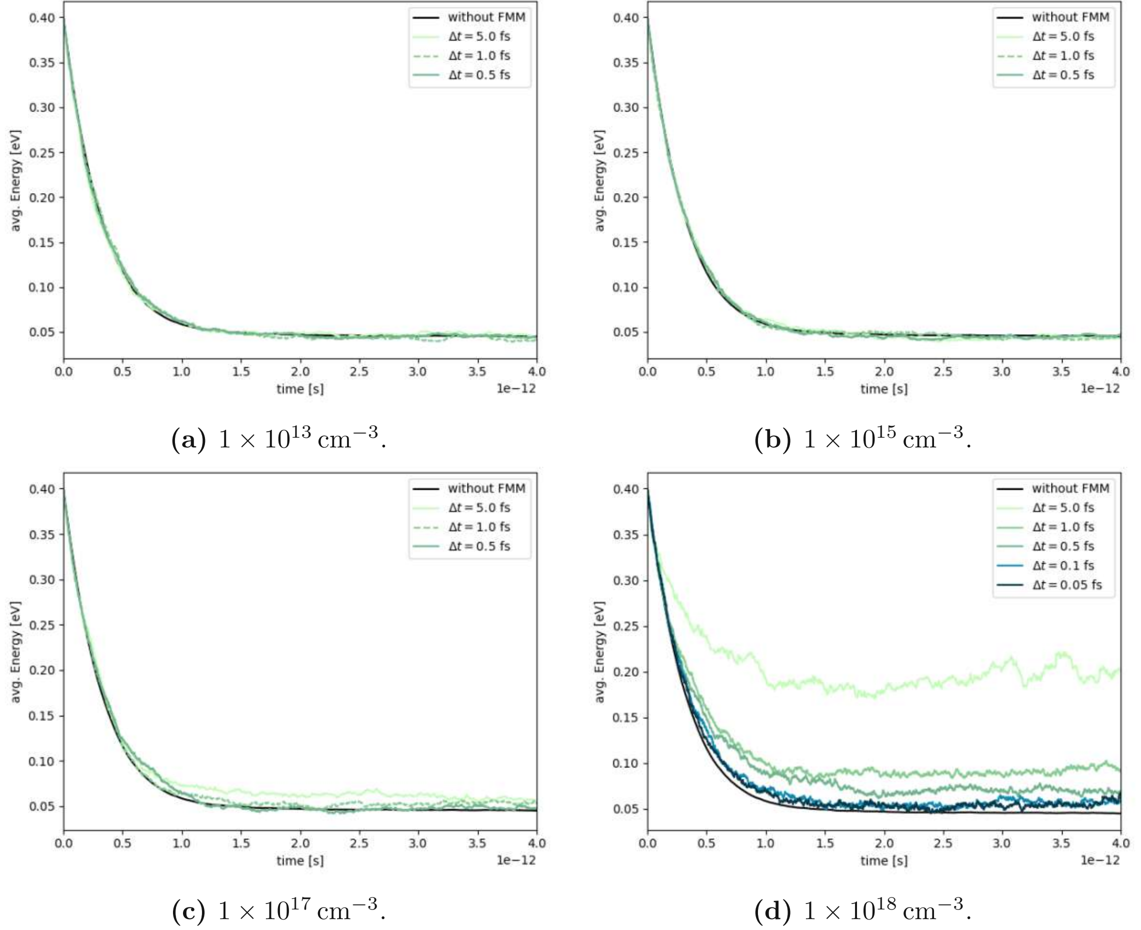

(a) $1 \times 10^{13}\,\mathrm{cm}^{-3}$.

(b) $1 \times 10^{15}\,\mathrm{cm}^{-3}$.

(c) $1 \times 10^{17}\,\mathrm{cm}^{-3}$.

(d) $1 \times 10^{18}\,\mathrm{cm}^{-3}$.

Figure 5.6.: Cooling of a hot electron ensemble at different doping concentrations, using 200 electrons and ions for the averaging and 1 728 copies of every particle for the calculation of $\boldsymbol{F}_c$.

5.1.3. MOSFET

The developed library is subsequently applied for the simulation of the n-channel MOSFET-structure which is sketched in Fig. 5.7 and whose implementation within the code is shown in Listing 4.1. This device is chosen for the comparison of the results to `CEMC`, the `C`-based code on which the developed library is based. As in `CEMC`, the NEC scheme is used for the simulations and the included scatter mechanisms are acoustic intravalley, zero-th order optical intervalley, and ionized impurity scattering. While the first two mechanisms have

Die approbierte gedruckte Originalversion dieser Diplomarbeit ist an der TU Wien Bibliothek verfügbar
The approved original version of this thesis is available in print at TU Wien Bibliothek.
TU WIEN Bibliothek Your knowledge hub

already been discussed for silicon, ionized impurity scattering approximates the interaction between carriers and impurities, as mentioned in Section 3.3, and is included as an elastic mechanism, whose rate is calculated using Eq. (3.24). Moreover, as in `CEMC`, only electrons are used within these simulations. Additionally, all simulations in this chapter are performed for a total simulation time of $t_s = 10\,\text{ps}$ using a time step of $\Delta t = 0.15\,\text{fs}$ and a selected transient time of 5 ps. Finally, for all simulations, the voltages at the source and bulk contact, V_s and V_b, are set to 0 V and the applied voltages at the gate and drain, V_g and V_d, are varied between 0 V and 1 V.

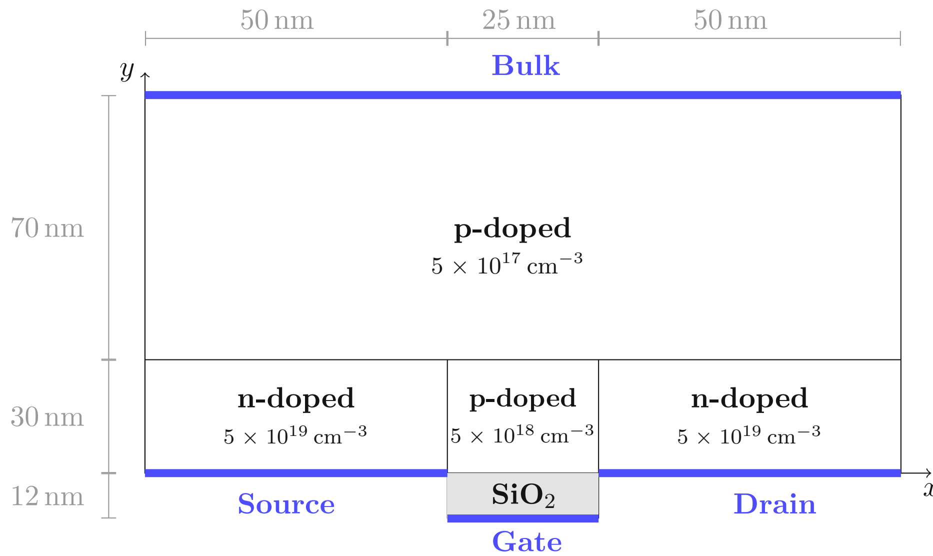

Figure 5.7.: Sketch of the geometry of the simulated MOSFET-structure.

At the beginning of the simulation the device is assumed to be in equilibrium, meaning that all applied voltages are neglected and the carrier concentrations are assumed to follow Eqs. (3.19) and (3.20) as discussed in Section 3.2.2. The resulting equilibrium potential for the simulated MOSFET structure is shown in Fig. 5.8a, in which a potential barrier between the source and the drain region can be seen, which hinders the carriers from traveling from one region to the other. Based on the calculated equilibrium potential, the particles are initialized using Eq. (3.19) for the determination of the initial number of particles close to each discrete grid point. The resulting equilibrium particle concentration which is calculated with the NEC scheme, is then shown in Fig. 5.8b. It can be seen that initially all electrons are placed within the n-doped drain and source regions which span from $(0\,\text{nm}, 0\,\text{nm})$ to $(50\,\text{nm}, 30\,\text{nm})$, and from $(75\,\text{nm}, 0\,\text{nm})$ to $(125\,\text{nm}, 30\,\text{nm})$, respectively.

Once the particles are initialized, the device simulation workflow, as described in Fig. 3.5 can proceed, until all time steps, in which the particle location, the potential, and the elec-

Die approbierte gedruckte Originalversion dieser Diplomarbeit ist an der TU Wien Bibliothek verfügbar
The approved original version of this thesis is available in print at TU Wien Bibliothek.
TU WIEN Bibliothek Your knowledge hub

tric field are updated, are complete. For the calculation of the final electron concentration and potential a time-average over all occurring concentrations and potentials within the steady-state phase is applied, as described in Section 3.1.3. An exemplary result for the final potential and electron concentration in case $V_d = V_g = 1\,\mathrm{V}$ can be seen in Fig. 5.9. In Fig. 5.9a it can be seen that due to the applied voltages, the potential barrier between the source and the drain region vanishes. Additionally, Fig. 5.9b shows that the electron concentration between the source and the drain, between $x = 50\,\mathrm{nm}$ and $x = 75\,\mathrm{nm}$, is not zero anymore, indicating a particle flow between these regions, which is enabled and controlled by the applied V_g and V_d. The effect of these applied voltages on the resulting potential within the device and the current I_d which is measured at the drain contact will be analyzed in the following.

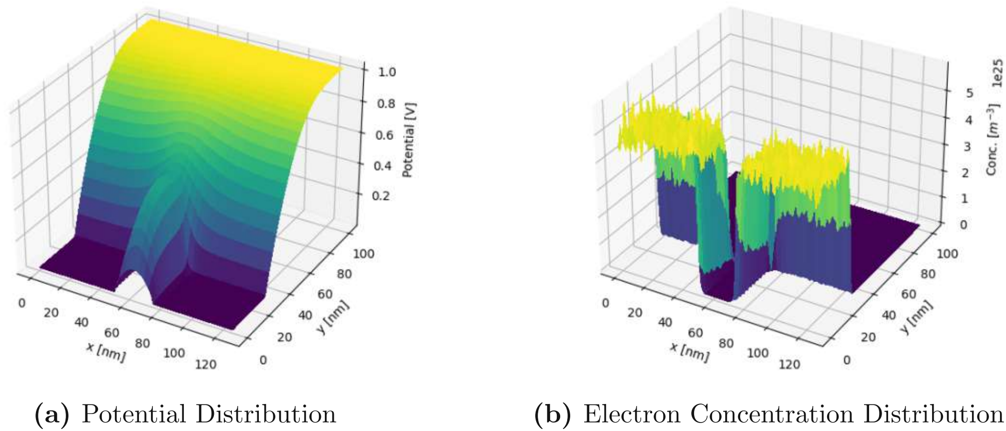

(a) Potential Distribution **(b)** Electron Concentration Distribution

Figure 5.8.: Equilibrium characteristics of the simulated silicon MOSFET.

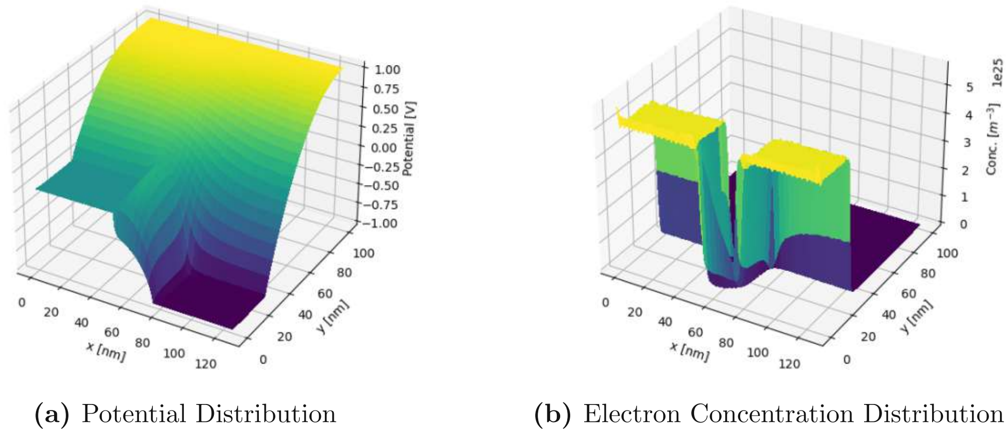

(a) Potential Distribution **(b)** Electron Concentration Distribution

Figure 5.9.: Characteristics of the simulated silicon MOSFET with $V_d = V_g = 1\,\mathrm{V}$.

To present the effect of an applied positive drain or gate voltage on the potential, the

Die approbierte gedruckte Originalversion dieser Diplomarbeit ist an der TU Wien Bibliothek verfügbar
The approved original version of this thesis is available in print at TU Wien Bibliothek.
TU WIEN Bibliothek Your knowledge hub

cross-section of the potential at $y = 0\,\text{nm}$, with various applied gate and drain voltages, is provided in Fig. 5.10. Additionally, the cross-section of the potential is compared to the results of `CEMC`, which show a good agreement with the outcome of the newly developed tool. Furthermore, Fig. 5.10a shows that a positive applied gate voltage V_g lowers the potential barrier between the drain and the source contacts. Hence, V_g can be utilized to enable and control the carrier flow. In case the potential barrier is lowered enough, a particle flow between the source and drain is enabled; on the other hand, if the barrier is too high this flow cannot occur. Moreover, in Fig. 5.10b one can see the effect of an increasing V_d on the potential at $y = 0$, which also leads to a drain-induced barrier lowering. Varying this parameter can then control the amount of described particle flow in case the barrier is low enough so that flow is enabled.

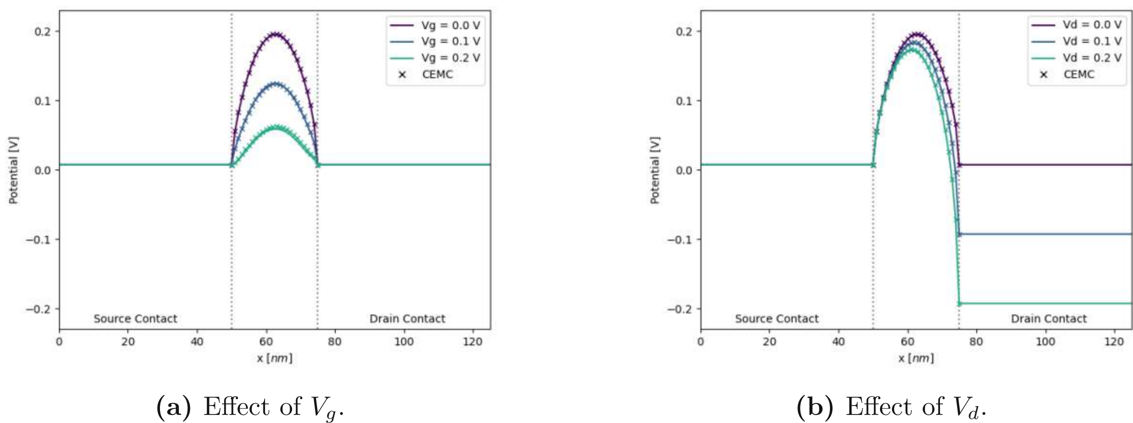

(a) Effect of V_g.

(b) Effect of V_d.

Figure 5.10.: Effect of applied potential at the gate and the drain on the potential cross-section at $y = 0\,\text{nm}$; if not stated otherwise, $V_g = V_d = 0\,\text{V}$. Additionally, results of the `CEMC` code are provided for comparison.

The final resulting current at the drain contact I_d, which is calculated using Eq. (3.22), for various applied voltages at the drain and gate contact between 0 V and 1 V, can be seen in Fig. 5.11. Moreover, for the comparison of the developed tool and `CEMC`, also the resulting drain current from simulations with `CEMC` is included and it can be seen that these results are in good agreement with the ones simulated using the framework developed in this thesis.

Die approbierte gedruckte Originalversion dieser Diplomarbeit ist an der TU Wien Bibliothek verfügbar
The approved original version of this thesis is available in print at TU Wien Bibliothek.
TU WIEN Bibliothek Your knowledge hub

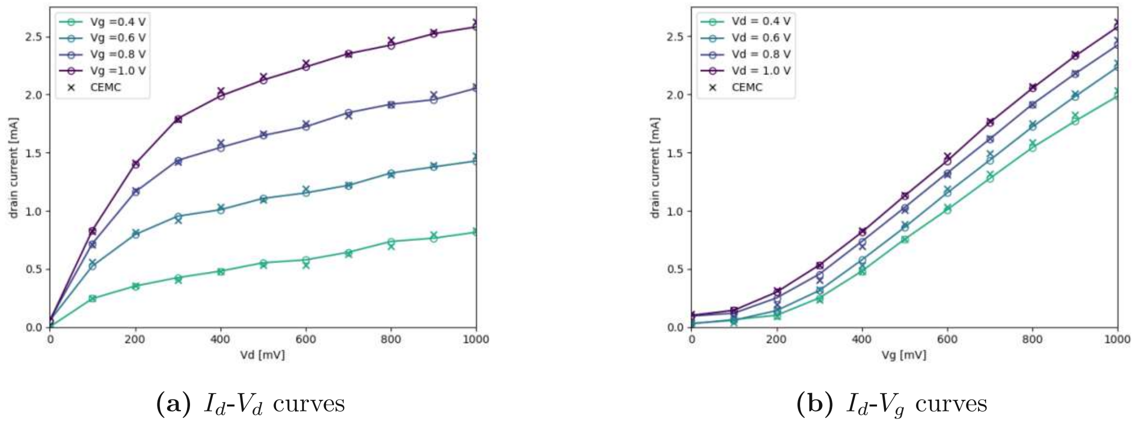

(a) I_d-V_d curves

(b) I_d-V_g curves

Figure 5.11.: Resulting I-V characteristics of the simulated MOSFET (lines and circles) and comparison to the results of CEMC (crosses).

5.2. Monolayer Molybdenum Disulfide (ML-MoS_2)

The second application of the developed library, which is used to demonstrate its capability, is the simulation of monolayer molybdenum disulfide (ML-MoS_2), a highly investigated 2D-material, which offers a theoretical direct band gap of 1.8 eV [54], a high on-off current ratio of approximately 10^8, and can withstand high elastic deformations. Due to these, and other beneficial properties of this material, it has gained traction in many fields including sensing, opto-electronics, and biochemistry [55]. The two-dimensional structure of this material in real- and **k**-space can be observed in Fig. 5.12. Additionally, Fig. 5.12b includes selected symmetry points in the first Brillouin zone.

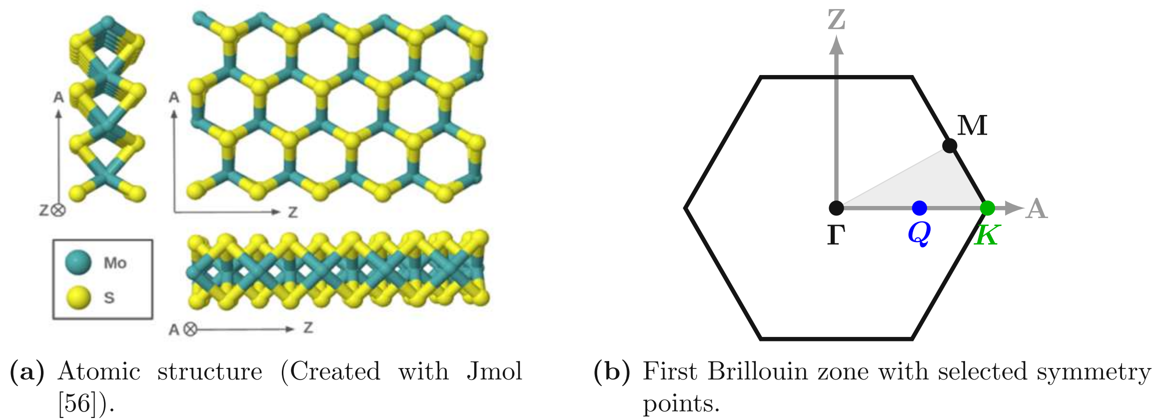

(a) Atomic structure (Created with Jmol [56]).

(b) First Brillouin zone with selected symmetry points.

Figure 5.12.: Characteristics of ML-MoS_2 in real- and **k**-space, including the armchair (A) and zigzag (Z) directions.

Due to advances in *ab-initio* calculations, especially using density functional theory (DFT), and gaps in experimental research on new materials, the band structure of ML-

Die approbierte gedruckte Originalversion dieser Diplomarbeit ist an der TU Wien Bibliothek verfügbar
The approved original version of this thesis is available in print at TU Wien Bibliothek.
TU Bibliothek WIEN Your knowledge hub

MoS_2 is mostly calculated with simulations from first principles [57]. This calculated band structure can then be approximated and used as a basis for the transport simulations of ML-MoS_2, as sketched in Fig. 5.13. However, problems may arise due to variations in the resulting band structure and the thereby varying resulting transport characteristics of the material, in case different approximations ('flavors') are applied for the *ab-initio* (DFT) calculations [57]. Within this thesis one characteristic of the band structure of ML-MoS_2, which highly depends on the selected 'flavor' of the *ab-initio* calculation, is selected and the effect of its variation on the resulting transport characteristics is evaluated. More precisely, this selected parameter is the energy difference ΔE_{QK} between the two conduction band minima at the **K**- and **Q**-points of the Brillouin zone, which is also sketched in Fig. 5.13. In the available literature, values between 60 meV and 300 meV can be found for this particular value [4].

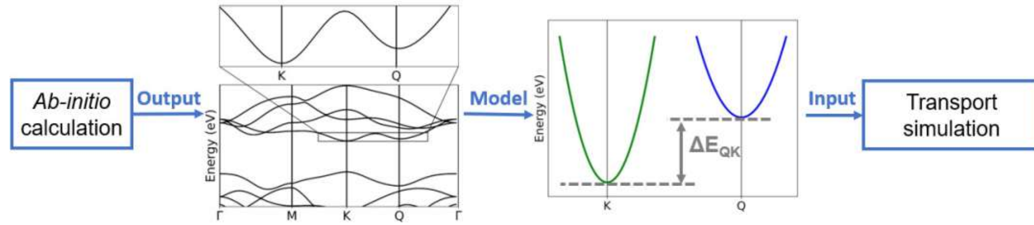

Figure 5.13.: Workflow for multi-valley Ensemble Monte Carlo simulation of electrons in ML-MoS_2.

While the value of ΔE_{QK} is varied within the values found in the literature, for the other parameters, which are required for the approximation of the band structure, fixed and established values, taken from Pilotto et al. [4], are applied. In general, only the minima around the $\boldsymbol{K}$- and $\boldsymbol{Q}$-points of the first Brillouin zone contribute to the electron transport and are approximated with the analytical band approach within this thesis. The constant-energy surfaces, positions, and orientations of the approximated valleys around these minima can be seen in Fig. 5.14. Moreover, the parameters used for the analytical band structure of ML-MoS_2 are shown in Table 5.2.

Valley	m_l $[m_0]$	m_t $[m_0]$	α $[eV^{-1}]$
$\boldsymbol{K}$	0.47	0.47	0.94
$\boldsymbol{Q}$	1.14	0.54	1.16

Table 5.2.: Parameters of approximated ML-MoS_2 valleys, taken from [4].

The scatter mechanisms, which are required for the simulation of ML-MoS_2, are inter- and intravalley scattering with acoustic and optical phonons. While acoustic intravalley scattering is calculated with the formula given in Eq. (2.20), the rates for the other mechanisms are given by Eq. (2.21). Furthermore, for the calculation of the scattering rates, half

Die approbierte gedruckte Originalversion dieser Diplomarbeit ist an der TU Wien Bibliothek verfügbar
The approved original version of this thesis is available in print at TU Wien Bibliothek.
TU WIEN Bibliothek Your knowledge hub

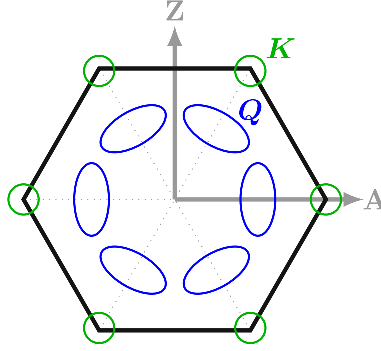

Figure 5.14.: $\boldsymbol{K}$- and $\boldsymbol{Q}$-valleys and their constant energy surfaces.

of the density of states for this two-dimensional material is required, which is given by [2]

$$N_{2D}(E) = \frac{m_d}{2\pi\hbar^2} \cdot (1 + 2\alpha E) \tag{5.3}$$

in case the non-parabolic approximation of the band structure described in Section 2.1.1 is applied. Finally, the parameters for the scattering mechanisms given in Li et al. [5], which are described in more detail in Section B.2, are used. The total scatter rates, which are the sums of the rates of all included mechanisms, for the $\boldsymbol{K}$- and $\boldsymbol{Q}$-valleys in ML-MoS_2 with varying values of ΔE_{QK}, can be seen in Fig. 5.15. Figure 5.15a shows that the total scatter rate in the $\boldsymbol{K}$-valleys decreases with increasing ΔE_{QK}. The reason for this decrease is that for intervalley scattering mechanisms between the $\boldsymbol{K}$- and $\boldsymbol{Q}$-valleys, the final energy E_f of particles after the scatter event, given in Eq. (2.22), depends on the valley energy separation. Due to the condition that E_f has to be non-zero, which is ensured by the Heaviside function in Eq. (2.21), the onset energy of scattering from $\boldsymbol{K}$- to $\boldsymbol{Q}$-valleys shifts to higher values for increasing ΔE_{QK}, thereby decreasing the resulting total scatter rates. For the total scatter rate of the $\boldsymbol{Q}$-valleys, shown in Fig. 5.15b, an increase in the scattering rates with increasing ΔE_{QK} can be observed. Again, the reason for this is the dependence of the final energy of the particles which scatter from the $\boldsymbol{Q}$- to the $\boldsymbol{K}$-valleys, which increases with increasing ΔE_{QK}.

5.2.1. Bulk Simulation

In this section, the effect of variations in ΔE_{QK} on the resulting bulk transport characteristics in ML-MoS_2 is analyzed with the application of the *Basic Bulk Particle Handler*. For this, multiple simulations of this 2D material are performed with varying ΔE_{QK} between 60 meV and 300 meV. In all simulations approximately 20 000 electrons are initialized within the $\boldsymbol{K}$-valleys. Additionally, their initial energy is determined using Eq. (3.1) and their wave-vector is initialized in a random direction within this 2D film, whereby the third dimension is discarded. Once all particles are initialized, their response to applied electric fields of varying strengths between 0 kV/cm and 400 kV/cm in the armchair (A) direction of the film, which is shown in Fig. 5.12, is tested.

Die approbierte gedruckte Originalversion dieser Diplomarbeit ist an der TU Wien Bibliothek verfügbar
The approved original version of this thesis is available in print at TU Wien Bibliothek.
TU WIEN Bibliothek Your knowledge hub

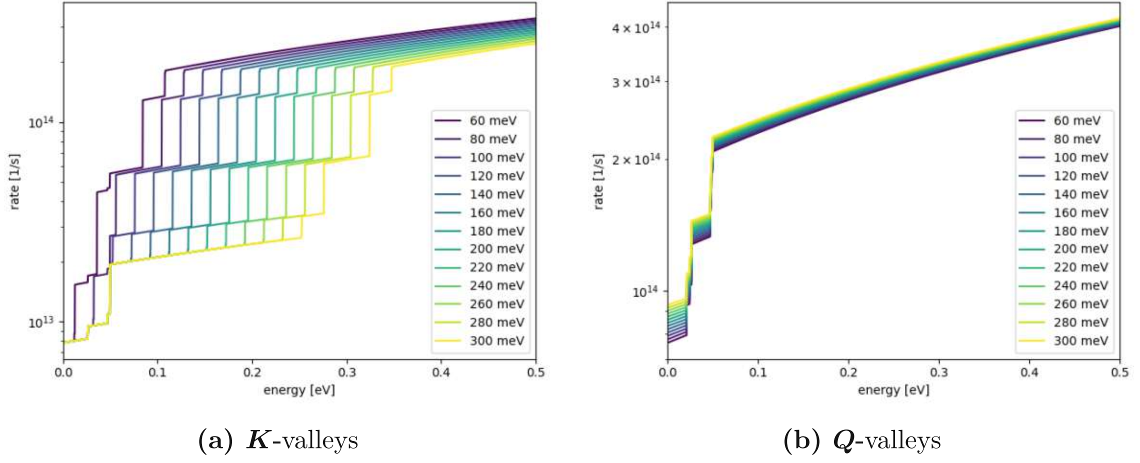

(a) $\boldsymbol{K}$-valleys

(b) $\boldsymbol{Q}$-valleys

Figure 5.15.: Total scatter rates in ML-MoS_2 with varying energy separation ΔE_{QK}.

First, the mean $\boldsymbol{K}$-valley population with different applied electric fields and varying ΔE_{QK} is shown in Fig. 5.16. It can be seen that for all values of ΔE_{QK} the $\boldsymbol{K}$-valley population decreases with increasing applied field strength. Due to the increasing field strength, more carriers are able to reach high enough energies to scatter into the higher energy $\boldsymbol{Q}$-valleys. Additionally, the results show that with increasing energy separation of the valleys, the population of the $\boldsymbol{K}$-valley also increases. This is expected as with growing ΔE_{QK} the energy onset of intervalley scattering from the $\boldsymbol{K}$- to the $\boldsymbol{Q}$-valleys increases, as shown in Fig. 5.15a. This effectively means that the electrons need to be accelerated more to be able to scatter into higher valleys. In addition to the findings of this work, Fig. 5.16 provides the results from Pilotto et al. [4], which assume a ΔE_{QK} of 160 meV and are in excellent agreement with our results.

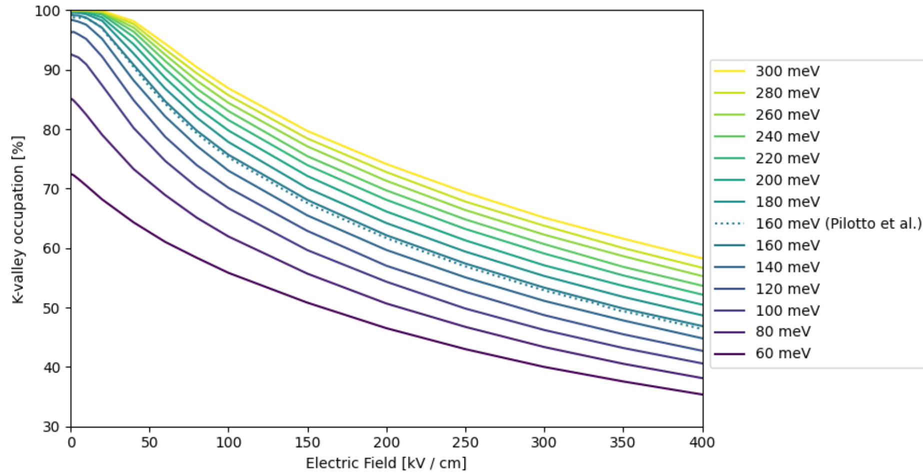

Figure 5.16.: $\boldsymbol{K}$-valley occupation of ML-MoS_2 vs. applied electric field for varying ΔE_{QK} and comparison to the findings of Pilotto et al. [4] (dotted line).

Die approbierte gedruckte Originalversion dieser Diplomarbeit ist an der TU Wien Bibliothek verfügbar
The approved original version of this thesis is available in print at TU Wien Bibliothek.
TU WIEN Bibliothek Your knowledge hub

Subsequently, the mobility due to varying ΔE_{QK} is provided in Fig. 5.17, where it can be observed that the resulting values vary between $100\,\mathrm{cm^2/(Vs)}$ and $300\,\mathrm{cm^2/(Vs)}$. At low valley separation energies, the mobility grows with increasing ΔE_{QK}. The reason for this increase is that with increasing valley separation energy, the onset energy for the scattering into the higher valleys also grows. Hence, a reduction of the importance and consequently of the limitation on the mobility of those scatter mechanisms at low fields is obtained. However, once ΔE_{QK} is sufficiently large, electrons at low-fields are not able to reach the onset energy for scattering into the $\boldsymbol{Q}$-valleys. This leads to a mobility which is independent of the investigated property ΔE_{QK} as the mobility is then only limited by the intra- and inter-valley scattering in the $\boldsymbol{K}$-valleys. This behavior can be observed in Fig. 5.17, for cases when ΔE_{QK} is larger than 160 meV.

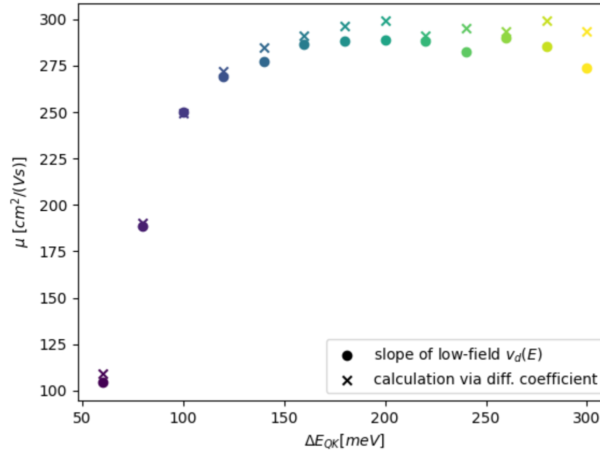

Figure 5.17.: Impact of varying ΔE_{QK} on the mobility of ML-MoS_2.

For stronger applied electric fields, Fig. 5.18 shows that the high-field drift-velocity slightly decreases with increasing ΔE_{QK}. Moreover, for higher values of the valley separation energy the Gunn Effect [58], including the typical negative differential mobility, can be observed. This effect occurs in multi-valley semiconductors with lower and higher energy valleys, where the later ones also have higher effective masses [59], as is the case for ML-MoS_2. This effect is not observable for simulations with lower values of ΔE_{QK} since, in those cases, a significant percentage of the electrons already populate the $\boldsymbol{Q}$-valleys at zero-field, as can be seen in Fig. 5.16. In addition to the findings of this work, Fig. 5.18 also includes the results of Pilotto et al. [4] and Li et al. [5], which assume ΔE_{QK} to be 70 meV and 160 meV, respectively, showing excellent agreement with our results.

Die approbierte gedruckte Originalversion dieser Diplomarbeit ist an der TU Wien Bibliothek verfügbar
The approved original version of this thesis is available in print at TU Wien Bibliothek.
TU WIEN Bibliothek Your knowledge hub

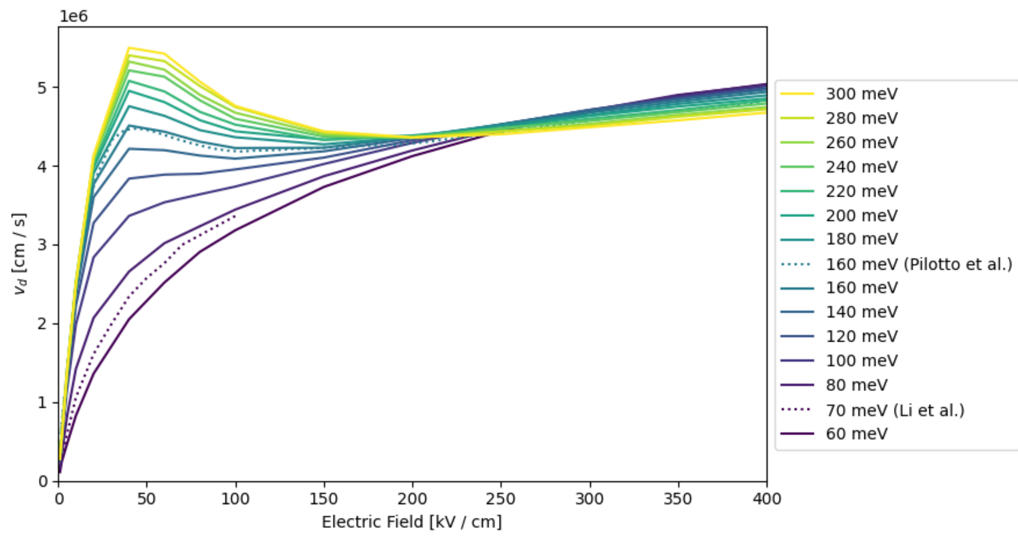

Figure 5.18.: Drift velocity vs. electric field with different ΔE_{QK} and comparison to findings of Pilotto et al. [4] and Li et al. [5] (dotted lines).

Die approbierte gedruckte Originalversion dieser Diplomarbeit ist an der TU Wien Bibliothek verfügbar
The approved original version of this thesis is available in print at TU Wien Bibliothek.
TU Bibliothek WIEN Your knowledge hub

6. Discussion

In the scope of this thesis an EMC simulation framework for various materials and devices was developed. The background and the general structure of this tool was explained and some sample applications of the developed library were presented.

The first presented application of this tool was the simulation of bulk silicon. For that, the response of electrons in silicon to electric fields of various strengths and directions at different temperatures was tested and compared to experimental results. It was shown that both the temperature-dependency and the anisotropy of the ensemble electron drift velocity within the material can be replicated with the developed simulation tool. For future applications, it should be noted that bulk simulations for various materials can be performed within this library. To apply the developed tool for the analysis of a new material, only the required material constants, the corresponding valleys, and the essential scattering mechanisms have to be introduced, which are typically obtained using DFT simulations.

Subsequently, real-space particle-particle interactions, calculated with the help of the FMM, as presented in Section 3.3.2, were included to the simulation of bulk silicon. Only initial tests which analyze the stability and reliability of this algorithm were performed, in which the cooling of an ensemble of electrons and ions at 3 000 K was observed by monitoring the evolution of the ensemble average of the electron energy. First, the resulting cooling behavior with and without the cut-off approach was compared. In case the cut-off approach was not used instead of the expected decrease of the ensemble energy with time, an increase in the ensemble energy for all tested discretized time steps Δt was observed. These observations suggest that using very long time steps may lead to instabilities and numerical heating. On the other hand, in case the cut-off approach was used, numerical instabilities and numerical heating were still observed, but a decrease in the discretized time step led to a decrease of these instabilities. This allowed for the evaluation of the upper limits of Δt which lead to the same resulting steady-state ensemble energy as the simulation which does not include the real-space particle-particle interactions. While, for the tests with bulks of silicon with a doping level of $1 \times 10^{13}\,\mathrm{cm}^{-3}$ and $1 \times 10^{15}\,\mathrm{cm}^{-3}$, the expected steady-state energy could be reached already with $\Delta t = 5\,\mathrm{fs}$, the limit for Δt decreases with increasing doping concentration. It was observed that for a doping concentration of $1 \times 10^{17}\,\mathrm{cm}^{-3}$ a time step below 1 fs and for a concentration of $1 \times 10^{18}\,\mathrm{cm}^{-3}$ a step below 0.05 fs is crucial to avoid this numerical artifact. The next steps for the inclusion of the real-space particle-particle interactions into the EMC workflow could be to perform further tests of this approach in bulk simulations with various applied electric fields in order to observe the effect of the inclusion of c-c and c-i interactions on the resulting ensemble drift velocity and energy and the extension of this approach towards device simulations. As already mentioned, to obtain the background force for device simulations, an adapted

Die approbierte gedruckte Originalversion dieser Diplomarbeit ist an der TU Wien Bibliothek verfügbar
The approved original version of this thesis is available in print at TU Wien Bibliothek.
TU WIEN Bibliothek Your knowledge hub

Poisson equation has to be solved, in which the effect of the particles needs to be discarded. For this extension, the tests within the scope of this thesis indicate that the choice of Δt within device simulations will likely be limited by the doping concentration in the highest doped region of the device.

After simulations with bulk silicon, simulations of a MOSFET device were performed, while the results were compared to the ones of the established tool `CEMC`, on which the developed library is based. Within this comparison, it was shown that the effect of different applied voltages at the drain and gate contact on the potential and drain current which is observed within `CEMC`, can be reproduced with the developed tool. Furthermore, while `CEMC` is written for the exclusive simulation of MOSFETs, the benefit of the newly developed tool is the generic definition of devices, whose idea is to enable the simulation of a broad range of materials and devices. Hence, the next steps for classical device simulations with the help of the developed tool could be simulations of other types of devices of interest, such as resistors or diodes, or the simulation of MOSFETs built from other materials.

Finally, the developed library was used to investigate monolayer molybdenum disulfide (ML-MoS_2). The band structure of this material is mostly obtained from *ab-initio* calculation. Problems often arise due to changes in the resulting band structure in case different approximations are used for the simulations from first principles and the thereby changing transport characteristics of this film. In the scope of this thesis the effect of changes in the energy difference ΔE_{QK} between $\boldsymbol{K}$- and $\boldsymbol{Q}$-valleys, which can vary between 60 meV and 300 meV when different *ab-initio* approximations are used, on the resulting carrier transport characteristics was analyzed. It has been shown that the theoretical electron mobility within the material varies between $100\,\mathrm{cm}^2/(\mathrm{Vs})$ and $300\,\mathrm{cm}^2/(\mathrm{Vs})$, when varying ΔE_{QK} within the values found in the literature while using established values for the other parameters. Additionally, it was shown that the relationship between the drift velocity and the electric field can vary highly, with the Gunn Effect only being observable for higher valley separation energies. The aim of this application was two-fold: First, it should show that the developed library can be applied to materials which differ from silicon and which are currently heavily investigated. Second, this study also shows that the impact of the $\boldsymbol{Q}$-valleys in ML-MoS_2 should be studied in more detail and, even though this material is investigated heavily, further investigations are necessary to obtain a physically realistic picture for the description of this material.

Die approbierte gedruckte Originalversion dieser Diplomarbeit ist an der TU Wien Bibliothek verfügbar
The approved original version of this thesis is available in print at TU Wien Bibliothek.
TU WIEN Bibliothek Your knowledge hub

Glossary

P^3M particle-particle particle-mesh. 26

2D two-dimensional. 3, 14, 24, 30, 31, 37, 38, 48, 50

3D three-dimensional. 3, 14, 30, 39

BTE Boltzmann transport equation. 5, 6, 13

c-c carrier-carrier. 25, 26, 28, 54

c-i carrier-impurity. 25, 26, 28, 54

CIC Cloud-In-Cell. 24

DFT density functional theory. 48, 49, 54

ECS ellipse coordinate system. 9, 10

EMC ensemble Monte Carlo. 3, 4, 10, 13–29, 36, 38, 43, 49, 54

FMM fast multipole method. 3, 26–29, 33, 36, 38, 42, 54

GaAs gallium arsenide. 7, 8, 38

ML-MoS_2 monolayer molybdenum disulfide. 48–52, 55, 66–68

MoS_2 molybdenum disulfide. 4, 38

MOSFET metal-oxide-semiconductor field-effect transistor. 3, 4, 31, 32, 44–46, 48, 55

NEC Nearest-Element-Center. 24, 44, 45

NGP Nearest-Grid-Point. 24

PM-Scheme Particle-Mesh Scheme. 23, 24, 29, 30, 36

SCS simulation coordinate system. 10

Si silicon. 38, 66

SOR Successive-Over-Relaxation. 23, 33, 65

Die approbierte gedruckte Originalversion dieser Diplomarbeit ist an der TU Wien Bibliothek verfügbar
The approved original version of this thesis is available in print at TU Wien Bibliothek.
TU Bibliothek WIEN Your knowledge hub

Bibliography

[1] R. W. Hockney and J. W. Eastwood, *Computer Simulation Using Particles*. Justus-Liebig-Universität Gießen: Taylor Francis, 1988. ISBN 978-0-852-74392-8

[2] D. Vasileska, S. M. Goodnick, and G. Klimeck, *Computational Electronics - Semi-classical and Quantum Device Modeling and Simulation*. CRC Press, 2017. ISBN 978-1-420-06484-1

[3] C. Canali, G. Ottaviani, and A. Alberigi Quaranta, "Drift velocity of electrons and holes and associated anisotropic effects in silicon," *Journal of Physics and Chemistry of Solids*, vol. 32, no. 8, pp. 1707–1720, 1971, doi: https://doi.org/10.1016/S0022-3697(71)80137-3.

[4] A. Pilotto, P. Khakbaz, P. Palestri, and D. Esseni, "Semi-classical transport in MoS_2 and MoS_2 transistors by a Monte Carlo approach," *Solid-State Electronics*, vol. 192, p. 108295, 2022, doi: https://doi.org/10.1016/j.sse.2022.108295.

[5] X. Li, J. T. Mullen, Z. Jin, K. M. Borysenko, M. Buongiorno Nardelli, and K. W. Kim, "Intrinsic electrical transport properties of monolayer silicene and MoS_2 from first principles," *Physical Review B*, vol. 87, p. 115418, March 2013, doi: https://doi.org/10.1103/PhysRevB.87.115418.

[6] M. Hosseini, M. Elahi, M. Pourfath, and D. Esseni, "Strain induced mobility modulation in single-layer MoS_2," *Journal of Physics D: Applied Physics*, vol. 48, no. 37, p. 375104, August 2015, doi: 10.1088/0022-3727/48/37/375104.

[7] C. K. Maiti, *Introducing Technology Computer-Aided Design (TCAD) - Fundamentals, Simulations, and Applications*. Jenny Stanford Publishing, 2017. ISBN 978-9-814-74552-9

[8] K. Tomizawa, *Numerical Simulation of Submicron Semiconductor Devices*. Artech House, 1993. ISBN 978-0-890-06620-1

[9] A. Gehring, "Simulation of Tunneling in Semiconductor Devices," Ph.D. dissertation, Technische Universität Wien, 2003, accessed: 2022-11-12. [Online]. Available: https://www.iue.tuwien.ac.at/phd/gehring/diss.html

[10] R. Entner, "Modeling and Simulation of Negative Bias Temperature Instability," Ph.D. dissertation, Technische Universität Wien, 2007, accessed: 2023-01-16. [Online]. Available: https://www.iue.tuwien.ac.at/phd/entner/diss.html

Die approbierte gedruckte Originalversion dieser Diplomarbeit ist an der TU Wien Bibliothek verfügbar
The approved original version of this thesis is available in print at TU Wien Bibliothek.
TU WIEN Bibliothek Your knowledge hub

[11] P. Ellinghaus, "Two-Dimensional Wigner Monte Carlo Simulation for Time-Resolved Quantum Transport with Scattering," Ph.D. dissertation, Technische Universität Wien, 2016, accessed: 2022-11-12. [Online]. Available: http://www.iue.tuwien.ac.at/phd/ellinghaus/

[12] C. M. Snowden, *Introduction to Semiconductor Device Modelling.* World Scientific, 1998. ISBN 978-9-810-23693-9

[13] H. Gummel, "A self-consistent iterative scheme for one-dimensional steady state transistor calculations," *IEEE Transactions on Electron Devices*, vol. 11, pp. 455–465, 1964, doi: https://doi.org/10.1109/T-ED.1964.15364.

[14] R. Klima, "Three-Dimensional Device Simulation with Minimos-NT," Ph.D. dissertation, Technische Universität Wien, 2002, accessed: 2023-01-08. [Online]. Available: https://www.iue.tuwien.ac.at/phd/klima/

[15] A. De Mari, "An accurate numerical steady-state one-dimensional solution of the P-N junction," *Solid State Electronics*, vol. 11, no. 1, pp. 33–58, 1968, doi: https://doi.org/10.1016/0038-1101(68)90137-8.

[16] D. L. Scharfetter and H. K. Gummel, "Large-signal analysis of a silicon Read diode oscillator," *IEEE Transactions on Electron Devices*, vol. 16, no. 1, pp. 64–77, 1969, doi: https://doi.org/10.1109/T-ED.1969.16566.

[17] J. E. Schroeder and R. S. Muller, "IGFET Analysis through numerical solution of Poisson's equation," *IEEE Transactions on Electron Devices*, vol. 15, no. 12, pp. 954–961, 1968, doi: https://doi.org/10.1109/T-ED.1968.16545.

[18] H. W. Loeb, R. Andrew, and W. Love, "Application of 2-dimensional solutions of the Shockley-Poisson equation to inversion-layer m.o.s.t. devices," *Electronics Letters*, vol. 4, pp. 352–354, 1968, doi: https://doi.org/10.1049/el:19680277.

[19] S. Selberherr, *Analysis and Simulation of Semiconductor Devices.* Springer Verlag, 1984. ISBN 978-0-387-81800-9

[20] E. Buturla, P. Cottrell, B. Grossman, K. Salsburg, M. Lawlor, and C. McMullen, "Three-dimensional finite element simulation of semiconductor devices," in *1980 IEEE International Solid-State Circuits Conference. Digest of Technical Papers*, vol. XXIII, 1980, doi: https://doi.org/10.1109/ISSCC.1980.1156066. pp. 76–77.

[21] S. Selberherr, A. Schutz, and H. W. Potzl, "MINIMOS - a Two-Dimensional MOS Transistor Analyzer," *IEEE Journal of Solid-State Circuits*, vol. 15, no. 4, pp. 605–615, 1980, doi: https://doi.org/10.1109/JSSC.1980.1051444.

[22] D. J. Roulston, "Three Dimensional Effects in Bipolar Transistors using Fast Combined 1D and 2D Numerical Simulation," in *Physics of Semiconductor Devices*, ser. Society of Photo-Optical Instrumentation Engineers (SPIE) Conference Series, V. Kumar and S. K. Agawal, Eds., vol. 3316, 1998, p. 967.

TU WIEN Bibliothek Your knowledge hub
Die approbierte gedruckte Originalversion dieser Diplomarbeit ist an der TU Wien Bibliothek verfügbar
The approved original version of this thesis is available in print at TU Wien Bibliothek.

[23] R. Minixhofer, "Integrating Technology Simulation into the Semiconductor Manufacturing Environment," Ph.D. dissertation, Technische Universität Wien, 2006, accessed: 2023-01-08. [Online]. Available: https://www.iue.tuwien.ac.at/phd/minixhofer/

[24] "Sentaurus Device: An advanced multidimensional (1D/2D/3D) device simulator," https://www.synopsys.com/silicon/tcad/device-simulation/sentaurus-device.html, accessed: 2022-30-09.

[25] "Victory Device Simulator," https://silvaco.com/tcad/victory-device-3d/, accessed: 2022-30-09.

[26] "GTS Minimos-NT," https://www.globaltcad.com/products/gts-minimos-nt/, accessed: 2022-10-10.

[27] "Sentaurus Device User Guide," https://picture.iczhiku.com/resource/eetop/WYktazdUiUOSQVMc.pdf, accessed: 2022-30-09.

[28] "Silvaco - Monte Carlo Device Applications," https://silvaco.com/examples/tcad/section19/index.html, accessed: 2022-12-29.

[29] "ViennaWD: A quantum decoherence simulator based on the Wigner formalism," https://viennawd.sourceforge.net/, accessed: 2022-01-10.

[30] P. Ellinghaus, J. Weinbub, M. Nedjalkov, S. Selberherr, and I. Dimov, "Distributed-Memory Parallelization of the Wigner Monte Carlo Method Using Spatial Domain Decomposition," *Journal of Computational Electronics*, vol. 14, no. 1, p. 151–162, 2015, doi: https://doi.org/10.1007/s10825-014-0635-3.

[31] J. Weinbub, P. Ellinghaus, and M. Nedjalkov, "Domain Decomposition Strategies for the Two-Dimensional Wigner Monte Carlo Method," *Journal of Computational Electronics*, vol. 14, no. 4, 2015, doi: https://doi.org/10.1007/s10825-015-0730-0.

[32] "scalFMM : N-body simulation using kernel independent fast multipole method," https://gitlab.inria.fr/solverstack/ScalFMM, accessed: 2022-03-08.

[33] P. Blanchard, B. Bramas, O. Coulaud, E. Darve, L. Dupuy, A. Etcheverry, and G. Sylvand, "ScalFMM: A Generic Parallel Fast Multipole Library," 2015.

[34] D. K. Ferry, *Semiconductor Transport*. Taylor & Francis, 2000. ISBN 978-0-748-40866-5

[35] M. Lundstrom, *Fundamentals of Carrier Transport*. Cambridge University Press, 2009. ISBN 978-0-521-63724-4

[36] D. Esseni, P. Palestri, and L. Selmi, *Nanoscale MOS Transistors - Semi-Classical Transport and Applications*. Cambridge University Press, 2011. ISBN 978-1-139-49438-0

TU WIEN Bibliothek Your knowledge hub
Die approbierte gedruckte Originalversion dieser Diplomarbeit ist an der TU Wien Bibliothek verfügbar
The approved original version of this thesis is available in print at TU Wien Bibliothek.

[37] C. Moglestue, *Monte Carlo Simulation of Semiconductor Devices*. Springer Science Business Media, 2013. ISBN 978-9-048-14008-4

[38] C. Jacoboni and P. Lugli, *The Monte Carlo Method for Semiconductor Device Simulation*. Springer Science Business Media, 2012. ISBN 978-3-709-16963-6

[39] R. Hathwar, "Generalized monte carlo tool for investigating low-field and high-field properties of materials using non-parabolic band structure model," Master Thesis, Arizona State University, 2011.

[40] R. Haberlandt, S. Fritzsche, and H.-L. Vörtler, "Chapter 10 - Simulation of microporous systems: Confined fluids in equilibrium and diffusion in zeolites," in *Handbook of Surfaces and Interfaces of Materials*. Academic Press, 2001, pp. 357–443. ISBN 978-0-12-513910-6

[41] R. Kircher and W. Bergner, *Three-Dimensional Simulation of Semiconductor Devices*. Springer-Verlag, 2013. ISBN 978-3-034-87731-2

[42] A. Schenk, *Advanced Physical Models for Silicon Device Simulation*. Springer Science Business Media, 1998. ISBN 978-3-211-83052-9

[43] C. Wordelman and U. Ravaioli, "Integration of a particle-particle-particle-mesh algorithm with the ensemble Monte Carlo method for the simulation of ultra-small semiconductor devices," *IEEE Transactions on Electron Devices*, vol. 47, no. 2, pp. 410–416, 2000, doi: https://doi.org/10.1109/16.822288.

[44] W. Gross, D. Vasileska, and D. Ferry, "A novel approach for introducing the electron-electron and electron-impurity interactions in particle-based simulations," *IEEE Electron Device Letters*, vol. 20, no. 9, pp. 463–465, 1999, doi: https://doi.org/10.1109/55.784453.

[45] S. Tyaginov, M. Bina, J. Franco, Y. Wimmer, B. Kaczer, and T. Grasser, "On the importance of electron–electron scattering for hot-carrier degradation," *Japanese Journal of Applied Physics*, vol. 54, p. 04DC18, 2015, doi: https://doi.org/10.7567/JJAP.54.04DC18.

[46] W. J. Gross, D. Vasileska, and D. Ferry, "3D Simulations of Ultra-small MOSFETs with Real-space Treatment of the Electron–Electron and Electron-ion Interactions," *VLSI Design*, vol. 10, 2000, doi: https://doi.org/10.1155/2000/48474.

[47] D. Vasileska, W. J. Gross, and D. K. Ferry, "Monte Carlo particle-based simulations of deep-submicron n-MOSFETs with real-space treatment of electron-impurity interactions," *Superlattices and Microstructures*, vol. 27, no. 2, pp. 147–157, 2000, doi: https://doi.org/10.1006/spmi.1999.0806.

[48] C. Heitzinger, C. Ringhofer, S. Ahmed, and D. Vasileska, "Efficient simulation of the full Coulomb interaction in three dimensions," 2004, doi: https://doi.org/10.1109/IWCE.2004.1407300. pp. 24 – 25.

Die approbierte gedruckte Originalversion dieser Diplomarbeit ist an der TU Wien Bibliothek verfügbar
The approved original version of this thesis is available in print at TU Wien Bibliothek.
TU WIEN Bibliothek Your knowledge hub

[49] H. Khan, D. Vasileska, S. Ahmed, C. Ringhofer, and C. Heitzinger, "Modeling of FinFET: 3D MC Simulation Using FMM and Unintentional Doping Effects on Device Operation," *Journal of Computational Electronics*, vol. 3, pp. 337–340, 2004, doi: https://doi.org/10.1007/s10825-004-7072-7.

[50] C. Heitzinger, C. Ringhofer, S. Ahmed, and D. Vasileska, "Accurate Three-Dimensional Simulation of Electron Mobility Including Electron-Electron and Electron-Dopant Interactions," 2005.

[51] R. K. Beatson and L. Greengard, "A short course on fast multipole methods," 1997.

[52] P. Blanchard, "Fast hierarchical algorithms for the low-rank approximation of matrices, with applications to materials physics, geostatistics and data analysis," Ph.D. dissertation, Université de Bordeaux, 2017.

[53] "ViennaEMC: Repository of the library developed within this thesis," https://github.com/ViennaTools/ViennaEMC/tree/500aa1b48b45635924be59c95b62d1f7caa6ea43, accessed: 2023-02-02.

[54] W. S. Yun, S. W. Han, S. C. Hong, I. G. Kim, and J. D. Lee, "Thickness and strain effects on electronic structures of transition metal dichalcogenides: 2H-MX_2 semiconductors (M = Mo, W; X = S, Se, Te)," *Physical Review B*, vol. 85, p. 033305, 2012, doi: https://doi.org/10.1103/PhysRevB.85.033305.

[55] U. Krishnan, M. Kaur, K. Singh, M. Kumar, and A. Kumar, "A synoptic review of MoS_2: Synthesis to applications," *Superlattices and Microstructures*, vol. 128, pp. 274–297, 2019, doi: https://doi.org/10.1016/j.spmi.2019.02.005.

[56] "Jmol: an open-source java viewer for chemical structures in 3D," http://www.jmol.org/, accessed: 2022-07-25.

[57] G. Gaddemane, S. Gopalan, M. L. Van de Put, and M. V. Fischetti, "Limitations of ab initio methods to predict the electronic-transport properties of two-dimensional semiconductors: The computational example of 2H-phase transition metal dichalcogenides," *Journal of Computational Electronics*, vol. 20, no. 1, p. 49–59, 2021, doi: https://doi.org/10.1007/s10825-020-01526-1.

[58] J. Gunn, "Microwave oscillations of current in III–V semiconductors," *Solid State Communications*, vol. 1, no. 4, pp. 88–91, 1963, doi: https://doi.org/10.1016/0038-1098(63)90041-3.

[59] P. N. Butcher, "The Gunn effect," *Reports on Progress in Physics*, vol. 30, no. 1, p. 97, 1967, doi: https://doi.org/10.1088/0034-4885/30/1/303.

TU Bibliothek WIEN Your knowledge hub
Die approbierte gedruckte Originalversion dieser Diplomarbeit ist an der TU Wien Bibliothek verfügbar
The approved original version of this thesis is available in print at TU Wien Bibliothek.

Die approbierte gedruckte Originalversion dieser Diplomarbeit ist an der TU Wien Bibliothek verfügbar
The approved original version of this thesis is available in print at TU Wien Bibliothek.
TU WIEN Bibliothek Your knowledge hub

Appendices

A. Solution of the Poisson Equation

This section presents the solution of the Poisson equation which is utilized within the scope of this thesis.

A.1. Domain Partitioning

As mentioned in Section 3.2.1, the partitioning of the simulation space is performed with a uniform mesh which uses spacing $\boldsymbol{h} = (h_x, h_y, h_z)$ between the grid points. In this mesh, a grid point is identified with its coordinates $\boldsymbol{c} = (i, j, k)$. Additionally, due to this partition all characteristics of the device are known only on the discrete grid points and not in the continuous space.

A.2. Discrete Approximation

The continuous Poisson equation is given in Eq. (1.2) and repeated, with the additional assumption of a constant dielectric constant ϵ, in the following:

$$\Delta\Phi = \frac{\partial^2\Phi}{\partial x^2} + \frac{\partial^2\Phi}{\partial y^2} + \frac{\partial^2\Phi}{\partial z^2} = \frac{q \cdot (n - p + N_A - N_D)}{\epsilon} \quad . \tag{A.1}$$

As already mentioned for Eq. (1.2), n represents the electron concentration, p the hole concentration, and N_D and N_A are the concentrations of positively- and negatively-charged impurities in the simulated device, respectively [9]. Due to the knowledge of all characteristics of the device only at the discrete grid points, the Laplace operator, required for the Poisson equation, must be approximated. For this reason, the second order central difference can be applied for the approximation of each second order derivative. In the following, this approximation is shown for the derivative in the x-direction at coordinate (i, j, k) [38]

$$\frac{\partial^2\Phi_{ijk}}{\partial x^2} \approx \frac{\Phi_{i+1jk} + \Phi_{i-1jk} - 2\Phi_{ijk}}{h_x^2} \quad , \tag{A.2}$$

where h_x is the spacing of the mesh in the corresponding direction. Applying Eq. (A.2) for all second order derivatives, then leads to

$$\begin{aligned}\Delta\Phi_{ijk} :=& \frac{\Phi_{i+1jk} + \Phi_{i-1jk} - 2\Phi_{ijk}}{h_x^2} + \frac{\Phi_{ij+1k} + \Phi_{ij-1k} - 2\Phi_{ijk}}{h_y^2} + \\ & \frac{\Phi_{ijk+1} + \Phi_{ijk-1} - 2\Phi_{ijk}}{h_z^2} \quad .\end{aligned} \tag{A.3}$$

Die approbierte gedruckte Originalversion dieser Diplomarbeit ist an der TU Wien Bibliothek verfügbar
The approved original version of this thesis is available in print at TU Wien Bibliothek.
TU WIEN Bibliothek Your knowledge hub

The resulting discrete approximation of the Poisson equation at coordinate $\boldsymbol{c} = (i, j, k)$ is then given by

$$\Delta\Phi_{ijk} \approx \frac{q(n_{ijk} - p_{ijk} + N^A_{ijk} - N^D_{ijk})}{\epsilon_{ijk}} \quad , \tag{A.4}$$

where each characteristic only has to be evaluated at the discrete points of the given uniform mesh.

A.2.1. Normalization

To avoid numerical under- and overflow and to increase the efficiency of the algorithm, the variables in the Poisson equation are scaled [2]. For the potential, the thermal voltage $V_T = \frac{k_b T}{q}$, for length the intrinsic Debye length $L_D = \sqrt{\frac{\epsilon V_T}{q n_i}}$, and for the carrier concentration the intrinsic carrier concentration n_i are used as scaling factors [2]. In the following all normalized characteristics will be marked with a tilde, which then leads to the following normalized and approximated equation

$$\begin{aligned}\Delta\tilde{\Phi}_{ijk} := \frac{\tilde{\Phi}_{i+1jk} + \tilde{\Phi}_{i-1jk} - 2\tilde{\Phi}_{ijk}}{\tilde{h}_x^2} + \frac{\tilde{\Phi}_{ij+1k} + \tilde{\Phi}_{ij-1k} - 2\tilde{\Phi}_{ijk}}{\tilde{h}_y^2} + \frac{\tilde{\Phi}_{ijk+1} + \tilde{\Phi}_{ijk-1} - 2\tilde{\Phi}_{ijk}}{\tilde{h}_z^2} \\ \approx \tilde{n}_{ijk} - \tilde{p}_{ijk} + \tilde{N}^A_{ijk} - \tilde{N}^D_{ijk} \quad .\end{aligned} \tag{A.5}$$

A.3. Solution of the Discrete Approximation

In this thesis an iterative solver is used to solve the approximation of the Poisson equation. The idea of this approach is to start with an initial guess for the potential $\tilde{\Phi}^0$ and update this solution step by step with a given update equation until a specific tolerance is met [38].

A.3.1. Linearization

Due to the dependence of the electron and hole concentrations, n and p, respectively, on the potential, the Poisson equation is not linear. To make this equation linear, it is assumed that for small changes δ in the potential the concentrations can be approximated with [2]

$$n(\Phi + \delta) \approx n(\Phi)\left(1 + \frac{\delta}{V_T}\right) \quad \text{and} \tag{A.6}$$

$$p(\Phi + \delta) \approx p(\Phi)\left(1 - \frac{\delta}{V_T}\right) \quad , \tag{A.7}$$

where V_T is the thermal voltage. This approximation is based on the equilibrium behavior of the concentrations, shown in Eqs. (3.19) and (3.20).

Die approbierte gedruckte Originalversion dieser Diplomarbeit ist an der TU Wien Bibliothek verfügbar
The approved original version of this thesis is available in print at TU Wien Bibliothek.
TU WIEN Bibliothek Your knowledge hub

A.3.2. Update of the Potential

The basis of the update equation which enables the calculation of the potential of the next step, for which $\tilde{\Phi}^{t+1}_{ijk} = \tilde{\Phi}^{t}_{ijk} + \tilde{\delta}_{ijk}$ is assumed, can be derived from the combination of Eqs. (A.5) to (A.7), given by

$$\Delta\tilde{\Phi}^{*}_{ijk} \approx \tilde{N}^{A}_{ijk} - \tilde{N}^{D}_{ijk} + \tilde{n}_{ijk}(1 + (\tilde{\Phi}^{t+1}_{ijk} - \tilde{\Phi}^{t}{}_{ijk})) - \tilde{p}_{ijk}(1 - (\tilde{\Phi}^{t+1}_{ijk} - \tilde{\Phi}^{t}_{ijk})) \quad . \tag{A.8}$$

The final update formula for the calculation of $\tilde{\Phi}^{t+1}_{ijk}$ can then be obtained by rearranging all occurring terms. Additionally, in this formula $\Delta\tilde{\Phi}^{*}_{ijk}$ represents the discrete approximation of the Laplace operator which requires the evaluation of the potential on the neighboring discrete mesh points for its calculation. The approach for the evaluation of the potential on the neighboring points depends on the applied method [38]: First, for the *Jacobi* method, the neighboring values are all taken from the last fully completed step t. Second, for the *Gauss-Seidl* method, each updated value is used immediately. This means that, in case a neighbor of the current point has already been updated in step $t+1$, the newest value of the potential at that point is already used for the update of the current point. Finally, the Successive-Over-Relaxation (SOR) method uses the resulting potential $\tilde{\Phi}^{GS}_{ijk}$ from one step of the Gauss-Seidl method for the calculation of the potential of the next step using

$$\tilde{\Phi}^{t+1}_{ijk} = \omega\tilde{\Phi}^{GS}_{ijk} + (1-\omega)\tilde{\Phi}^{t}_{ijk} \quad , \tag{A.9}$$

where ω is a selected value between 1 and 2 [2]. Within the scope of this thesis, the SOR method is applied.

Die approbierte gedruckte Originalversion dieser Diplomarbeit ist an der TU Wien Bibliothek verfügbar
The approved original version of this thesis is available in print at TU Wien Bibliothek.
TU WIEN Bibliothek Your knowledge hub

B. Simulation Parameters

This section presents the parameters which were used for the simulation of silicon and ML-MoS_2.

B.1. Silicon (Si)

The applied simulation parameter for silicon include its dielectric constant $\epsilon = 11.8\,\epsilon_0$, its density $\rho = 2329\,\mathrm{kg/m^3}$, and its velocity of sound $v_s = 9040\,\mathrm{m/s}$. Additionally, the parameters for the approximation of the used valley, with the six equivalent subvalleys, is given in Table 5.1.

Acoustic intravalley scattering, optical zero-th and first order intervalley scattering are the included scatter mechanisms for this material. For acoustic intravalley scattering a deformation potential of $\Xi = 9\,\mathrm{eV}$ is used. For intervalley scattering two types, f- and g-type, are distinguished, as described in Section 5.1. Moreover, all subvalleys have the same energy at the minimum, meaning that $\Delta E_{fi} = 0$ and the number of final valleys to scatter into Z_f for g-type scattering is 1 and for f-type is 4. The supplementary applied values for silicon intervalley optical scattering are shown in Table B.1 and are taken from Vasileska et al. [2].

Parameter	Value
D_f^0	$5.23 \times 10^{10}\,\mathrm{eV/m}$
D_g^0	$5.23 \times 10^{10}\,\mathrm{eV/m}$
$\hbar\omega_f^0$	$60\,\mathrm{meV}$
$\hbar\omega_g^0$	$60\,\mathrm{meV}$
D_f^1	$2.5\,\mathrm{eV}$
D_g^1	$4\,\mathrm{eV}$
$\hbar\omega_f^1$	$23\,\mathrm{meV}$
$\hbar\omega_g^1$	$18\,\mathrm{meV}$

Table B.1.: Parameters for intervalley optical scattering in silicon, taken from Vasileska et al. [2].

TU Bibliothek WIEN Your knowledge hub
Die approbierte gedruckte Originalversion dieser Diplomarbeit ist an der TU Wien Bibliothek verfügbar
The approved original version of this thesis is available in print at TU Wien Bibliothek.

B.2. Monolayer Molybdenum Disulfide (ML-MoS_2)

In this section the material parameters applied for the simulation of ML-MoS_2 are provided. First, a density $\rho = 3.1 \times 10^{-7}$ g/cm^2 and a sound velocity of $v_s = 6.6 \times 10^3$ m/s are applied [5]. Additionally, the parameters for the valleys are presented in Table 5.2 and are established values taken from Pilotto et al. [4].

Acoustic intravalley scattering and optical and acoustic intervalley scattering are included in the simulations. While a sketch of the possible intervalley scattering events out of a ***K***- and ***Q***-valley and the involved phonon are sketched in Fig. B.1, the parameters used for the calculation of the corresponding scatter rates can be found in Table B.3. Additionally, the energies of the phonons, which are involved in the scattering, are shown in Table B.2.

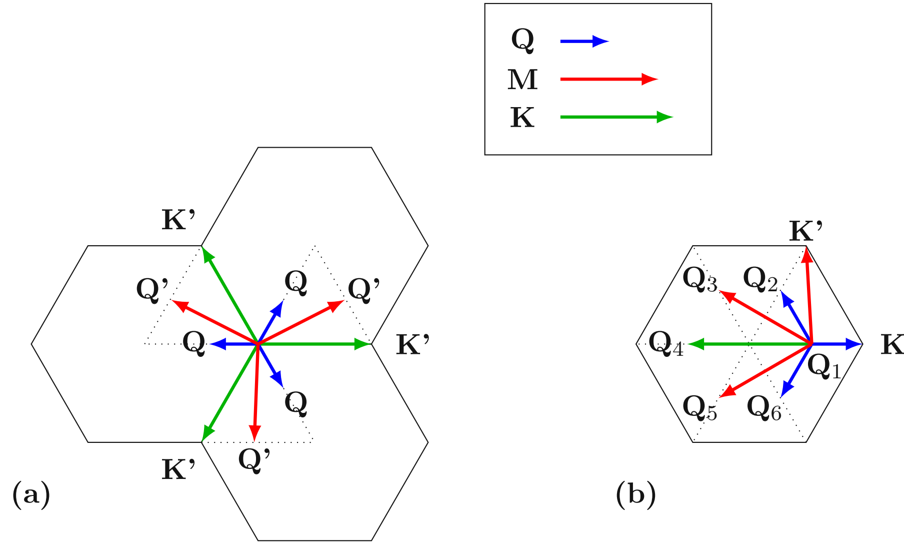

Figure B.1.: Intervalley scatter mechanisms out of (a) ***K***- and (b) ***Q***-valleys and sketch of the corresponding phonon momenta (color).

Phonon mode	Γ	K	M	Q
acoustic [meV]	0	26.1	24.2	20.7
optical [meV]	49.5	46.8	47.5	48.1

Table B.2.: Phonon energies at symmetry points in ML-MoS_2, taken from [5, 6].

Die approbierte gedruckte Originalversion dieser Diplomarbeit ist an der TU Wien Bibliothek verfügbar
The approved original version of this thesis is available in print at TU Wien Bibliothek.
TU WIEN Bibliothek Your knowledge hub

Phonon momentum	**Electron transition**	**Deformation Potential**
Γ	$\boldsymbol{K} \rightarrow \boldsymbol{K}$	$\Xi = 4.5\,\mathrm{eV}$
		$D^{op} = 5.8 \times 10^8\,\mathrm{eV/cm}$
K	$\boldsymbol{K} \rightarrow \boldsymbol{K'}$	$D^{ac} = 1.4 \times 10^8\,\mathrm{eV/cm}$
		$D^{op} = 2.0 \times 10^8\,\mathrm{eV/cm}$
Q	$\boldsymbol{K} \rightarrow \boldsymbol{Q}$	$D^{ac} = 9.3 \times 10^7\,\mathrm{eV/cm}$
		$D^{op} = 1.9 \times 10^8\,\mathrm{eV/cm}$
M	$\boldsymbol{K} \rightarrow \boldsymbol{Q'}$	$D^{ac} = 4.4 \times 10^8\,\mathrm{eV/cm}$
		$D^{op} = 5.6 \times 10^8\,\mathrm{eV/cm}$
Γ	$\boldsymbol{Q_1} \rightarrow \boldsymbol{Q_1}$	$\Xi = 2.8\,\mathrm{eV}$
		$D^{op} = 7.1 \times 10^8\,\mathrm{eV/cm}$
Q	$\boldsymbol{Q_1} \rightarrow \boldsymbol{Q_2}$ or $\boldsymbol{Q_6}$	$D^{ac} = 2.1 \times 10^8\,\mathrm{eV/cm}$
		$D^{op} = 4.8 \times 10^8\,\mathrm{eV/cm}$
M	$\boldsymbol{Q_1} \rightarrow \boldsymbol{Q_3}$ or $\boldsymbol{Q_5}$	$D^{ac} = 2.0 \times 10^8\,\mathrm{eV/cm}$
		$D^{op} = 4.0 \times 10^8\,\mathrm{eV/cm}$
K	$\boldsymbol{Q_1} \rightarrow \boldsymbol{Q_4}$	$D^{ac} = 4.8 \times 10^8\,\mathrm{eV/cm}$
		$D^{op} = 6.5 \times 10^8\,\mathrm{eV/cm}$
Q	$\boldsymbol{Q_1} \rightarrow \boldsymbol{K}$	$D^{ac} = 1.5 \times 10^8\,\mathrm{eV/cm}$
		$D^{op} = 2.4 \times 10^8\,\mathrm{eV/cm}$
M	$\boldsymbol{Q_1} \rightarrow \boldsymbol{K'}$	$D^{ac} = 4.4 \times 10^8\,\mathrm{eV/cm}$
		$D^{op} = 6.6 \times 10^8\,\mathrm{eV/cm}$

Table B.3.: Parameters used for scatter mechanisms of ML-MoS_2, taken from [5, 6]. Additionally, intervalley scattering is visualized in Fig. B.1 and the phonon momenta are given in Table B.2.

Die approbierte gedruckte Originalversion dieser Diplomarbeit ist an der TU Wien Bibliothek verfügbar
The approved original version of this thesis is available in print at TU Wien Bibliothek.
TU WIEN Bibliothek Your knowledge hub